ABSTRACT

Title of dissertation: PATH PLANNING, FLOW ESTIMATION,
AND DYNAMIC CONTROL
FOR UNDERWATER VEHICLES

Francis D. Lagor Jr., Doctor of Philosophy, 2017

Dissertation directed by: Professor Derek A. Paley
Department of Aerospace Engineering
Institute for Systems Research

Underwater vehicles such as robotic fish and long-endurance ocean-sampling platforms operate in challenging fluid environments. This dissertation incorporates models of the fluid environment in the vehicles' guidance, navigation, and control strategies while addressing uncertainties associated with estimates of the environment's state. Coherent flow structures may be on the same spatial scale as the vehicle or substantially larger than the vehicle. This dissertation argues that estimation and control tasks across widely varying spatial scales, from vehicle-scale to long-range, may be addressed using common tools of empirical observability analysis, nonlinear/non-Gaussian estimation, and output-feedback control.

As an application in vehicle-scale flow estimation and control, this dissertation details the design, fabrication, and testing of a robotic fish with an artificial lateral-line inspired by the lateral-line flow-sensing organ present in fish. The robotic fish is capable of estimating the flow speed and relative angle of the oncoming flow. Using symmetric and asymmetric sensor configurations, the robot achieves the primitive fish behavior called rheotaxis, which describes a fish's tendency to orient upstream.

For long-range flow estimation and control, path planning may be accomplished using observability-based path planning, which evaluates a finite set of candidate control inputs using a measure related to flow-field observability and selects an optimizer over the set. To incorporate prior information, this dissertation derives an augmented observability Gramian using an optimal estimation strategy known as Incremental 4D-Var. Examination of the minimum eigenvalue of an empirical version of this Gramian yields a novel measure for path planning, called the empirical augmented unobservability index. Numerical experiments show that this measure correctly selects the most informative paths given the prior information.

As an application in long-range flow estimation and control, this dissertation considers estimation of an idealized pair of ocean eddies by an adaptive Lagrangian sensor (i.e., a platform that uses its position data as measurements of the fluid transport, after accounting for its own control action). The adaptive sampling is accomplished using the empirical augmented unobservability index, which is extended to non-Gaussian posterior densities using an approximate expected-cost calculation. Output feedback recursively improves estimates of the vehicle position and flow-field states.

PATH PLANNING, FLOW ESTIMATION, AND DYNAMIC CONTROL FOR UNDERWATER VEHICLES

by

Francis D. Lagor Jr.

Dissertation submitted to the Faculty of the Graduate School of the
University of Maryland, College Park in partial fulfillment
of the requirements for the degree of
Doctor of Philosophy
2017

Advisory Committee:
Professor Derek A. Paley, Chair/Advisor
Professor Kayo Ide, Dean's Representative
Professor Anya R. Jones
Professor P. S. Krishnaprasad
Professor Robert M. Sanner

Acknowledgments

I offer my sincere thanks to my advisor and mentor, Prof. Derek Paley. His commitment to his students, their scholarship, and their long-term success is unparalleled. I was very fortunate to have him as an advisor. I did my very best to resist his approaches and methods, only to realize in the end their overwhelming value. I thank Derek for his persistent support, constructive criticism, and most of all, his patience. There are many attributes that make him an excellent mentor, including his ingenuity, his scholarship, and professional writing acumen. However, his most important attributes in my development were his patience and persistence. For these, I am very much indebted.

I am thankful for so many wonderful professors at the University of Maryland (UMD) whose efforts inside and outside of the classroom made my time at Maryland truly memorable. Foremost, I thank Prof. P. S. Krishnaprasad for his mentorship, instruction, and kindness. I am also grateful for the education I received from Profs. Anya Jones, Rob Sanner, and James Carton (Department of Atmospheric and Oceanic Science). Their engaging courses have built a strong foundation in me. I am grateful to my dissertation committee, in particular, Prof. Kayo Ide (Department of Atmospheric and Oceanic

Science) for thought-provoking conversations as well as careful critiques and suggestions. The last Maryland professor to whom I am largely indebted is Prof. Norm Wereley. I thank him for not firing me after I tipped over his X-ray machine—I also thank the X-ray machine for not landing on me!

Close collaborations, funded and non-funded, as well as internal and external to UMD, enriched the research process for me, strengthening the questions I asked and my methods for answering them. I gratefully acknowledge Prof. Sean Humbert (University of Colorado Boulder) and his former student Badri Narayanan Ranganathan, Prof. Xiaobo Tan (Michigan State University) and his former student, Hong Lei, as well as Prof. Sheryl Coombs (Bowling Green State University). I am grateful to Prof. James Tangorra (Drexel University) and his former student, Jeff Kahn, for lending pressure sensors used in Chapter 4. I thank Prof. Alison Flatau for lending a flow probe used in Chapter 4. Profs. Levi DeVries (U. S. Naval Academy) and Feitian Zhang (George Mason University) provided tremendous collaborations in robotic fish research following the work detailed in Chapter 4. I acknowledge helpful discussions with Prof. Pierre Lermusiaux (Massachusetts Institute of Technology) and his former student, Tapovan Lolla, regarding the Gaussian Mixture Kalman Filter in Chapters 3 and 7.

I will forever cherish time spent with my friends, the current and former members of the Collective Dynamics and Control Laboratory (CDCL), including Sachit Butail, Tracie Severson, Chin Gian Hooi, Nitin Sydney, Amanda Chicoli, Derrick Yeo, Will Scott, Helene Nguewou, Jinseong Lee, Debdipta Goswami, Brian Free, Will Craig, and Brett Barkley. I am especially grateful for the dear friendship of my perennial officemate, Daigo Shishika—

his continued encouragement and companionship have meant a great deal to me. I had the privilege of working with many excellent undergraduates who provided indispensible research assistance through the CDCL and Research Experience for Undergraduate (REU) programs, including Mukund Patnaik, Patrick Washington, Kathryn Waychoff, Storm Weiner, Amy Davis, and Cody Karcher.

I appreciate the friendship and camaraderie of other current and former graduate students at Maryland, including Dave Mayo, Elena Shrestha, Tom Pillsbury, Steve Day, Steve Sherman, Andrew Becnel, Lina Castano, Mac MacFarlane, Andrew Kehlenbeck, Kedar Dimble, Hector Escobar, Greg Gremillion, Andrew Lind, Field Manar, Gino Perrotta, Peter Mancini, Vera Klimchenko, Vikram Hrishikeshavan, Udit Halder, Joe Schmaus, Elizabeth Ward, Robbie Vocke, Nishan Jain, Dipankar Maity, Yunlong Huang, Biswadip Dey, Jeff Gillette, Alejandro Rivera, Peter Rossoni, Ben Barry, Chris Binz, and Will Staruk. They made coming to work enjoyable each and every day. I appreciate the tireless efforts of the administrative staff in the Department of Aerospace Engineering, including Otto Fandino, Aaron Broome, Tom Hurst, Becky Sarni, Laura Thorsen, and LaVita Williams, for doing all of the important behind-the-scenes work needed to support my research.

My family has provided unwavering support for me throughout the long road of graduate school. My Mom and Dad and my siblings, Bill, Kristen, Erin, and Stephen are so much a part of who I am. I thank each of them for always being there for me, letting me talk through my highs and lows, and for sharing in my successes and failures. I thank my parents-in-law, Bob and Roberta. They have always treated me like a son of their own, with love, kindness, and respect. I thank my beautiful daughter, Claire. She is such a gift, and she reminds me everyday about the big beautiful world that exists outside of work. Most of all, I thank my best friend, the love of my life, my wonderful wife, Annie. I thank her for always believing in me, for always trusting me, and for always supporting me. Her tremendous love fills me each and every day.

I gratefully acknowledge funding from the Office of Naval Research, Bioinspired Autonomous Systems program, under grant N00014-12-1-0149, as well as support from the National Science Foundation's, Dynamics, Control and System Diagnostics program under award CMMI-1362837. Undergraduates contributing to preliminary versions of the work in Chapter 7 received support from the National Science Foundation TREND REU under award PHY-1461089. I acknowledge the UMD supercomputing resources (http://www.it.umd.edu/hpcc) made available for the simulations in Chapter 7.

Table of Contents

List of Tables

List of Figures

List of Nomenclature

	Symbol modifiers
$\tilde{(\cdot)}$	Quantity corrupted by noise
$\hat{(\cdot)}$	Estimated quantity
$\check{(\cdot)}$	Particular or marked quantity
$\bar{(\cdot)}$	Complex conjugate
$\underline{(\cdot)}$	Mean value in GMM model
$(\cdot)'$	Differentiation with respect to arc length
$(\cdot)^{-1}$	Matrix inverse
$(\cdot)^a$	Analysis quantity (i.e., after assimilation of data)
$(\cdot)^d$	Desired or target quantity
$(\cdot)^f$	Forecast quantity (i.e., prior to assimilation of data)
$(\cdot)^T$	Transpose
$(\cdot)_j$	Subscript indexing of vector representing jth entry
$(\cdot)_k$	Time index subscript
$(\cdot)_R$	Quantity specified in co-rotating frame
	Lowercase Greek letters
α	Self-propulsive speed (Chapter 2); Angle of attack (Chapter 4)
β	Angle of total velocity vector relative to positive x-axis in inertial frame
γ_0, γ_B, γ_E, γ_I, γ_λ	Target curve in steering control law, Bézier curve, an exterior Bertrand curve, an interior Bertrand curve, a parameterized family of curves
$\delta x(t), \delta y(t)$	Perturbation state vector at time t, Perturbation output vector at time t
ϵ	Vector of perturbation values
η	Angle from (a_1, a_2) frame to (b_1, b_2) frame (Chapter 2); Additive white measurement noise vector (Chapter 4); Perturbation direction in Fréchet differentiation (Chapter 6)

θ	Polar angle in ξ plane (Chapter 4)
$\theta(t)$	Inertial orientation at time t (Chapter 2)
κ_s	Signed curvature
κ_a, κ_b	Coefficients in Zhang and Leonard's control law
λ	Cylinder offset for conformal mapping (Chapter 4); Displacement from γ_0 curve (Chapter 5)
$\lambda_{\min}$	Minimum eigenvalue
$\mu(t)$	White, Gaussian measurement noise at time t
$\nu, \nu_a, \nu_{a,j}$	Unobservability index, Empirical augmented unobservability index, ν_a for jth route
ξ	Complex coordinate for conformal mapping (Chapter 4)
$\xi(t)$	Complex coordinate in co-rotating reference frame at time t (Chapter 2)
π	Ratio of a circle's circumference to its diameter
$\pi(\cdot)$, $\pi(\cdot\vert\cdot)$	Probability density function, Conditional probability density function (Chapter 6)
ρ	Fluid density (Chapter 4); Total self-propulsion speed (Chapter 2)
σ	Measurement noise standard deviation vector (Chapter 3); Dummy variable for continuous parameterization (Chapter 5)
τ_{relax}	Time constant for relaxation of complexity penalty in BIC optimization
$\phi(t, t_0, x(t_0))$	State solution from $(t_0, x(t_0))$ evaluated at time t (Chapter 6);
ϕ	Initial phase angle of vortex pair's rotation (Section 2.3.1)
χ	Curve orientation
ψ	Stream function
ω	Angular rotation rate of vortex pair
	Uppercase Greek letters
Γ_j	Circulation strength for vortex j
Δp	Pressure difference measurement vector
$\Theta(z)$	Generic scalar function over $\mathbb{C}$
$\Pi(z)$	Scalar-valued function over $\mathbb{C}$ meeting technical requirements
$\Phi(t_1, t_2)$	State transition matrix from time t_1 to time t_2 (Chapters 3,6)
$\Phi(z)$	Scalar orbit function (Chapter 5)
Ψ	Mean vector for transition density
Ψ_e	Empirical output sensitivity matrix in calculation of $\mathcal{W}_{\text{eo}}$, $\mathcal{W}_{\text{ea}}$
Ω	Vector of flow-model parameters (Chapter 4); Region of steering law validity (Chapter 5)
	Lowercase English letters
a_1, a_2	Path frame unit vectors

b_1, b_2	Unit vectors for secondary frame based on gradient of scalar field
b	Real constant in conformal mapping (Chapter 4)
c_0, c_1, c_2, c_3	Control points in Bézier curve
d	Vortex separation distance
e	Euler's number $2.71828\dots$
$\mathbf{e}_j$	Unit vector with 1 in the jth position
$f(z), f_j$	Complex representation of flow velocity, Flow contribution from jth vortex
$g(t, x(t))$	Nonlinear dynamics function evaluated at $x(t)$ at time t (Chapters 3,6)
g	Acceleration due to gravity (Chapter 4)
$h(t, x(t))$	Nonlinear observation function evaluated at $x(t)$ at time t
i	imaginary unit
j, k	Subscript indices
m	Dimension of measurement vector
n	Dimension of state vector
p, p_s	Static pressure, stagnation pressure
r_1, r_2	Radii of concentric circles in cusp smoothing
s	Arc length
t, t_0, Δt	Time, Initial time, Change in time
$u(t), u_{[t_0,t]}, u^j$	Control signal at time t, Open-loop control signal specified on $[t_0, t]$ time interval, jth candidate control input (Chapters 5,6,7)
$u(t)$	Steering control input at time t for self-propelled particle in flow (Chapter 2)
$u_{\max}$	Saturation value for control input u
u_x, u_y	Real and imaginary components of complex-valued function (e.g., flow velocity)
$v(t)$	White Gaussian noise vector at time t (Chapters 3,6); Steering control input at time t for self-propelled particle without flow (Section 2.4)
$w(\xi)$	Complex potential function (Chapters 2,4)
$w(t)$	Process noise vector at time t (Chapter 3)
w_m	Scalar GMM weight for Gaussian m (Chapter 3)
$x(t)$	State vector at time t
$y(t)$	Measurement vector at time t
$x_r(t), y_r(t)$	State reference trajectory vector at time t, Output reference trajectory vector at time t
$x^{\text{true}}(t)$	True state vector at time t
$\underline{x}_m(t)$	Mean state vector for Gaussian m in GMM at time t
$z(t), z_j(t)$	Complex number/Location in complex plane at time t, Location of jth vortex at time t
z_c	Point on curve γ_0 closest to z

z_{cv}	Center of vorticity

Uppercase English letters

$A(t)$	Linear dynamics matrix at time t
$C(t)$	Linear observation matrix at time t(Chapters 3,6)
C	Total pressure (Chapter 4)
C_p	Coefficient of pressure
D, D_k	Collection of measurements, Collection of measurements at time index k
$G(t)$	Process noise input matrix at time t
H	Linear observation/output matrix
$J(\delta x)$	Cost function for update to state estimate δx
$J_0(\delta x_0)$	Cost function over reduced δx_0 space
K	Number of free parameters in BIC fit (Chapter 3)
$K,\ K_1,\ K_2,\ K_3,\ K_4$	Control gains
M	Number of Gaussians in GMM
N	Number of parameters in flow model
N_e	Number of ensemble members in GMKF
$P(t), P_0, P_m$	State covariance matrix at time t, Initial state covariance matrix, Covariance associated with mth Gaussian in GMM
$Q(t)$	Process noise covariance matrix at time t
R	Cylinder radius (Chapter 4)
$R(t)$	Measurement noise covariance matrix at time t (Chapters 3,6,7)
S	Saddle point location in $\mathbb{C}$
T	Period of orbit
T_h	Time horizon in path planning
T_{plan}	Time horizon for re-evaluating plan
T_{vort}	Period of vortex rotation
T_{sim}	Simulation duration
T_{samp}	Time duration between measurements
U	Flow speed
V	Generic square matrix
W	Generic square matrix

Calligraphic, blackboard, decorative letters

$\mathbb{C}$	The field of complex numbers
$\mathbb{I}$	Identity matrix
$\Im(\cdot)$	Imaginary component operator
$\mathcal{N}(\mu, R)$	Gaussian probability density function with mean μ and covariance R
$\mathbf{0}$	Matrix of zeros
$\mathbb{R}, \mathbb{R}^+$	The real numbers, The positive real numbers

$\Re(\cdot)$	Real component operator
$\mathcal{W}_{\mathrm{o}}$	Observability Gramian
$\mathcal{W}_{\mathrm{ao}}$	Augmented observability Gramian
$\mathcal{W}_{\mathrm{so}}$	Stochastic observability Gramian
$\mathcal{W}_{\mathrm{ea}}$	Empirical augmented observability Gramian
$\mathcal{W}_{\mathrm{eo}}$	Empirical observability Gramian

List of Abbreviations

4D-Var	Four Dimensional and Variational (data assimilation method)
A-OP	Augmented-Observability Planner
BIC	Bayesian Information Criterion
EnKF	Ensemble Kalman Filter
EM	Expectation-Maximization
IPMC	Ionic Polymer Metal Composite
GMKF	Gaussian Mixture Kalman Filter
GMM	Gaussian Mixture Model
GMM-DO	Gaussian Mixture Model-Dynamically Orthogonal Field Equations data assimilation method
`MaxComplexity`	Maximum number of Gaussians permitted in BIC optimization
`MaxIter`	Maximum number of EM iterations permitted in Gaussian mixture fitting
pdf	Probability density function

Chapter 1

Introduction

The past few decades have seen the emergence of mobile autonomous systems as practical and useful technologies. These technologies have moved beyond proof-of-concept demonstrations driven by the research community. Society at-large is now demanding these technologies to improve daily life and our understanding of the world around us. Autonomous Underwater Vehicles (AUVs) are of particular interest. These vehicles may automate patrol of harbors, bays, littoral zones, in-land lakes, and some rivers, as well as inspect infrastructure. Autonomous ocean vehicles can now take scientific measurements within a long-duration deployable network. These submersible technologies have the potential to secure our domestic waterways and to contribute meaningfully to our understanding of the threat of global climate change.

AUVs have great potential, but underwater autonomy has been a major research focus for several decades. Despite many proof-of-concept demonstrations with AUVs, most applications still have not progressed beyond teleoperation of robotic platforms [1] or pre-planned missions with limited forms of autonomy based on simple switching in response of pre-programmed events [2]. One may attribute delayed progress to the many challenges faced by these platforms.

Some of the largest challenges currently faced by submersible autonomous robots involve their interactions with their surrounding fluid environments. Understanding the surrounding environment can be challenging because of the breadth of dynamic behavior exhibited by fluid flows—the system is infinite-dimensional, distributed, time-varying, and can display multi-scale effects, leading to turbulence and chaos. For some applications, understanding the surrounding fluid environment can be relatively straightforward. For example, many large, fast-moving vehicles such as commercial aircraft and naval submarines address flow interactions by linearization of the vehicle dynamics about fixed operating conditions (e.g., steady, wings-level flight) and scheduling control gains to stitch together these operating points [3]. This approach does not require knowledge of the fluid environment beyond the conditions experienced at each operating point, for which extensive empirical testing is performed. Of interest are applications in which the surrounding flow field is not simply addressed through linearization and coherent flow structures are dynamically relevant to the vehicle and its intended path. For smaller vehicles with reduced power available for control, vehicle stabilization in an unknown flow becomes increasingly important. Additionally, long-endurance vehicles need to consider large, coherent flow structures that may greatly influence their intended path if they wish to minimize control effort or ensure their intended trajectory is feasible given control limitations.

This dissertation contributes to the control design practices for AUVs by developing flow-aware controllers that enable interaction with the surrounding fluid environment. It contributes estimation and control loops that have understanding of the surrounding flow as a primary design objective. By employing output-feedback control, nonlinear/non-Gaussian estimation, and observability-based sensor placement and routing, the vehicle recursive improves its understanding of the flow by updating its flow map using information collected from sensors. Using the updated flow map, the vehicle then can take control action to further another control objective within the flow field or navigate to highly informative regions of the flow field to collect additional measurements. This control design methodology applies in two example applications: (i) the orientation control of a bioinspired robotic fish, and (ii) adaptive sampling of an autonomous vehicle deployed to monitor a pair of ocean eddies. Improved control of robotic fish will enhance our national security, while intelligent path planning for ocean-sampling vehicles will lead to new scientific understanding of the world's oceans and climates.

1.1 Statement of the problem

One challenging consideration for mobile autonomous robotic systems is the influence of an unknown or unsteady flow field [4–6]. Robotic platforms operating in *challenging flows* face difficult vehicle-fluid interaction problems. Challenging fluid flows may be *strong flows*, in which local flow speeds may meet or exceed vehicle's through-water speed (i.e., the speed of the vehicle relative to the flow) thereby inhibiting forward progress [7]. Complex fluid flows also include flow fields with prominent nonlinearities, including coherent flow structures on the order of the vehicle's body length or larger, that are dynamically relevant to the stability and long-range trajectory of the vehicle. For many applications, the presence of a challenging flow means that traditional control techniques based on linearization are insufficient.

The challenges of the vehicle's Guidance, Navigation, and Control (GNC) in challenging flows are substantially enhanced if the flow is *unknown* or *uncertain*. The term *unknown* is reserved for flows in which very little is known about the surrounding environment—only that the physics of fluid dynamics apply. In the case of an unknown flow, there is insufficient prior information from initial conditions, boundary conditions, or other constraints to be able to form a reduced-order model of the flow. Reduced-order models are often necessary for rapid evaluation within a control loop. Addressing GNC of robotic platforms in fully unknown flows is beyond the scope of this dissertation and is a direction for future research (see Section 8.2). This dissertation focuses on *uncertain* flows. The term *uncertain* is reserved to indicate that the true flow state is not known, but there is sufficient prior information of the flow structure to be able to form a reduced-order model. Further, the vehicle may make estimates of the true flow state, but these estimates carry a degree of uncertainty with them. The challenge then lies in properly quantifying all of the uncertainties about the flow and utilizing this knowledge effectively in the vehicle's GNC.

Complex vehicle-fluid interaction problems occur across many spatiotemporal scales. This dissertation considers two general categories: vehicle-scale interactions and long-range interactions. Vehicle-scale interactions occur at the same spatial scale of the vehicle body and occur over a timescale consistent with how long it takes the vehicle to traverse a body length (or a small multiple of the body length) when traveling at an average vehicle speed. Long-range interactions occur over distances that greatly exceed the vehicle length scale and on a timescale that is consistent with the much longer length scale, when traveling at an average vehicle speed. The two categories of vehicle-scale and long-range fluid interactions correspond naturally and respectively with the two control objectives of stabilization and path planning. Vehicle stabilization typically is achieved by a controller running in a fast inner loop that controls the vehicle dynamics in the presence of disturbances. Path planning is usually a task assigned to a slower outer loop that takes deliberative control action to achieve a higher-level control objective.

AUVs should be capable of understanding their local, surrounding flow using flow sensors. AUVs should also be capable of inferring the global flow structure in the far field through exploration and coordination with other vehicles. With these capabilities, AUVs will be able to achieve effective GNC in challenging flows by building stabilizing and path planning controllers with understanding of the flow environment at both vehicle and long-range scales.

Engineers must overcome substantial challenges in order to meet these goals. Some of the most prominent challenges concern the fundamental limitations of observability that may inhibit unique inference of the state of the fluid system. Observability is the property by which the initial state of a system can be uniquely inferred by watching the output or measurements of the system over a specified time horizon. Being able to infer the initial state of an infinite-dimensional, nonlinear dynamical system uniquely using a finite number of sensors is undoubtedly doomed to failure without additional knowledge or constraints to aid in the inference. However, by carefully arranging the sensors on the body of the vehicle as well as moving the sensors within the flow field while integrating the measurements in time, it is possible to restore observability.

The next question concerns how to move the sensors to maximize observability. One approach is observability-based path planning, in which candidate control inputs are evaluated by simulating their impact on observability over a future time interval. The criterion for evaluation is a measure called the empirical unobservability index. Until now, it has been unclear how to incorporate prior information about the state of the vehicle and the flow within observability-based path planning. Additionally, there exists no comprehensive adaptive-sampling framework based on observability that makes proper use of state uncertainty in estimation, feedback, and path planning.

To study vehicle-scale flow sensing, this dissertation considers the application of closed-loop stabilizing control of a bioinspired robotic fish using flow-sensing information. To study the long-range flow sensing, this dissertation tackles the application of ocean sampling using a guided sensor that takes its own position data as measurements. Together, the following tasks directly address the challenges of GNC for AUVs in challenging flows and form the basis of this dissertation:

1. *Develop a control framework for closed-loop motion control of a bioinspired robotic fish, using only local, flow-sensing information.*

2. *Determine the how to incorporate prior information from ongoing flow-field estimation in observability-based evaluation of possible future paths.*

3. *Develop an adaptive-sampling framework for flow-field estimation by a guided sensor*

using its Lagrangian data as measurements.

1.2 Survey of related work

This section provides surveys of related literature in the areas of bioinspired flow sensing and control, observability-based path planning, and flow estimation using ocean sampling vehicles. Due to the wide breadth of topics covered in this dissertation, these surveys only focus on the most pertinent works known to the author at the time of writing. Additional references appear elsewhere in the text of the dissertation where appropriate.

1.2.1 Bioinspired flow sensing and control

A flow field provides rich information to the evolutionarily adaptive, flow-sensing features present in some biological systems [8, 9]. The field of bioinspired flow sensing has developed with the following objectives: (i) to use biological structures to inform the design, fabrication, and packaging of artificial flow-sensing devices for autonomous robotics [5, 10]; and (ii) to develop algorithms for data assimilation and control that use these complex flow-sensing arrays to achieve specific functional goals, such as local flow-field estimation, object identification, and navigation [6, 11, 12].

One prominent example of an advanced biological flow-sensing system is the lateral-line system present in all cartilaginous and bony fish and aquatic amphibians [9, 12]. The uses of the lateral-line system in fish behavior include orienting in flow (rheotaxis), schooling, detecting obstacles, and avoiding predators. For example, the blind Mexican cave fish (Astyanax fasciatus) relies exclusively on the lateral-line system for orienting, navigating, and schooling [8, 9]. The lateral-line system runs the length of the fish and is made up of receptors, known as neuromasts, ranging in number from under 100 to over 1000 [9]. The neuromasts consist of ciliary bundles of hair cells, covered in a gelatinous outer dome called a cupula, that serve as mechano-electrical transducers with directional sensitivity [8]. Neuromasts exist in two types: superficial neuromasts, which are located on the exterior surface; and canal neuromasts, which are located between pore entrances of a subdermal lateral-line canal. Superficial neuromasts serve as flow-velocity sensors, whereas canal neuromasts respond to pressure-driven flow in the canal in order to measure pressure differences [13].

Two specific fish behaviors of interest for bioinspired robotics are rheotaxis and station-holding, because they serve as foundational behaviors from which one can construct a more complex repertoire. Rheotaxis is a behavior in which a fish orients upstream toward oncoming flow [14]; station-holding is a behavior in which a fish maintains position behind an upstream obstacle [8]. The lateral-line sensing modalities are thought to play an important role in executing these behaviors [8]. An artificial lateral-line system for use on an autonomous underwater vehicle would enhance its autonomy by providing a short-range sensing modality. Moreover, it would provide indispensable sensory information in dark, murky, or cluttered environments, where traditional sensing modalities like vision or sonar may be impaired.

Since the first artificial lateral-line was fabricated [15], researchers have developed artificial lateral-line systems using a variety of sensor types, including microfabricated hot-wire anemometry [15], capacitive [16], piezoresistive [17], optical [12], and ionic polymer metal composite cantilever [11] sensors. Yang *et al.* [10] designed an artificial lateral-line canal and demonstrated the properties of band-pass filtering and noise rejection in dipolar and turbulent flows. Tao and Yu [9] provided a comprehensive review of biomimetic hair flow sensors, and Ren and Mosheni [18] performed analytical work for flow sensing of a Kármán vortex street. Abdulsadda and Tan [11] created an artificial lateral-line using ionic polymer metal composite cantilever sensors and trained an artificial neural network to localize a dipole source. Venturelli *et al.* [13] showed that an artificial lateral-line made of off-the-shelf piezoresistive pressure sensors (approximating pressure-difference measurements of canal neuromasts) can be used to identify the presence of a Kármán vortex street and its hydrodynamic features. Kottapalli *et al.* [19, 20] developed liquid crystal polymer pressure sensors in a flexible array for mounting on curved surfaces. Asadnia *et al.* [21] produced a piezoelectric artificial lateral-line requiring zero power input.

Although many investigators have constructed artificial lateral-line systems, few have implemented closed-loop estimation and control using sensor data, and these controllers have been empirical in nature. For example, Salumäe *et al.* [6] demonstrated closed-loop rheotaxis of a robotic fish using pressure sensors and a Braitenberg controller, which is a memoryless controller that uses direct pressure readings from sensors on opposing sides of the fish to turn in the direction of increasing signal strength. Using empirical techniques, Salumäe and Kruusmaa [22] also demonstrated closed-loop station-holding control of a fish robot. Work is still needed to develop model-based controllers that will be extensible to more challenging flow environments.

Chapter 4 presents an output-feedback-control framework for achieving rheotaxis using symmetric and asymmetric artificial lateral-line sensor arrays. This research presented novel contributions at the time of publication. Since publication, additional significant robotic fish research has been performed. DeVries *et al.* [23] created an artificial lateral line with multiple sensing modalites, using Ionic Polymer Metal Composite (IPMC) whisker sensors to mimic the sensory information from superficial neuromasts and signal differences from pressure sensors to mimic the sensory information from canal neuromasts. Using this multimodal, artificial lateral line, the pressure-difference measurement equation from Chapter 4, and many of the same components in output-feedback-control framework, DeVries *et al.* [23] demonstrated rheotaxis with improved flow-field estimation and station holding behind an upstream obstacle (also known as flow refuging [24]). Zhang *et al.* [25] also utilized the pressure-difference measurement equation from Chapter 4 in a flow-sensing and control framework for station keeping of a self-propelled, flexible robotic fish. The station keeping task involved identification of the oncoming freestream flow speed and self-propulsion with a corresponding forward average velocity to avoid being swept back by the current. Modification of the output-feedback-control loop required inclusion of a feedforward term capturing the inverse kinematics needed to swim at an average forward speed.

Other notable contributions in bioinspired flow sensing and control since the publication of the findings in Chapter 4 include the works of Xu and Mohseni [26] and Akanyeti *et al.* [24]. Xu and Mohseni [26] derive a method for the automatic use of pressure signals on the hull of an AUV for estimating the hydrodynamic forcing on the body. They use the estimated forcing in a control framework for trajectory tracking with the control design being accomplished with robust-integral-of-the-sign-of-the-error (RISE) control and backstepping. They show the benefit of their framework in simulation and conduct a one degree-of-freedom gantry-controlled test of the trajectory tracking of a cylinder outfitted with pressure sensors. Akanyeti *et al.* [24] construct a three degree-of-freedom robotic fish constrained to the plane and endowed with an artificial lateral line made up of commercial off-the-shelf pressure sensors. The authors use empirically constructed relations to extract information of the robot's flow-relative states as well as salient flow features. Using these correlations, the authors perform a number of closed-loop control experiments, including station keeping, station holding behind an obstacle, and flow-aided trajectory following.

1.2.2 Observability-based path planning

Observability is the property of being able to infer the initial state of a system or underlying model parameters by observing the system output over a fixed time interval. In Chapters 6 and 7, the system under study is a fluid dynamic environment surrounding and influencing a mobile sensor, and the vehicle must infer the parameters in a flow model that most accurately represent the environment. In such a context, observability-based path planning refers to the systematic selection of paths that enhance the vehicle's observability of the underlying flow-field parameters.

Many researchers have planned informative routes by considering a path's observability or empirical observability, which is an approximation to observability for nonlinear systems. Hinson *et al.* [27] analytically derive a trajectory that maximizes the observability of inertial position and heading for a self-propelled vehicle in uniform flow. They pose an optimal-control problem to choose a path that minimizes the condition number of the observability Gramian for the linearized dynamics. Unfortunately, analytical solutions to the optimal-control problem exist only in specialized cases due to non-differentiability and non-convexity of the cost functional [27]. This problem may be addressed with grid-based optimization [7], or evaluation over a family of pre-determined candidate trajectories. Quenzer and Morgansen [28] also perform a finite-dimensional optimization over a discrete set of constant turning rates for an empirical observability-based controller in a multivehicle helming application.

Another method for performing finite-dimensional optimization of observability is to consider evaluation over a family of pre-determined candidate trajectories. The Adaptive Sampling and Prediction field experiment of 2006 in Monterey Bay performed a similar optimization over a family of coordinated sampling patterns with respect to a sampling performance metric [29]. In addition to reducing computational cost, this method permits integration of observability optimization with other control policies that may have generated the candidate trajectories. For example, Chapter 7 generates candidate trajectories by steering a vehicle to separating boundaries of invariant regions in a two-vortex flow field.

A topic not previously addressed in the observability-based path planning literature is the incorporation of prior information with a forward-looking observability analysis. This topic is the focus of Chapter 6, and the result is a novel concept called augmented observability. However, incorporating prior information in general adaptive sampling has been accomplished in previous works by maximizing the anticipated reduction in error covariance. For example, Bishop *et al.* [30] consider an adaptive network design problem by optimizing the forecasted error covariance of an Ensemble Transform Kalman Filter over a finite set of possible network realizations. Davis *et al.* [31] also consider the forecasted covariance reduction in an objective analysis estimation technique to simulate routes for underwater gliders. Reducing the anticipated error covariance is a closely related topic to incorporating prior information in observability-based path planning, and Section 6.5 specifically addresses the similarities and differences.

Augmented observability in Chapter 6 includes an observability Gramian and an inverse covariance. Due to inclusion of an inverse covariance matrix, one may consider it to be an information-theoretic concept. Existing research [32] has shown the utility of information metrics for nonuniform spatiotemporal coverage when sampling via a team of cooperative oceanographic vehicles. Other researchers [33] use mutual information for multivehicle scalar-field sampling. To make the connection between augmented observability and information theory explicit, Section 6.4 relates the empirical augmented observability Gramian to the Fisher information matrix for initial-condition inference.

1.2.3 Flow estimation using ocean-sampling vehicles

Distributed environmental sampling is an active field of research [34, 35] due to its many applications, including contaminant plume localization [36], biological monitoring [37], and data assimilation in atmospheric and oceanic sciences [38, 39]. Autonomous sampling vehicles determine advantageous routes for measurement collection in response to uncertainty in estimates of a real-time environmental process [40]. Significant hardware and sensor improvements [41] as well as algorithmic performance guarantees [42, 43] have further encouraged interest. However, there are open challenges about how mobile sensor platforms can most effectively sample and interact with challenging flow environments [7, 43, 44]. When the underlying flow field is uncertain these difficulties are further magnified.

Ocean sampling for the purpose of ocean-state estimation is of particular interest. Due to strong ocean-atmosphere coupling, improved understanding of the ocean may lead to better predictions in atmospheric climate variations on a wide range of time scales [45, 46]. Ocean-observing systems provide essential information on the state of the ocean for use in oceanographic, atmospheric, and climatological modeling and forecasting. One such system is Argo, a continuously deployed, global array of drifting platforms that capture temperature, current, and salinity data on vertical dives [47]. Although the Argo system already provides subsurface measurements, these measurements are incredibly sparse—only 3,750 floats in 361,900,000 square kilometers of ocean [46, 48].

Observation sparsity motivates the need for sampling with long-endurance autonomous vehicles like underwater drifters (passive vehicles that operate at constant depth) and ocean gliders (steered vehicles that operate at variable depths) [35, 49, 50] in the design of the next global, ocean-observing system. A steered sampling platform such as a glider that travels within the flow field taking targeted observations may be even more beneficial than passive drifter, even if the drifter has longer endurance. Utilizing such platforms and their Lagrangian position data (i.e., time-series measurements of vehicle position), autonomous control algorithms may exploit flow-field forecasts by using underlying currents for transport and uncertainty reduction. The benefits of underwater gliders for adaptive sampling have been established for reducing uncertainties in estimates of ocean processes [35, 49, 50], and for sampling and tracking oceanographic features [34, 37]. However, there exists no comprehensive framework that takes advantage of ocean-current forecasts for autonomous and coordinated path planning of multiple, minimally actuated vehicles.

Prior works have examined energy [51] and time-optimality [43] of path planning for point-to-point navigation of a self-propelled vehicle using stochastic-optimization and level-set methods. However, a framework for extended-deployment ocean sampling, which is focused primarily on flow-field estimation, should address transport barriers formed by coherent structures for understanding the flow-field geometry. Coherent structures are also important for long-endurance path planning [51], coverage and sampling [52], and understanding ocean transport processes in general [50]. Mallory *et al.* [44] highlighted the importance of coherent structures in the flow field for understanding spatial transport and sampling coverage. Prior works have also addressed this issue by optimizing the launch site of passively drifting vehicles (e.g., see [53]).

Coherent structures in strong flows such as ocean eddies and gyres create (almost) invariant sets or entrained regions; a vehicle cannot leave the set without exerting control. There are many techniques for identifying coherent structures in flows [54]. For example, Lagrangian Coherent Structures (LCS) are calculated by finding the local maxima in a Finite Time Lyapunov Exponent (FTLE) field [55]. Another approach uses the stochastic Frobenius-Perron operator to examine the transition probabilities between spatially discretized cells [54]. Methods also exist for quantifying the uncertainty of such structures [56].

To test the adaptive-sampling framework, Chapter 7 considers flow-field estimation around a pair of coherent ocean eddies modeled as point vortices. Coherent eddies in the ocean persist on mesoscales (10 to 500 km) and submesoscales (1 to 10 km) for weeks or even months. These coherent structures play an important role in global transport and mixing processes [57]. During field experiments of the second Autonomous Ocean Sampling Network (AOSN-II), small-scale (15 km) eddies appeared at the mouth of Monterey Bay and contributed to the overall transport of cold water away from the southern part of the bay [37]. Understanding transport within these flow structures is possible but requires *in situ* observations over a large spatiotemporal volume collected by fleets of autonomous vehicles [7, 57–59]. Section 2.3.1 describes the two-vortex system in which invariant sets and coherent flow structures appear. Chapter 7 utilizes the invariant-set boundaries in the planning algorithm and samples along invariant-set boundaries to improve the overall flow-field observability. Empirical observability analysis of a drifting Lagrangian sensor motivates this proposal. Krener and Ide [60] previously applied empirical observability to Lagrangian and Eulerian sensor deployment in a point-vortex flow. Section 5.1 extends their analysis to show that the boundaries of invariant sets also have high observability of flow-field parameters under Lagrangian position measurements.

Vehicle guidance along invariant-set boundaries requires a path-following controller. Previous works [61, 62] developed such controllers for a variety of vehicle models, but without significant flow-field influence on the vehicle. Chapter 7 constructs a hybrid controller to guide the vehicle modeled as a self-propelled particle along set boundaries while allowing for periodic re-assessment of the selected route, in the presence of a time-invariant flow field with spatial nonuniformity. The hybrid steering controller includes a streamline controller and a stream-function-value controller. The streamline controller is a novel application of an existing transformation of the vehicle speed and heading relative to the flow [63] and an existing flow-free steering algorithm [62] to a time-invariant flow field. The vehicle drives to a unique, closed streamline of the flow by building a Bertrand family of curves extended from the target curve. The streamline should be a simple, closed, regular curve. Section 5.2.1 analytically establishes the region of validity for the streamline controller by proving that within this region a unique closest point on the curve exists, extending the existing control law [62] to non-convex, closed streamlines in a flow field. The stream-function-value controller guides the vehicle to the valid region of the streamline controller. Together, the streamline controller and the stream-function-value controller are a hybrid control strategy that generates candidate trajectories guided to highly observable regions of the flow field, the invariant-set boundaries.

1.3 Contributions of dissertation

This dissertation provides research contributions in the general areas of robotic fish design, observability-based path planning, and adaptive sampling for environmental monitoring. The main results of this dissertation have been published or submitted for publication in archival journals [64–66]. Earlier research results related to this dissertation appeared in conference proceedings [67–70]. Some additional discussion and results appear in this dissertation that have not appeared elsewhere. Unless otherwise stated, the following claims of contribution were performed together with colleagues in the aforementioned publications.

We study flow-field estimation by bioinspired robotic fish using distributed sensor arrays. We also explore how the feedback of flow-field information can be used to achieve primitive, bioinspired behaviors, such as rheotaxis. Specifically, we develop a pressure-difference measurement model for interfacing potential-flow models with distributed arrays of pressure sensors for estimation. We use empirical observability analysis of a potential-flow model of a hydrofoil in uniform flow to optimize pressure-sensor placement. We develop an output-feedback-control framework for achieving rheotaxis in an unknown, uniform flow field. We experimentally demonstrated rheotaxis using symmetric and asymmetric sensor arrays. These contributions preceded subsequent collaborative works that investigated the use of multimodal artificial lateral lines [23], station holding by a robotic fish [23], and the closed-loop self-propulsion of a flow-sensing robotic fish [25, 71, 72].

We also study the model-predictive control technique known as observability-based path planning in which a mobile robotic platform seeks to gain information about a spatiotemporal process present in its environment. In the context of sampling for the purpose of flow-field estimation, we provide an example that shows how the inclusion of the vehicle's sampling history in observability-based path planning can alter its selected path. We pose the question of how best to incorporate prior sampling information in observability-based path planning, especially when the true state or model parameters under study are uncertain. To address this question, we solve a continuous-time variational data assimilation problem in terms of the linear stochastic observability Gramian with an inverse background error covariance, which together we refer to as augmented observability. We provide an analytical solution to the continuous-time Kalman filter Riccati equation for a linear time-varying system with deterministic dynamics and uncertain measurements in terms of the stochastic observability Gramian, and we compare anticipated-covariance path planning to observability-based path planning using this solution. We extend augmented observability to nonlinear systems by utilizing the empirical observability Gramian, yielding a novel method for scoring candidate trajectories, the empirical augmented unobservability index. I also provide an analytical connection between empirical augmented observability and Fisher information. These contributions are important because they provide a quantitative evaluation criterion for automatic selection of the candidate path that maximizes the anticipated observability given existing state uncertainty. The strategy of path planning with empirical augmented observability is illustrated for a single vehicle in a two-vortex flow pertinent to ocean sampling.

We additionally study the problem of adaptive Lagrangian sampling for flow-field estimation to answer the question of where to steer vehicles that use their own positions as measurements to estimate most accurately the underlying flow field. We consider the estimation of the locations and strengths of two co-rotating vortices as an example system. We propose an adaptive-sampling framework that includes a nonlinear/non-Gaussian estimator to handle flow-field nonlinearities. The framework also exchanges full probability density functions (pdf) describing the state/parameter uncertainty between the estimating and planning functional blocks. We refer the the planning functional block as the Augmented-Observability Planner (A-OP). Within the A-OP, we identify regions of high flow-field observability for Lagrangian measurements as coherent structures that divide the flow. We develop a hybrid steering controller for time-invariant flows that directs a self-propelled vehicle along separatrices of the two-vortex flow field. The A-OP uses a hybrid steering controller to simulate steering to these target streamlines as a means of generating candidate control inputs. We implement augmented observability-based path planning for non-Gaussian probability densities by performing an approximate expected cost calculation over the empirical augmented unobservability index for each candidate control. This calculation yields a novel approach to observability-based path evaluation that weights candidate paths with reference to how anticipated observability gains complement existing information represented by non-Gaussian densities. Numerical experiments on a single vehicle in the two-vortex flow demonstrate the benefits of each component in the proposed sampling framework.

1.4 Outline of dissertation

Chapters 2 and 3 provide background information utilized throughout this dissertation. The topics collected in Chapters 2 and 3 represent existing knowledge upon which subsequent chapters build. Chapter 4 presents an application implementing output feedback control of a robotic fish for the task of rheotaxis. Chapter 5 details how to perform observability-based path planning in an uncertain potential-flow field. Chapter 6 derives a theoretically justified method for incorporating prior information in empirical observability analysis. Chapter 7 applies augmented observability analysis within an adaptive-sampling framework for estimating a two-vortex flow, a problem pertinent to ocean sampling. Chapter 8 concludes the dissertation by summarizing the contributions and discussing directions for future research.

Chapter 2 provides necessary background for the modeling of fluid flows and vehicles in the plane. This chapter employs the notational convenience of complex-variable mathemetics, for which there is additional background in Appendix A. Stream functions and potential-flow theory form the basis of the reduced-order fluid modeling used in this dissertation. Section 2.1 presents the background needed to represent flow fields using stream functions. Section 2.2 introduces potential-flow theory, velocity potential functions, and complex potential functions. Section 2.3 specializes potential flow to planar flow fields that contain vortical structures. Self-propelled particle models representing the dynamics of an abstracted vehicle in the plane are presented in Section 2.4.

Chapter 3 details state estimation techniques that are useful for output-feedback control. Section 3.1 presents multiple topics from estimation theory, including recursive Bayesian filtering and the Gaussian Mixture Kalman Filter (GMKF). These estimation tools feature prominently in the output-feedback approaches of this dissertation to both vehicle-scale and long-range flow sensing. Chapter 3 concludes with Section 3.2 by discussing observability, both classical linear observability and the approximate extension of linear observability to nonlinear systems, known as empirical observability.

As an application, rheotaxis encapsulates many of the challenges of vehicle-scale flow sensing and control highlighted in Section 1.1. To achieve rheotaxis on a bioinspired robotic fish, Section 4.1 constructs a potential-flow model of flow past the body of a fish and derives a pressure-difference measurement equation for obtaining flow-sensing information from a distributed sensor array. Section 4.3 details the construction of a flow-sensing and control test bed used in experiments. Section 4.4 evaluates the potential-flow model against experimental data as well as against data collected from Computational Fluid Dynamic (CFD) simulations. Section 4.2 performs observability-based sensor placement of pressure sensors on the body of the robotic fish using the potential-flow model. Section 4.5 proposes our framework for closed-loop rheotaxis, and Section 4.6 presents experimental data for the framework using both symmetric and asymmetric sensor arrays.

Chapter 5 discusses how to perform GNC of a self-propelled particle model of a vehicle in an uncertain potential-flow field. Section 5.3 discusses observability-based path planning and presents results illustrating the most informative regions of a flow field from which a Lagangian sensor can sample. These regions are the separating boundaries of invariant sets, including close approaches along the stable manifolds of saddle points. Section 5.2 derives a hybrid steering controller. The first component of this hybrid controller is a steering controller that converges to a unique streamline. Section 5.2 also derives analytical expressions for the region of validity of the controller based on the curvature characteristics of the target streamline. The second component of the hybrid controller applies outside of the region of validity and steers the vehicle to within a region of validity for the first controller in the hybrid strategy.

Chapter 6 poses the question of how one can incorporate prior information with a forward-looking observability analysis in observability-based path planning. Section 6.3 provides background on the error covariance matrix and the stochastic observability Gramian. Additionally, Section 6.3 presents the solution to an optimal, linear data assimilation problem known as Incremental 4D-Var. The Incremental 4D-Var formalism for optimal, initial-condition inference provides an answer of how to incorporate prior information for Gaussian uncertainty—combine the stochastic observability Gramian with the inverse of the covariance associated with the initial condition estimate. An appropriate name for this new matrix is the augmented observability Gramian since the observability Gramian is augmented with a prior covariance. Section 6.3 extends the augmented observability Gramian to the nonlinear case by replacing its stochastic observability Gramian with the empirical observability Gramian. Section 6.4 connects augmented observability with two other inference matrices: the Fisher information matrix, and the Kalman Filter covariance. Section 6.5 introduces a novel measure for observability-based path planning with prior information, known as the empirical augmented unobservability index, and it also provides an upper bound on this quantity. Section 6.5 also performs a numerical experiment to demonstrate that augmented observability-based path planning yields the desired planning decisions. Section 6.6 concludes the chapter by extending augmented observability-based path planning to non-Gaussian prior pdfs approximated by Gaussian Mixture Models (GMMs).

Chapter 7 addresses the application of adaptive sampling with a guided Lagrangian sensor for ocean-state estimation. Section 7.1 presents the framework designed to solve this problem, consisting of a nonlinear/non-Gaussian estimator and the A-OP. The A-OP identifies high-observability regions of the flow field for sampling, simulates steering to each of these regions for several, possible state realizations, and performs an augmented observability analysis with expected cost to choose the control that minimizes the empirical augmented unobservability index. Section 7.2 demonstrates the performance gains for each element of the adaptive-sampling framework by conducting Monte Carlo experiments in a two-vortex flow.

Chapter 8 concludes the dissertation. Section 8.1 summarizes the primary contributions of this work. Section 8.2 discusses directions for future research. A direction for future research in vehicle-scale flow sensing entails the use of higher-fidelity reduced-order flow models within the control loop. Another direction moves closer to estimation of an unknown flow field by considering the additional problem of model selection using sensor data. The primary direction for future research in long-range flow sensing involves incorporating additional, cooperative vehicles in the estimation of the flow environment while using augmented observability-based guidance.

Supplemental materials are provided for the reader in the appendices. Appendix A reviews complex-variable mathematics and includes a list of useful mathematical identities. Appendix B details how to extract boundary targets for steering in the two-vortex example from Chapter 7. Appendix C contains rationale for the parameter values selected in the numerical experiments performed in Section 7.2.

A terminology index appended to the end of the dissertation can assist the reader in readily locating material thoroughout the text.

Chapter 2

Modeling of fluid flows and vehicles in the complex plane

This chapter presents necessary background on topics of fluid-flow modeling and vehicle modeling in the complex plane. Complex variables can compactly represent simplified fluid dynamic models in the plane. The tools for modeling planar fluid flows arise in Chapters 4 (which uses potential-flow theory), 5 (which uses stream functions), 6 (which uses a two-vortex flow), and 7 (which uses stream functions and a two-vortex flow). This chapter models planar flows using a stream function under assumptions of steady, incompressible flow. This chapter also introduces potential flow theory, which is useful for constructing fluid models additively under an assumption of irrotationality. Point-vortex flows are potential flows that have all circulation of the flow field concentrated at vortex singularities. This chapter also describes the two-vortex system, which is a point-vortex flow useful for studying path planning of autonomous vehicles.

Modeling an abstracted autonomous vehicle using complex variables provides unified approach to studying path planning for an autonomous vehicle in the presence of planar fluid flows. This chapter details the self-propelled particle model, a steering controller for converging to a level-set of a scalar-valued function in the plane, and a control transformation for steering a self-propelled particle in the presence of a flow field.

In an effort to keep the dissertation self-contained, Appendix A provides an overview of more fundamental concepts from complex-variable mathematics.

2.1 The stream function for steady, incompressible flows

Stream lines provide curves connecting the velocity vectors in an instantaneous flow field, and they represent level-set values of a scalar function known as a *stream function*. The stream function is useful for specification of a flow field because spatial differentiation returns the full velocity field in the domain. This section derives the relation between the stream function and the velocity field in complex variables since many texts only use complex variables for potential-flow theory (see Section 2.2). In the following, the stream function applies more generally than to potential flows alone. Specifically, the adaptive-sampling framework in Chapter 7 utilizes a stream function for a steady and incompressible flow in the plane; an additional potential-flow (irrotationality) assumption is not needed.

Consider a steady, planar flow described by a spatial (Eulerian) velocity field, $f(z, \bar{z})$, evaluated at $z = x + iy$. The constraint that a streamline is everywhere tangent to the flow velocity implies that there is no flow perpendicular to a streamline. Rotating the flow vector by i provides the perpendicular flow, if, and the constraint of no flow perpendicular to a streamline becomes

$$\langle if, dz\rangle = 0. \tag{2.1}$$

Equation (2.1) can be simplified using (A.1) and scaled to yield

$$-2i\bar{f}dz + 2ifd\bar{z} = 0, \tag{2.2}$$

which closely resembles the exact differential of a scalar-valued complex function ψ [73]

$$d\psi = \frac{\partial\psi}{\partial z}dz + \frac{\partial\psi}{\partial\bar{z}}d\bar{z}. \tag{2.3}$$

The equality of an exact, scalar differential to zero would imply the existence of a function that is constant along streamlines. However, one cannot directly equate the coefficient terms of (2.2) and (2.3) unless the spatial derivatives of these coefficients (equivalently, the mixed, second partial derivatives of ψ) also agree, providing the constraint

$$\frac{\partial^2\psi}{\partial z\partial\bar{z}} = \frac{\partial(-2i\bar{f})}{\partial\bar{z}} = \frac{\partial(2if)}{\partial z}, \tag{2.4}$$

or

$$\frac{\partial f}{\partial z} + \frac{\partial\bar{f}}{\partial\bar{z}} = 0. \tag{2.5}$$

Equation (2.5) is $\langle\partial/\partial\bar{z}, f\rangle = 0$, thereby representing a zero-divergence condition that is equivalent to the steady continuity equation in the plane under an assumption of incompressibility of the fluid.

When Equation (2.5) is satisfied, a scalar-valued function ψ satisfying $d\psi = 0$ exists and one may derive the flow velocity vectors from ψ by equating coefficients in (2.2) and (2.3). Spatial differentiation of ψ recovers the velocity field, and an incompressible, time-invariant flow f in $\mathbb{C}$ may be conveniently represented in terms of a stream function $\psi = \psi\,(z, \bar{z})$ by [74, 75]

$$f(z, \bar{z}) = -2i \frac{\partial \psi}{\partial \bar{z}}(z, \bar{z}). \tag{2.6}$$

2.2 Potential-flow models in the plane

Equation (2.6) provides a convenient method for prescribing the flow-velocity field through the use of a stream function. Another convenient way to prescribe a flow field is by specifying a velocity potential $\phi(z, \bar{z})$ such that the gradient of this function provides the flow

$$f = 2\frac{\partial \phi}{\partial \bar{z}}. \tag{2.7}$$

A flow that admits representation (2.7) is a *potential flow*. An important assumption that the flow is *irrotational* is implicit in this representation.

Let $\mathrm{curl}_{\mathbb{C}} : \mathbb{C} \to \mathbb{R}$ be an operator over the $\mathbb{C}$ plane, such that

$$\mathrm{curl}_{\mathbb{C}} f := 2\left\langle i\frac{\partial}{\partial \bar{z}}, f \right\rangle. \tag{2.8}$$

Confined to the $\mathbb{C}$ plane, the result of this operation corresponds with the scalar component of the usual curl operation from vector calculus when applied to vectors in the plane. This scalar value, known as the *vorticity*

$$\omega(z,\bar{z}) = \mathrm{curl}_{\mathbb{C}} f(z,\bar{z}), \tag{2.9}$$

describes the rotational character of the flow field f. If f admits representation (2.7), calculate the vorticity field by substitution,

$$\begin{aligned}
\omega &= \mathrm{curl}_{\mathbb{C}}\left(2\frac{\partial \phi}{\partial \bar{z}}\right) \\
&= -i\frac{\partial}{\partial z}\left(2\frac{\partial \phi}{\partial \bar{z}}\right) + i\frac{\partial}{\partial \bar{z}}\left(2\frac{\partial \phi}{\partial z}\right) \\
&= -2i\frac{\partial^2 \phi}{\partial z \partial \bar{z}} + 2i\frac{\partial^2 \phi}{\partial \bar{z} \partial z} \\
&= 0.
\end{aligned}$$

Therefore, a potential flow is necessarily an irrotational flow.

A steady, planar flow that is both incompressible and irrotational is called an *ideal flow*. Such a flow possesses both a velocity potential ϕ and a stream function ψ. Equating the expressions of the flow velocity

$$f = -2i\frac{\partial \psi}{\partial \bar{z}} = 2\frac{\partial \phi}{\partial \bar{z}}, \tag{2.10}$$

yields the constraint

$$\frac{\partial}{\partial \bar{z}}(\phi + i\psi) = 0, \tag{2.11}$$

which matches the Cauchy-Riemann relation (A.4) for the composite function $w(z) =$

$\phi(z,\bar{z})+i\psi(z,\bar{z})$. The composite function $w(z)$ is an analytic function known as a *complex potential*.

The complex potential yields the conjugate flow via

$$\bar{f}=\frac{dw}{dz}. \tag{2.12}$$

One may also recover the velocity potential and stream function via

$$\phi(z,\bar{z})=\frac{1}{2}\left(w(z)+\overline{w(z)}\right), \tag{2.13}$$

and

$$\psi(z,\bar{z})=\frac{1}{2i}\left(w(z)-\overline{w(z)}\right). \tag{2.14}$$

A notable attribute of potential flow is the additivity of complex potentials; the sum of two complex potentials yields another, valid complex potential describing the combined flow field. For example, the complex potential for a stationary source of strength Λ at the orgin is $\Lambda\log(z)$, and the complex potential for a uniform flow of speed U is Uz. Together, $(\Lambda\log(z)+Uz)$ gives the complex potential for a stationary source within uniform flow.

2.3 Point-vortex flows

Point-vortex flows are flows that have circulating character and are nearly irrotational with vorticity concentrated only at the isolated centers of vortices. Without an assumption of irrotational flow, consider the expression for the vorticity field of a planar flow in terms of the stream function

$$\omega = \mathrm{curl}_{\mathbb{C}}\left(-2i\frac{\partial\psi}{\partial\bar{z}}\right) = -4\frac{\partial^2\psi}{\partial z\partial\bar{z}} \tag{2.15}$$

The right-hand side of (2.15) is the complex equivalent of the negative of a Laplacian operator [76], making (2.15) a Poisson partial-differential equation, for which the solution in the plane can be expressed in terms of the Green's function $1/(2\pi|z-\xi|^2)$ [74]

$$\psi(z,\bar{z}) = \int \frac{1}{2\pi|z-\xi|^2}\omega(\xi)d\xi. \tag{2.16}$$

To create a nearly irrotational flow with circulating character, let vorticity exist only at isolated points in the flow, called point vortices. The integral of vorticity within an enclosed area is circulation Γ. A point vortex j has circulation Γ_j concentrated at its center. The superposition of point vortices located at z_j for $j = 1, \ldots, N$ yields the total vorticity field

$$\omega(z) = \sum_{j=1}^{N}\Gamma_j\delta(z-z_j), \tag{2.17}$$

where δ is a Dirac delta function. Insertion of (2.17) into (2.16) with evaluation of the integral results in the stream function for a flow field containing N stationary vortices

$$\psi(z,\bar{z}) = \sum_{j=1}^{N}\frac{-\Gamma_j}{2\pi}\log|z-z_j|. \tag{2.18}$$

2.3.1 The two-vortex system

The two-vortex system is a potential-flow model of two interacting ocean eddies. It is useful in studying idealized path planning of ocean vehicles, because it is analytically tractable and (when viewed in a co-rotating frame) contains coherent flow structures [70]. These coherent structures are important barriers to transport that also play a role during path planning. Further, the two-vortex system is a natural extension of prior works on observability-based path planning in a uniform flow [27] and in the presence of a single, stationary point vortex [7]. The two-vortex model appears in the research of Chapters 6 and 7.

Let z represent a location in the complex plane $\mathbb{C}$. Let z_1 and z_2 be the locations of two point vortices with circulation strengths Γ_1 and Γ_2, respectively. Applying (2.18) to the two-vortex case gives the stream function

$$\psi\left(z,\bar{z}\right) = -\frac{1}{2\pi}\left(\Gamma_1 \log|z-z_1| + \Gamma_2 \log|z-z_2|\right). \tag{2.19}$$

Making use of (2.6), the flow felt by a drifting vehicle at location z becomes

$$f(z,\overline{z}) = \frac{i\Gamma_1}{2\pi}\frac{z-z_1}{|z-z_1|^2} + \frac{i\Gamma_2}{2\pi}\frac{z-z_2}{|z-z_2|^2}. \tag{2.20}$$

The flow-field specification (2.20) according to stream function (2.19) allows evaluation if z_1 and z_2 are known. However, the vortices are also interacting; vortices advect according to the flow of other vortices. The flow at z due to an isolated vortex j at z_j

with circulation strength Γ_j is

$$f_j(z,\overline{z}) = \frac{i\Gamma_j}{2\pi}\frac{z - z_j}{|z - z_j|^2}. \tag{2.21}$$

Each vortex in the two-vortex system is influenced by the flow of the opposing vortex only. Evaluation of the flow $f_j(z,\overline{z})$ at each vortex location z_j under the influence of the opposing vortex $q \neq j$, leads to the two-vortex dynamics

$$\dot{z}_j = -\frac{i\Gamma_q}{2\pi}\frac{z_j - z_q}{|z_j - z_q|^2}, \tag{2.22}$$

for $j, q = 1, 2$ with $j \neq q$.

Under dynamics (2.22), vortices with same-signed circulation strengths rotate in a relative equilibrium (i.e., an equilibrium in a reduced set of variables) around a shared center of vorticity [74]

$$z_{\text{cv}} = \frac{\Gamma_1 z_1 + \Gamma_2 z_2}{\Gamma_1 + \Gamma_2}. \tag{2.23}$$

Let

$$\omega = \frac{\Gamma_1 + \Gamma_2}{2\pi|z_1 - z_2|^2} \tag{2.24}$$

be the angular rate of rotation of the vortex pair about z_{cv}. During this motion, the distance between the vortices $d = |z_1 - z_2|$ is conserved. The transformation

$$z(t) = \xi(t)e^{i(\omega t + \phi)} + z_{\text{cv}} \tag{2.25}$$

maps between the inertial frame and a reference frame that co-rotates with the vortices around z_{cv}, where $\xi(t)$ is the complex variable in the co-rotating frame, and ϕ is an initial phase angle of the vortex pair.

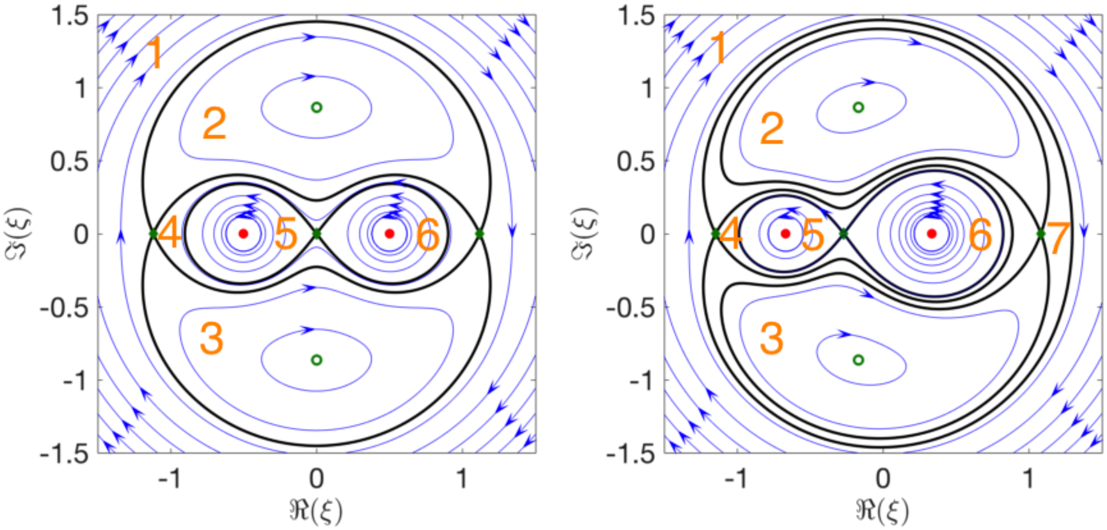

(a) $\Gamma_2 = \Gamma_1$ (b) $\Gamma_2 = 2\Gamma_1$

Figure 2.1: Flow-field geometry for the two-vortex system in the co-rotating frame; red circles are vortices; green circles and green diamonds are center and saddle fixed points, respectively; black lines are the stable and unstable manifolds of the saddle points.

In the co-rotating frame, invariant regions appear as enumerated in Figure 2.1. Figure 2.1(a) shows the streamlines for two equal-strength vortices. The black lines represent separating boundaries or separatrices, which divide the six invariant regions for this case. A vehicle drifting within an invariant region may escape the region only if control actions are taken. The separatrices represent the stable and unstable manifolds for the saddle points. Note that five fixed points are present: two center fixed points are shown as green circles, and three saddle fixed points are shown as green diamonds. Figure 2.1(b) shows a similar portait for two vortices with the same-signed circulation but unequal strengths $\Gamma_1 < \Gamma_2$. An additional invariant set forms and the origin of the frame shifts towards the stronger vortex.

A first-order model for the motion of a drifting vehicle is

$$\dot{z} = f. \tag{2.26}$$

Under the frame transformation (2.25), these kinematics in the co-rotating frame are $\dot{\xi} = f - i\omega\xi$. One may alternately write $\dot{\xi} = f_R$, where $f_R = f - i\omega\xi$ defines a flow in the co-rotating frame. In the co-rotating frame, the stream function corresonding to f_R via the stream-function-flow relation (2.6) is [65]

$$\psi_R\left(\xi, \bar{\xi}\right) = -\frac{1}{2\pi}\left(\Gamma_1 \log|\xi - \xi_1| + \Gamma_2 \log|\xi - \xi_2|\right) + \frac{\omega}{2}|\xi|^2, \tag{2.27}$$

where ξ_1 and ξ_2 are the locations of the vortices in this frame.

For Lagrangian sampling in the two-vortex system, the full system state (including both vortices and a sampling vehicle) is given by

$$(\Gamma_1, z_1, \Gamma_2, z_2, z)^T, \tag{2.28}$$

where z represents the location of a drifting vehicle. The state of this system may also be represented by the real-valued vector

$$x = (\Gamma_1, \Re(z_1), \Im(z_1), \Gamma_2, \Re(z_2), \Im(z_2), \Re(z), \Im(z))^T \tag{2.29}$$

when convenient. For a controlled vehicle, the state vector also includes the heading, which the next section addresses. All dynamical calculations for the two-vortex system in this dissertation, including observability calculations in Chapters 5, 6, and 7, are performed in the inertial frame and converted to the co-rotating frame only for plotting.

2.4 Steering-controlled guidance with self-propelled particle models

Planning planar routes for an autonomous vehicle can readily be accomplished by abstracting away the vehicle and replacing it with a particle model that has nominal forward speed ρ and steering as the primary control input. This abstraction, known as the *self-propelled particle model*, allows the engineer to focus on high-level vehicle guidance by removing vehicle-specific dynamics. However, the simplified model of the vehicle retains the necessary constraint that the vehicle cannot instantaneously move side-to-side; it can only turn while propelling forward. Typically, one assumes that lower-level controllers will be used for navigation and control of the vehicle when the planned paths are executed.

The planar, self-propelled particle model for a vehicle at $z \in \mathbb{C}$ with speed ρ is [7]

$$\begin{aligned} \dot{z} &= \rho e^{i\beta} \\ \dot{\beta} &= v, \end{aligned} \tag{2.30}$$

where v is a steering input and β is the heading relative to the x axis. This model represents a vehicle under gyroscopic steering control.

2.4.1 Self-propelled particle model with flow

This section presents a self-propelled particle model in the presence of an underlying flow field and shows a connection to the self-propelled particle model without flow. Consider a sampling platform with self-propulsive speed α located at $z \in \mathbb{C}$ and advected with the flow. The self-propelled particle model (2.30) may be modified to include the influence of an underlying flow velocity f on the vehicle according to [7, 63]

$$\begin{aligned} \dot{z} &= \alpha e^{i\theta} + f \\ \dot{\theta} &= u, \end{aligned} \tag{2.31}$$

where θ is the counter-clockwise angle from the positive real axis to self-propulsive direction and u is a steering-rate control.

Paley and Peterson [63] construct a method for compensating for the influence of the flow by defining the variables in (2.30) to be the total vehicle speed $\rho = |\alpha e^{i\theta} + f|$, the total velocity angle $\beta = \arg(\alpha e^{i\theta} + f)$, and the flow-relative control input v. These definitions transform the model (2.31) with flow into the model (2.30) without flow. The control inputs of the two models are related by [63]

$$u = \frac{v - \left\langle \dot{f}, ie^{i\beta} \right\rangle}{1 - \rho^{-1} \left\langle f, e^{i\beta} \right\rangle}, \tag{2.32}$$

where $\dot{f} = (\partial f/\partial z)\,\dot{z} + (\partial f/\partial \bar{z})\,\dot{\bar{z}}$. Note that (2.32) has a singularity if the vehicle is unable to make forward progress, that is, if $\langle f, e^{i\beta} \rangle = \rho$ or equivalently, if $\langle f, e^{i\theta} \rangle = -\alpha$ [63]. In strong flows for which the vehicle may not always be able to make forward progress, a saturation function may be applied to u to handle large control excursions [7].

2.4.2 Steering along a level-set of a scalar field

A useful control objective for guidance of an autonomous vehicle represented by a self-propelled particle model is to steer the vehicle along a level-set of a scalar field. Such a scalar field may be defined by a virtual function designed to specify vehicle paths or tracks that the vehicle may follow during surveillance or sampling missions. The control design task then requires that the vehicle converge to a specified level-set of the scalar-valued function. This section describes an existing control law that achieves this objective for a user-defined scalar-valued function defined over the plane.

Let $a_1 = e^{i\beta}$ be the velocity orientation vector. Under the constraint $a_2 = ia_1$, the unit vectors $a_1, a_2 \in \mathbb{C}$ define a path frame for the vehicle. The dynamics of the path-frame vectors are [77]

$$\begin{aligned} \dot{a}_1 &= va_2 \\ \dot{a}_2 &= -va_1. \end{aligned} \tag{2.33}$$

The solutions of (2.30) and (2.33) describe the evolution of the vehicle and its path frame.

Zhang and Leonard [77] use a self-propelled particle model similar to (2.30) and a path frame similar to (2.33) to derive a control law in a scalar field $\Theta(z, \bar{z})$ that navigates the vehicle to the level-set $\{z : \Theta(z, \overline{z}) = \Theta^d\}$ for a desired field value Θ^d.[1] This control law applies to a vehicle that may have nonconstant speed ρ. The control law of [77] makes use of the following frame constructions. Consider the path frame (a_1, a_2) of a vehicle located at $z \in \mathbb{C}$ and construct a secondary frame (b_1, b_2) also located at z, such that b_2 points in the direction of the gradient of the field and b_1 is a clockwise rotation of b_2, i.e.,

$$\begin{aligned} b_1 &= -ib_2 \\ b_2 &= \frac{\frac{\partial\Theta}{\partial\bar{z}}}{|\frac{\partial\Theta}{\partial\bar{z}}|}. \end{aligned} \tag{2.34}$$

Let η represent the angle from a_1 to the b_1 direction such that

$$\begin{aligned} \cos\eta &= \langle a_2, b_2\rangle &&= \langle a_1, b_1\rangle \\ \sin\eta &= \langle a_2, b_1\rangle &&= -\langle a_1, b_2\rangle\,. \end{aligned} \tag{2.35}$$

Figure 2.2 depicts these definitions, with $\Re(\cdot)$ and $\Im(\cdot)$ denoting the real and imaginary operators, respectively. Zhang and Leonard [77] consider how the angle η changes and how the scalar field value Θ changes as the vehicle moves to derive the following theorem.

Theorem 1 (Zhang and Leonard [77]). *Suppose a scalar field $\Theta(z, \overline{z})$ is defined over a connected subset of $\mathbb{C}$ with extrema $-\infty \leq \Theta_{min} < \Theta_{max} \leq \infty$. Further, assume $|\partial\Theta/\partial\bar{z}| < \infty$ and $|\partial^2\Theta/\partial z\partial\bar{z} + \partial^2\Theta/\partial\bar{z}^2| < \infty$ with $|\partial\Theta/\partial\bar{z}| \neq 0$ except at a finite number of points where either Θ_{min} or Θ_{max} is attained. Let $\Pi(\Theta)$ be a scalar function meeting the technical requirements:*

---

[1] This section presents the work of [77] in the form of complex variables.

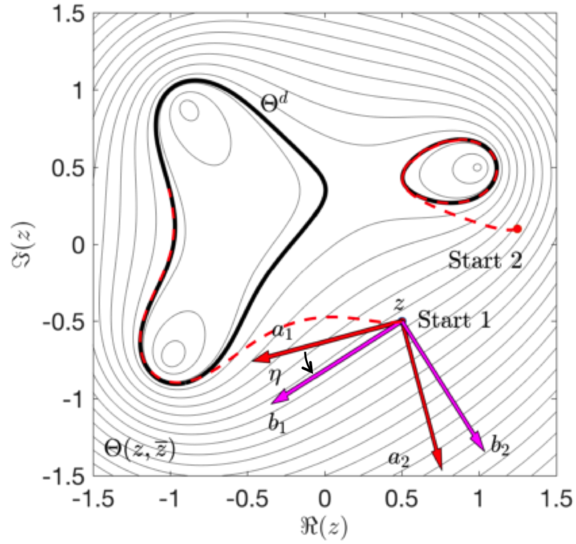

Figure 2.2: Nomenclature used in control laws for steering to a desired level-set.

(i) $g(\Theta)$ *is a locally Lipschitz continuous function on* $(\Theta_{min}, \Theta_{max})$ *so that* $\Pi(\Theta)$ *is continuously differentiable on* $(\Theta_{min}, \Theta_{max})$*;*

(ii) $g(\Theta^d) = 0$ *and* $g(\Theta) \neq 0$ *if* $\Theta \neq \Theta^d$*;*

(iii) $\lim\limits_{\Theta \to 0} \Pi(\Theta) = \infty$, $\lim\limits_{\Theta \to \infty} \Pi(\Theta) = \infty$ *and* $\exists \check{\Theta}$ *such that* $\Pi\left(\check{\Theta}\right) = 0$.

Assume $\eta(t_0) \neq \pi$ *and* $|\partial\Theta/\partial\bar{z}| \neq 0$ *initially. Then, the steering control law*

$$v = \rho\left(\kappa_a \cos\eta + \kappa_b \sin\eta - 4\left.\frac{d\Pi}{d\Theta}\right|_{\Theta(z)} \left|\frac{\partial\Theta}{\partial\bar{z}}\right| \cos^2\frac{\eta}{2} + K_1 \sin\frac{\eta}{2}\right), \tag{2.36}$$

with

$$\begin{aligned}
\kappa_a &= \frac{-1}{\left|\frac{\partial\Theta}{\partial\bar{z}}\right|}\left\langle b_1, \frac{\partial^2\Theta}{\partial z\partial\bar{z}} b_1 + \frac{\partial^2\Theta}{\partial\bar{z}^2}\bar{b}_1\right\rangle \\
\kappa_b &= \frac{1}{\left|\frac{\partial\Theta}{\partial\bar{z}}\right|}\left\langle b_1, \frac{\partial^2\Theta}{\partial z\partial\bar{z}} b_2 + \frac{\partial^2\Theta}{\partial\bar{z}^2}\bar{b}_2\right\rangle,
\end{aligned}$$

steers the self-propelled vehicle model (2.30) *such that* $\eta \to 0$ *and* $\Theta \to \Theta^d$ *as* $t \to \infty$*.*

Figure 2.2 shows two simulations of a vehicle steering under control law (2.36) with different start locations and the same Θ^d value. The ultimate closed curve for the Θ^d level set that the vehicle steers to depends on the initial condition. Section 5.2.2 utilizes this theorem to construct two new controllers: the first controller drives the vehicle through a flow field to a unique, closed streamline of the flow, and the second controller drives the vehicle to be within the applicable range of the first controller, if it is not already within range. These two controllers combine in a hybrid control strategy that Chapter 7 incorporates in a guided-sampling framework.

Chapter 3

State estimation and observability

To learn about a surrounding fluid environment, autonomous vehicles must take measurements of the flow with sensors or through their own motion. By comparing these measurements to anticipated values derived from various realizations of a flow model, the vehicle may assess the most likely state of the fluid system (or the most likely model parameter values). These comparisons comprise the task of flow-field estimation. This chapter presents two powerful methods for nonlinear/non-Gaussian state estimation that may be used in conjunction with a fluid flow model to achieve flow-field estimation. This chapter also describes the use of the state- or parameter-vector estimate for feedback, which is also called output-feedback control.

Observability can describe the ability of the vehicle to infer the true initial state of the fluid surroundings by collecting flow measurements over a specified time interval. If the flow measurements provide enough information to infer uniquely the true initial condition or the true parameters of the flow field, then the vehicle has observability of the flow field. This chapter introduces observability and a numerical approximation to observability, known as empirical observability. Empirical observability is a tool that the vehicle may use to assess informative regions for sampling or which candidate control signal will lead to the best sampling trajectory for the vehicle.

3.1 Output-feedback control using nonlinear/non-Gaussian filters

Output-feedback control refers to the use of a state estimate based on output measurements in a state feedback controller [78]. The flow field surrounding an underwater vehicle is often unknown, so control action based on flow-field information necessarily requires estimation of the flow-field state or parameter vector. Chapter 4 provides an application of estimating the angle of a robotic fish relative to an oncoming flow to feedback to the controller. Similarly, Chapter 7 provides an application of estimating vortex states and strengths by an ocean vehicle guided to take informative measurements of its surrounding flow field.

Consider the stochastic system

$$\begin{aligned} \dot{x}(t) &= A(t)x(t) + G(t)w(t) \\ y(t) &= C(t)x(t) + v(t), \end{aligned} \tag{3.1}$$

where $x(t) \in \mathbb{R}^n$ is the state vector, $y(t) \in \mathbb{R}^p$ is the output vector, $A(t)$, $G(t)$, and $C(t)$ are real-valued, time-varying matrices and, $w(t)$ and $v(t)$ are white Gaussian noise vectors with covariances $Q(t)$ and $R(t)$, respectively. The state $x(t)$ and the measurement $y(t)$ are both stochastic processes due to randomness injected by the process noise $w(t)$ and the measurement noise $v(t)$.

The true state $x(t)$ in (3.1) is uncertain because of uncertainties in the initial condition, process noise $w(t)$, and measurement noise $v(t)$. *Filtering* refers to generating an estimate $\hat{x}(t)$ of the unknown state vector $x(t)$ at the current time t using the measurement $y(t)$ and prior uncertainties. System (3.1) possesses certain favorable characteristics: dynamics that are affine in $x(t)$, an output equation that is affine in $x(t)$, and additive, white Gaussian noise in both the dynamics and the measurements. With such structure, the optimal filtering algorithm is the Kalman Filter [79], which is the minimum-variance, unbaised estimator for producing continuous-time estimates $\hat{x}(t)$ given system (3.1). The uncertainties in the estimate are captured by the state error covariance $P(t)$, which the Kalman Filter also provides. Chapter 6 re-visits the continuous-time Kalman Filter for the case of deterministic dynamics to make comparisions between its covariance $P(t)$ and a novel concept, known as augmented observability.

Consider the stochastic, nonlinear system

$$\begin{aligned} \dot{x}(t) &= g(t, x(t)) + G(t)w(t) \\ y(t) &= h(t, x(t)) + v(t), \end{aligned} \tag{3.2}$$

where g and h are nonlinear, real-valued, vector functions. A *nonlinear filter* addresses systems in which the dynamics function is nonlinear or the observation function is nonlinear, or both [80]. Note that one may also estimate parameters of the system dynamics in (3.2) by creating an augmented state vector that includes the parameters and appending zero dynamics.

Nonlinear dynamics and nonlinear observation operators lead to the development of non-Gaussianity in the pdfs that characterize the state uncertainty. A filter the properly handles the uncertainties for (3.2) is referred to as a *nonlinear/non-Gaussian filter*. This dissertation uses two nonlinear/non-Gaussian filters for output-feedback control: the recursive Bayesian filter, and the Gaussian Mixture Kalman Filter. The recursive Bayesian filter appears in Chapter 4, and the Gaussian Mixture Kalman Filter appears in Chapter 7.

Although systems (3.1) and (3.2) provide continuous-time measurements, only the theoretical work of Chapter 6 considers continuous-time measurements. The applications of Chapters 4 and 7 employ continuous-time dynamics with discrete-time measurements by collecting the observations at time t_k, yielding

$$\begin{aligned} \dot{x}(t) &= g(t, x(t)) + G(t)w(t) \\ y(t_k) &= h(t_k, x(t_k)) + v(t_k). \end{aligned} \tag{3.3}$$

3.1.1 Recursive Bayesian filtering

Bayesian estimation is a probabilistic technique by which knowledge of an unknown quantity is enhanced through the assimilation of measurements [81]. Bayes' formula is [81]

$$\underbrace{\pi(x|y)}_{\text{posterior}} \propto \underbrace{\pi(y|x)}_{\text{likelihood}} \underbrace{\pi(x)}_{\text{prior}}, \tag{3.4}$$

where $\pi(\cdot)$ represents a probability density function (pdf). The central idea is to use Bayes' formula (3.4) to adjust the prior understanding of an unknown quantity x, represented in the form of a pdf, based upon the likelihood that a measurement y was generated by a nearby state of the system. Normalization of the posterior density is required to ensure the total integral of the pdf sums to unity. (The $\propto$ symbol is used to indicate a proportional relationship). In practice, grid-based Bayesian estimation discretizes a finite volume of state space or parameter space and approximates the pdf's on this grid. Normalization is performed by dividing the weight at each grid point by the total weight, summed over all grid points. Through re-arrangement of the measurement equation in (3.3), the assumption of additive Gaussian measurement noise results in a Gaussian likelihood function

$$\pi(y(t_k)|x) \propto \exp\left(-\frac{1}{2}\left(y(t_k) - h(t_k, x)\right)^T Q^{-1}\left(y(t_k) - h(t_k, x)\right)\right), \tag{3.5}$$

where Q is the measurement covariance matrix. The entries of the covariance matrix Q are typically calculated by considering the noise characteristics of data offline, prior to filtering. The t_k dependence in the term $x(t_k)$ is suppressed here because (3.5) is viewed as a function over the discretized x state space.

Collect the discrete-time measurements in set D_k such that

$$D_k = \{y(t_1), \ldots, y(t_k)\}. \tag{3.6}$$

The posterior probability density from the previous t_{k-1} assimilation time is used as the prior density for assimilation at time t_k, yielding

$$\pi(x(t_k)|D_k) \propto \pi\left(y(t_k)|x(t_k)\right)\pi\left(x(t_{k-1})|D_{k-1}\right). \tag{3.7}$$

The state evolution equation and the measurement equation together are an evolution-observation model, for which our knowledge of the system state can evolve in time and be augmented with new information through the following sequential, recursive scheme, known as Bayesian filtering [81]:

- Time evolution of the pdf (uncertainty propagation) is accomplished using the Chapman-Kolmogorov equation [81]

$$\pi\left(x(t_{k+1})|D_k\right) = \int \pi\left(x(t_{k+1})|x(t_k)\right)\pi\left(x(t_k)|D_k\right)dx(t_k), \tag{3.8}$$

- Assimilation of the observations occurs via Bayes' formula [81]

$$\pi\left(x(t_{k+1})|D_{k+1}\right) \propto \pi\left(D_{k+1}|x(t_{k+1})\right)\pi\left(x(t_{k+1})|D_k\right). \tag{3.9}$$

Note that the use of transition density $\pi\left(x(t_{k+1})|x(t_k)\right)$ in (3.8) is based on a Markov assumption in the propagation of uncertainty (i.e., the state $x(t_{k+1})$ depends only on the state $x(t_k)$) [81]. Chapter 4 implements uncertainty propagation by shifting probability mass on the discretized state space and diffusing using a Gaussian transition density. For more advanced uncertainty propagation (e.g., when probability mass does not shift uniformly across the state space), the following filter implements a nonlinear, ensemble-based approach.

3.1.2 Gaussian Mixture Kalman Filter

The Gaussian Mixture Kalman Filter (GMKF) is a nonlinear/non-Gaussian filter because it performs nonlinear forecasts of state uncertainty and it allows for non-Gaussian pdfs that commonly arise when nonlinear dynamics are present. The filter assumes a linear observation operator, which is ideal for the Lagrangian data assimilation application in Chapter 7. Gaussian mixture-based filters have previously appeared in literature in a variety of forms (see, e.g., [82], [83], or [84]). The GMKF is based primarily on the filter of Sondergaard and Lermusiaux [84], known as the GMM-DO filter because it combines Gaussian mixture models and dynamically orthogonal field equations. The GMM-DO filter differs from other mixture filters because it contains automated selection of the number of Gaussians used. We adopt the GMM-DO filter without the DO equations and instead directly propagate the state estimate.

Let w_m, $m = 1, \ldots, M$, be scalar weights such that $\sum_{m=1}^{M} w_m = 1$. Let $\underline{x}_m$ and P_m, $m = 1, \ldots, M$, be the mean vectors and covariance matrices respectively for M multivariate Gaussians $\mathcal{N}(x; \underline{x}_m, P_m)$. The weighted sum of M Gaussian densities [84]

$$p\left(x; \{(w_m, \underline{x}_m, P_m)\}_{m=1}^{M}\right) = \sum_{m=1}^{M} w_m \mathcal{N}(x; \underline{x}_m, P_m) \tag{3.10}$$

is a valid pdf known as a Gaussian mixture that integrates to unity and has an analytical representation. Through the selection of the weights, means, covariances, and number of mixture components, (3.10) can represent highly non-Gaussian distributions.

Traditional ensemble/particle-based methods represent a pdf using a sparse support of ensemble members (i.e., a Monte Carlo sampling of realizations) [80]. This representation enables nonlinear propagation of the uncertainty in the forecast step of the filter. Unfortunately, many particle filters suffer from degeneracy issues due to the sparsity of the pdf representation [80]. Kernel-based approaches address this issue by periodically creating a full density estimate from the ensemble sample so that the state space is fully supported and resampling may be performed [80]. Unfortunately, such approaches invariably require the arbitrary choice of fitting parameters such as the kernel bandwidth [84]. For Gaussian mixtures, given a specific choice for mixture complexity, an Expectation-Maximization algorithm may be applied to select automatically the weights, means, and covariances of the Gaussians to best fit the ensemble [85]. A key contribution of [84] is the use of the Bayesian Information Criterion (BIC) for the automatic selection of the mixture complexity as well. The BIC may be (approximately) expressed as [84]

$$\mathrm{BIC} = -2\sum_{j=1}^{N} \log p\left(x_j; \{(w_m, \underline{x}_m, P_m)_{\mathrm{ML}}\}_{m=1}^{M}\right) + K \log N, \tag{3.11}$$

where K is the number of parameters in the model, x_j is the jth ensemble member, $\{(w_m, \underline{x}_m, P_m)_{\mathrm{ML}}\}_{m=1}^{M}$ is the collection of maximum likelihood GMM components produced by the EM algorithm, and N is the number of ensemble members. For a multivariate

Gaussian mixture,

$$K = M\left(2n + \frac{n(n-1)}{2} + 1\right)$$

is the number of free parameters, where n is the dimension of the state vector. Note that the BIC has two components: the first component evaluates the goodness-of-fit for the model of complexity M and the second component is a penalty on the overall model complexity [84]. By sequentially evaluating models of increasing complexity, one may identify a local minimum in the BIC. One seeks the best fit of a mixture of Gaussians to the data; the model-complexity term in the BIC ensures that a simpler model is preferred [84].

Let matrix H replace the observation operator h in (3.3) since it linearly extracts the vehicle position from the state vector, i.e.,

$$y(t_k) = Hx(t_k) + v(t_k) \quad \text{with} \quad v(t_k) \sim \mathcal{N}\left(0, R(t_k)\right). \tag{3.12}$$

In the case of a single Gaussian forecast pdf, Gaussian measurement noise, and a linear observation operator, the Kalman-analysis equations represent the optimal approach to Bayesian assimilation of a linear measurement. For $M = 1$, the GMKF reduces to an Ensemble Kalman Filter (EnKF) in which only a single Gaussian is used to represent the prior (forecast) and posterior (analysis) densities. In the case of a mixture of Gaussians, the Kalman-analysis equations may be augmented with a weight-analysis equation to yield the proper application of Bayes' rule for each component in the mixture [84]. For $M > 1$, the GMKF may be viewed as a collection of Ensemble Kalman Filters operating in parallel [84]. Algorithm 1 contains the GMKF, for the case of constant noise covariances.

Algorithm 1 Gaussian Mixture Kalman Filter

```
Input: GMM of prior pdf
Output: GMM of analysis pdf
Parameters: $N$, MaxComplexity, and covariance matrices $Q$, $R$

Sample $N$ particles from the prior pdf.
Integrate the particles forward in time with process noise sampled from $\mathcal{N}(0, (t_k - t_{k-1})Q)$
// Fit a minimal GMM to the forecast ensemble
EM algorithm to fit GMM with 1 Gaussian. Evaluate the BIC.
for $m \leftarrow 2$ to MaxComplexity do
    EM algorithm to fit GMM with $m$ Gaussians. Evaluate the BIC.
    If BIC increases, select previous GMM, set $M = m - 1$, then break.
end for
// Assimilate measurements
Calculate the analysis weight for each Gaussian in GMM.
    $w_m^a = \frac{w_m^f \mathcal{N}(y; H\underline{x}_m^f, HP_m^f H^T + R)}{\sum_{q=1}^{M} \mathcal{N}(y; H\underline{x}_q^f, HP_q^f H^T + R)}.$
Calculate the Kalman gain, analysis mean, and analysis covariance for each Gaussian.
    $K_m = P_m^f H^T \left( HP_m^f H^T + R \right)^{-1},$
    $\underline{x}_m^a = \underline{x}_m^f + K_m(y - H\underline{x}_m^f),$
    $P_m^a = (I - K_m H)P_m^f.$
```

In practice, the model-size penalty term in (3.11) can be relaxed to allow for more complex models during the initial estimation cycles, reducing the tendency to place too much trust in the first measurements, causing the filter to follow noise in the data. Replace the $K \log N$ term in (3.11) with

$$K\left(1 - e^{t_k/\tau_{\text{relax}}}\right)\log N,$$

where τ_{relax} is a relaxation time constant. Note that either $t_k \to \infty$ or $\tau_{\text{relax}} = 0$ recovers (3.11).

The GMKF yields a GMM of the posterior pdf after assimilation of data. Two approaches to extracting estimates from the pdf are the use of a mode-finding algorithm such as [86] or taking the overall mean [86]

$$\underline{x} = \sum_{m=1}^{M} w_m \underline{x}_m \tag{3.13}$$

and covariance [86]

$$P = \sum_{m=1}^{M} w_m \left(P_m + (\underline{x}_m - \underline{x})(\underline{x}_m - \underline{x})^T\right) \tag{3.14}$$

of the mixture. The extraction of only a mean and a covariance from a possibly multimodal pdf does not fully utilize the pdf. Chapter 7 designs a path planner that uses the full posterior GMM. Section 7.2 compares the performance of this path planner to one that uses only the mean and covariance of the mixture.

3.2 Linear and empirical observability

In dynamical systems theory, observability describes the ability to infer the initial state of a system by observing the output over a specified time interval. The presence of a full-rank condition in the observability Gramian indicates that the state of a system can be inferred from observations of the output [60]. Consider system (3.1) without process noise or measurement noise, resulting in the deterministic linear system

$$\begin{aligned}\dot{x}(t) &= A(t)x(t)\\ y(t) &= C(t)x(t),\end{aligned} \tag{3.15}$$

with $x(t) \in \mathbb{R}^n$, $y(t) \in \mathbb{R}^m$, $A(t) \in \mathbb{R}^{n\times n}$, and $C(t) \in \mathbb{R}^{m\times n}$. For the time interval $[t_0, t_f]$, the linear observability Gramian is [87]

$$\mathcal{W}_{\mathrm{o}}(t_0, t_f) = \int_{t_0}^{t_f} \Phi(\tau, t_0)^T C^T(\tau) C(\tau) \Phi(\tau, t_0) d\tau, \tag{3.16}$$

where $\Phi(\tau, t_0)$ is the state transition matrix for the dynamics from time t_0 to τ. By uniqueness of the state solution to (3.15), the state transition matrix has the property that $\Phi(\tau, t_0)^{-1} = \Phi(t_0, \tau)$. Assessing the rank of $\mathcal{W}_{\mathrm{o}}(t_0, t_f)$ is a boolean test to determine whether the system is observable on the time interval $[t_0, t_f]$: if $\mathcal{W}_{\mathrm{o}}(t_0, t_f)$ is full rank, then the system is observable.

For a nonlinear system, the observability Gramian may not be easily formed through linearization about an equilibrium point [60, 88]. Consider nonlinear system (3.2) without noise, such that

$$\begin{aligned}\dot{x}(t) &= g(t, x(t))\\ y(t) &= h(t, x(t)),\end{aligned} \tag{3.17}$$

where g and h are nonlinear functions. The tangent-linear model for the dynamics (3.2) along a reference trajectory $x_r(t)$ with output $y_r(t)$ is given by the linear system

$$\begin{aligned} \frac{d}{dt}\left(\delta x(t)\right) &= \left.\frac{\partial g}{\partial x}\right|_{x_r(t)} \delta x(t) \\ \delta y(t) &= \left.\frac{\partial h}{\partial x}\right|_{x_r(t)} \delta x(t). \end{aligned} \tag{3.18}$$

For an initial condition x_0, the solution to (3.18) for $\delta x(t_0) = x(t_0) - x_r(t_0)$ yields the approximations $x_r(t) + \delta x(t) \approx x(t)$ and $y_r(t) + \delta y(t) \approx y(t)$. The local observability Gramian for the nonlinear system (3.17) is defined to be the linear observability Gramian (3.16) for the tangent-linear approximation (3.18) with $C(\tau) = \partial h/\partial x|_{x_r(\tau)}$ and $\Phi(\tau, t_0)$ as the state transition matrix for $\partial g/\partial x|_{x_r(\tau)}$ [60].

The empirical observability Gramian [60] is an approximation of the local observability Gramian (3.16) for the nonlinear system (3.17). Let $\phi(t, t_0, x(t_0))$ denote the state solution of (3.17) from $(t_0, x(t_0))$ at time t. Let $\epsilon > 0$ denote a perturbation magnitude, and let $\mathbf{e}_j$ represent the unit vector with one in the jth entry and zeros elsewhere. Through $2n$ simulations of the system output from closely perturbed initial conditions, the empirical observability Gramian for time interval $[t_0, t_f]$ may be constructed as

$$\mathcal{W}_{\mathrm{eo}}(t_0, t_f, x(t_0)) = \int_{t_0}^{t_f} \Psi_{\mathrm{e}}(\tau, t_0, x(t_0))^T \Psi_{\mathrm{e}}(\tau, t_0, x(t_0)) d\tau, \tag{3.19}$$

where the (i, j)th entry of the $n \times n$ matrix Ψ_{e} is

$$[\Psi_{\mathrm{e}}(\tau, t_0, x(t_0))]_{ij} = \frac{h_i(\tau, \phi(\tau, t_0, x(t_0) + \epsilon \mathbf{e}_j)) - h_i(\tau, \phi(\tau, t_0, x(t_0) - \epsilon \mathbf{e}_j))}{2\epsilon}. \tag{3.20}$$

Note that that Ψ_{e} is a central-difference approximation to $\partial h/\partial x(t_0)$ and, in the limit $\epsilon \to 0$, $\mathcal{W}_{\mathrm{eo}}$ converges to the local observability Gramian $\mathcal{W}_{\mathrm{o}}$ for (3.17) [60, 89].

Similar to the linear observability Gramian $\mathcal{W}_{\mathrm{o}}(t_0, t_f)$, the empirical observability Gramian $\mathcal{W}_{\mathrm{eo}}(t_0, t_f, x(t_0))$ must be full rank for the system (3.17) to be observable on $[t_0, t_f]$. The initial state $x(t_0)$ is also included in the arguments, because this assessment only applies for the initial condition used, in contrast to $\mathcal{W}_{\mathrm{o}}$. $\mathcal{W}_{\mathrm{eo}}$ has also been applied to systems similar to (3.17) that include a prescribed control signal $u(t)$, i.e., $\dot{x}(t) = g(t, x(t), u(t))$ [70, 89]. The control $u(\cdot)$ is a time-varying input signal, prescribed over $[t_0, t_f]$, so $\mathcal{W}_{\mathrm{eo}}$ should be denoted $\mathcal{W}_{\mathrm{eo}}(t_0, t_f, x_0, u_{[t_0,t_f]})$.[1]

If the system fails to satisfy the observability rank condition in any open subset of the state space, then the system is not locally observable [60]. If, however, the observability rank condition holds on $\mathcal{W}_{\mathrm{eo}}$, one may measure the degree of observability using the unobservability index ν of $\mathcal{W}_{\mathrm{eo}}$ defined by Krener and Ide [60] to be the reciprocal of the smallest eigenvalue $\lambda_{\min}$ of $\mathcal{W}_{\mathrm{eo}}$, i.e.,

$$\nu(\mathcal{W}_{\mathrm{eo}}) = \frac{1}{\lambda_{\min}(\mathcal{W}_{\mathrm{eo}})}. \tag{3.21}$$

The unobservability index quantifies how difficult it is to infer the initial condition $x(t_0)$ from the system output over $[t_0, t_f]$ [60].

---

[1] We omit some arguments of $\mathcal{W}_{\mathrm{eo}}(t_0, t_f, x(t_0), u_{[t_0,t_f]})$ and write instead $\mathcal{W}_{\mathrm{eo}}(t_0, t_f)$ or $\mathcal{W}_{\mathrm{eo}}$ if the meaning is clear from context.

Chapter 4

Application I: Output-feedback control for rheotaxis of a robotic fish

As an application of vehicle-scale flow estimation and control, this chapter presents the design and use of an artificial lateral-line system for a bioinspired robotic fish capable of autonomous flow-speed estimation and rheotaxis (the natural tendency of fish to orient upstream), using only flow-sensing information. This chapter addresses vehicle-scale flow estimation and control for a robotic fish through observability-based sensor placement, nonlinear/non-Gaussian estimation, and output-feedback control. This chapter contains the first application of observability-based sensor placement for flow-field estimation in an experiment, and it also makes contributions in bioinspired robotics by performing autonomous rheotaxis with symmetric and asymmetric sensor arrays.

This chapter describes the principled design and implementation of a dynamic control framework for rheotaxis of a bioinspired robotic fish that includes model-based estimation of flow-field parameters using two or more pressure sensors in an arbitrary arrangement. The technical approach employs a reduced-order fluid-mechanical model for flow past a streamlined body based on potential-flow theory (see Section 4.1). Sensor locations are selected to maximize empirical observability of the flow-field parameters (see Section 4.2). The recursive Bayesian filter from Section 3.1.1 estimates the flow speed and angle of attack, under a quasi-static assumption. The use of the estimated angle of attack with a proportional control law results in a dynamic rheotaxis controller (see Section 4.5).

The technical approach is justified by the following rationale: potential-flow theory produces a reduced-order model with few parameters that can be used within a real-time control loop; recursive Bayesian filtering can handle nonlinear observation operators (without linearization) and arbitrary non-Gaussian probability densities; and a simple proportional control law permits easier assessment of the filter performance in the control loop.

The experimental test bed consisted of a 185L flow tank, a two-degree-of-freedom mechanical gantry system, and a robotic fish endowed with commercially-available pressure sensors (see Section 4.3). To validate the potential-flow model, Section 4.4 compares it with computational fluid dynamic (CFD) simulations and laboratory experiments. Finally, Section 4.6 presents experimental test results from the rheotaxis controllers. The closed-loop demonstration of rheotaxis behavior is the first experimental implementation of model-based rheotaxis control of a robotic fish based on pressure-difference measurements without first training an empirical or fluid-mechanical model to match the flow-field conditions.

4.1 Pressure difference sensor model

This section presents a reduced-order fluid-mechanics model for flow past a fish body and a measurement equation to predict pressure differences between sensor locations in a bioinspired artificial lateral-line.

4.1.1 Flow past a streamlined body

An idealized model of fluid flow past a streamlined body enables estimates of flow parameters based on sensor measurements. Potential-flow theory and conformal mapping, making use of the Joukowski transformation [90, 91], provide the necessary tools. Let $\xi = Re^{i\theta} + \lambda$, where $\theta \in [0, 2\pi)$, be a disk of radius R centered at λ, and let $b = R - |\lambda|$ [90]. Using the complex plane to represent a two-dimensional domain, the transformation [90]

$$z = \xi + \frac{b^2}{\xi} \tag{4.1}$$

maps a disk into a symmetric streamlined body centered at the origin [90]. Let $U > 0$ be the free-stream flow speed and α be the angle of attack of the fish relative to the flow (when viewed from above). When transformation (4.1) is used in conjunction with the following complex potential [90, 91]

$$w(\xi) = U(\xi - \lambda)e^{-i\alpha} + \frac{R^2}{\xi - \lambda}Ue^{-i\alpha} + 2iRU\sin(\alpha)\log(\xi - \lambda), \tag{4.2}$$

it maps uniform flow past a cylindrical disk into uniform flow past a streamlined body [88, 90]. The first term in the complex potential (4.2) represents the uniform flow, the second term introduces the boundary condition, and the third term enforces the Kutta condition, which states that the rear stagnation point must occur at the trailing tip of the airfoil.

The conjugate flow $\bar{f}(z)$ around the body is [88, 90]

$$\begin{aligned}\bar{f}(z) &= \frac{\partial w}{\partial \xi}\left(\frac{\partial z}{\partial \xi}\right)^{-1} \\ &= \left(Ue^{-i\alpha} - \frac{R^2}{(\xi(z)-\lambda)^2}Ue^{i\alpha} + \frac{2iRU\sin(\alpha)}{(\xi(z)-\lambda)}\right)\left(1 - \frac{b^2}{(\xi(z))^2}\right)^{-1}, \end{aligned} \tag{4.3}$$

where $\xi(z)$ is the dual-valued inverse mapping of (4.1) with values selected to lie outside of the fish body [88, 90], i.e.,

$$\xi(z) = \begin{cases} \frac{1}{2}\left(z + \sqrt{z^2 - 4b^2}\right) & \arg(z) \in \left(-\frac{\pi}{2}, \frac{\pi}{2}\right] \\ \frac{1}{2}\left(z - \sqrt{z^2 - 4b^2}\right) & \arg(z) \in \left(\frac{\pi}{2}, \frac{3\pi}{2}\right]. \end{cases} \tag{4.4}$$

The real and imaginary parts of $f(z)$ give the components of the flow field. Note that the flow is evaluated at sensor locations and is parameterized by the free-stream flow speed U and angle of attack α.

4.1.2 Pressure-difference measurement equation

Consider multiple pressure sensors distributed around the body of a robotic fish enclosed within canals as shown in Figure 4.3, with p_j denoting the pressure at sensor

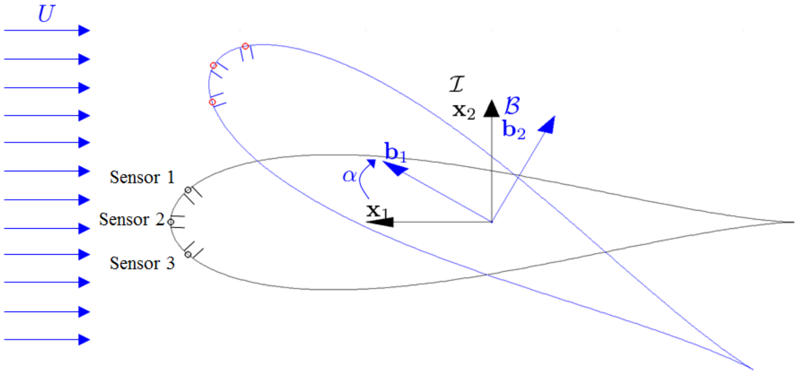

Figure 4.1: Relevant reference frames and flow-field parameters describing a one-degree-of-freedom robotic fish (top view).

location j. A model of the pressure values predicted by the potential-flow model (4.3) is obtained from Bernoulli's principle for inviscid, incompressible flow along a streamline [92], i.e.,

$$\frac{v^2}{2} + gh + \frac{p}{\rho} = C, \tag{4.5}$$

where v is the local flow speed, g is the acceleration of gravity, h is the elevation, p is the static pressure, ρ is the fluid density, and C is a constant describing the total specific energy of a fluid parcel moving along the streamline. Applying (4.5) to two equal-elevation locations along a streamline, one of which is a stagnation point, results in the following expression for pressure p in terms of the streamline's stagnation pressure p_s [92]:

$$\frac{v_1^2}{2} + \frac{p_1}{\rho} = \frac{p_s}{\rho},$$

which implies (after dropping the subscript)

$$p = p_s - \rho \frac{v^2}{2}.$$

Figure 4.2(a) shows the pressure p at sensor 1 for various flow-field parameters with stagnation pressure $p_s = 100$ Pa.

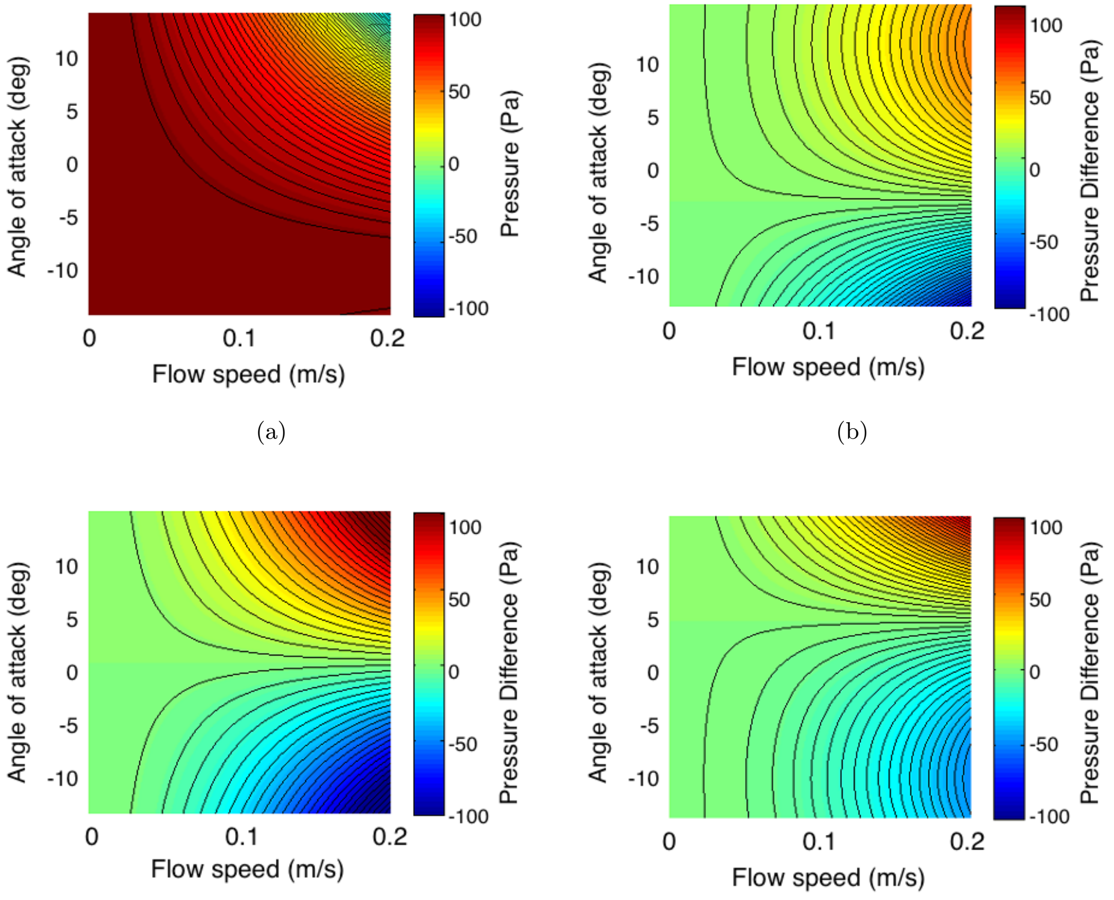

(a)

(b)

(c)

(d)

Figure 4.2: (a) Fluid pressure at the sensor location; (b) pressure difference between p_1, p_2; (c) p_1, p_3; and (d) p_2, p_3 sensors locations

For an unknown angle of attack, the stagnation pressure p_s is not known. However, the difference between two pressure sensors is

$$\Delta p_{12} = p_2 - p_1 = \frac{\rho}{2}\left(v_1^2 - v_2^2\right).$$

Hence, a measurement equation based on the pressure difference offers the advantage that the stagnation pressure, an identifying characteristic of the flow condition, does not need to be known *a priori*. The measurement function for the case of three sensors is a vector collecting individual pressure differences $\Delta p = [\Delta p_{12}, \Delta p_{13}, \Delta p_{23}]$, where Δp_{jk} indicates the pressure difference from sensor j to sensor k. Figures 4.2(b), 4.2(c), and 4.2(d) illustrate pressure difference values between sensor pairs available in Figure 4.1 for various flow conditions. The maximum value of $U = 0.2$ m/s corresponds to a flow speed of 2 body lengths per second for a 10 cm fish. These plots show angles of attack $\alpha \in [-15°, 15°]$, since the flow model is accurate only for small angles due to the stall condition that arises in the study of airfoils [88, 91]. Nonetheless, the experiments evaluate the model in the range $\alpha \in [-35°, 35°]$.

Assume that the pressure measurements contain additive Gaussian white noise, i.e., the jth sensor measurement is

$$\tilde{p}_j = p_j + \eta_j, \tag{4.6}$$

where η_j has a zero-mean Gaussian distribution with σ_j^2 variance, $\mathcal{N}(0, \sigma_j^2)$. (Note, the difference between sensor signals produce another random variable, $\eta_k - \eta_j$, which has distribution $\mathcal{N}(0, \sigma_j^2 + \sigma_k^2)$). Let $\Omega = [U, \alpha]^T$. The measurement equation, after subsititution of the flow model (4.3) and inclusion of the additive measurement noise model (4.6), becomes

$$\Delta\tilde{p}_{jk}(z_j, z_k; \Omega) = \frac{\rho}{2}\left(|\bar{f}(z_j, \Omega)|^2 - |\bar{f}(z_k, \Omega)|^2\right) + \eta_k - \eta_j. \tag{4.7}$$

The pressure difference in (4.7) may be based on sensors arbitrarily distributed around the fish body; equation (4.7) does not require that the pressure sensors be close together. Thus, (4.7) is a bioinspired, but not biomimetic, approach to pressure sensing, since pressure differences measured by canal neuromasts in the lateral-line result from the fluid pressure at neighboring pore locations [18]. Equation (4.7) can be used to estimate Ω from pressure measurements. However, Figure 4.2(c) shows that U is unobservable at zero angle of attack for the symmetric p_1, p_3 sensor pair, because all flow speeds give $\Delta p_{13} = 0$. Figures 4.2(b) and 4.2(d) show how this unobservable region shifts in parameter space for asymmetric sensor pairs. Similarly, α is unobservable if U is zero. Observability is also lost if the pressure difference is smaller than the noise level of the sensors.

4.2 Optimizing sensor placement for flow observability

This section describes optimal pressure sensor placement, based on maximizing the empirical observability of the unknown flow parameters, similar to [88]. Numerical calculation of the empirical observability Gramian (3.19) for a sensor pair at a constant angle of attack reveals that the joint state (U, α) is not locally observable, regardless of the pair placement, because $\mathcal{W}_{eo} \in \mathbb{R}^{2\times 2}$ has rank one. However, observability may be restored if one combines measurements from the same sensor pair at different angles (i.e., if the fish robot is permitted to move). Further, observability can be restored for either the U or α parameter-estimation problem if an estimate of the accompanying state component is known (e.g., via another sensing modality). Figure 4.3 shows the results for optimizing placement of a pair of pressure sensors to observe a fixed angle of attack for several discrete angles. Although the flow speed must be known, the results are independent of its actual value [88].

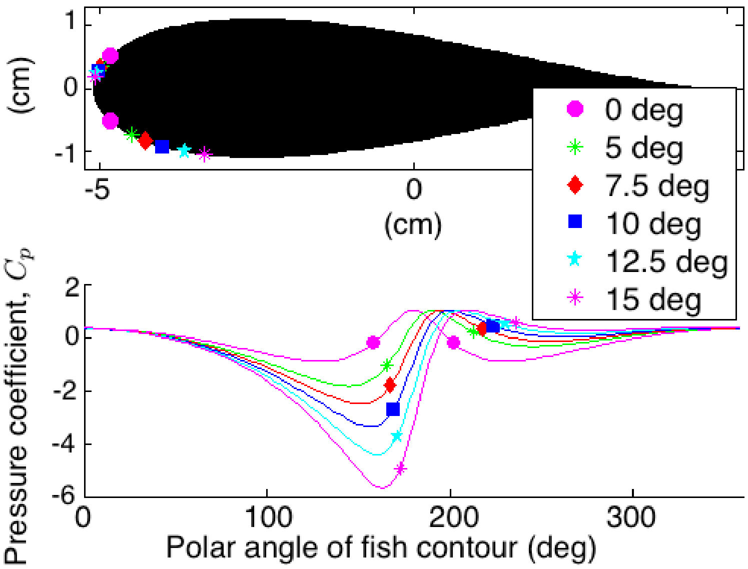

Figure 4.3: Optimal placement locations for a pair of pressure sensors based on observability of several discrete angles of attack.

Figure 4.3 plots the nondimensional coefficient of pressure [90] $C_p = 1 - |f|^2/U^2$ versus polar angle around the fish body, starting from 0° at the tail, wrapping counterclockwise to 180° at the nose, and returning to 360° at the tail. Whenever the flow speed on the surface of the fish body is zero, the flow is stagnant and the pressure is maximum, so $C_p = 1$. Note that the sensor pairs always straddle the stagnation point, as seen in the lower subplot. Further, for increasing angles of attack, one of the sensor locations approaches the nose of the fish. Performing this analysis for angles in the range of $\alpha = [-15^\circ, 15^\circ]$ in increments of 2.5° and summing the observability Gramian values over all angles, the optimal sensor pair for zero angle of attack is also the optimal pair for observing arbitrary angles of attack.

Optimization of the nonlinear observability in the three-sensor case produces an asymmetric result, with a corresponding mirror configuration (mirrored about the real axis) that is also optimal. The experiments of this chapter use three sensors in a symmetric layout; two pressure sensors are at the optimal two-sensors locations and a third sensor is at the nose of the fish. The joint state (U, α) is observable with this three-sensor configuration, and its symmetry allows for proper flow-field alignment. Furthermore, as shown experimentally in Section 4.6, ignoring the signal from the nose sensor, leaves a two sensor configuration that is optimal for observing angle of attack.

4.3 Robotic test bed for flow sensing and control

This section describes the laboratory test bed constructed for experimental validation of the flow-sensing and control framework. Figure 4.4 shows the laboratory test bed, which consisted of a 185 L flowtank (Loligo Systems, SW10275 modified) and a two-degree-of-freedom custom robot equipped with commercially available pressure sensors (Millar Instruments, Mikro-Tip Catheter Pressure Transducers, model SPR-524). The flow tank had a flow straightener and a 25 x 25 x 87.5 cm enclosed test section. A 5 x 22 cm slot

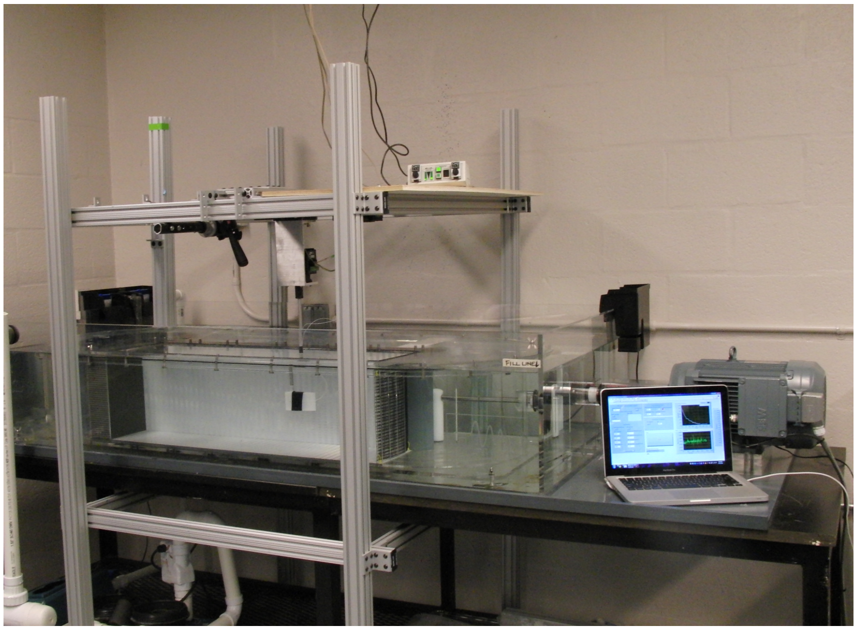

Figure 4.4: The laboratory test bed consisted of a 185 L flowtank and a two-degree-of-freedom underwater robot equipped with commercially available pressure sensors. The motors that regulate the robot position and orientation were controlled by a laptop computer.

in the top of the test section provided access for the robotic control arm. Calibration of the flow tank was accomplished using a Hach FH950 portable flow meter. A mechanical gantry system provided overhead control of the robot's orientation and cross-stream position (although only orientation control was used in the rheotaxis experiment). The gantry was elevated by a custom support fixture (materials from 80/20, Inc.) and consisted of an LS-100-18-H linear lead screw table (Anaheim Automation), coupled to a secondary stepper motor for rotary motion. Both stepper motors were STM23Q-XAE integrated stepper drives (Applied Motion Products), which take commands from LabVIEW via an RS-232 serial connection. The drives contained built-in motion controllers that accept high-level text commands, most notably feed-to-length and jog commands for control of motor position or angular velocity. The stepper motors also contained integrated encoders that were queried directly from LabVIEW. Each robotic fish was constructed from a 3D-printed airfoil shape when viewed from above, as shown in Figure 4.5. Choosing $R = 2.9$ cm and $\lambda = -0.5$ cm yields a 9.9 cm by 2.2 cm fish cross-section that approximately

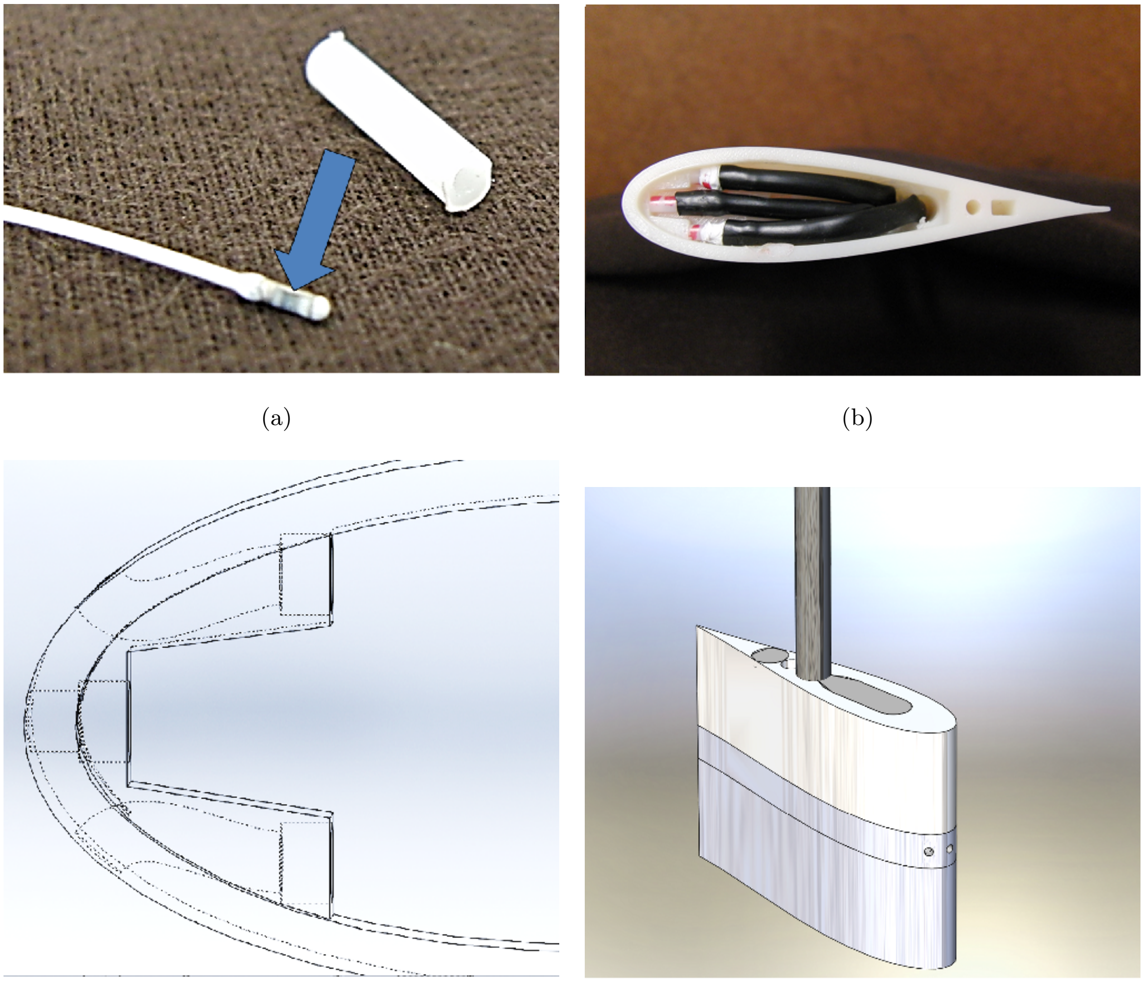

(a) (b)

(c) (d)

Figure 4.5: Images of the robotic fish used in the experiments: (a) Mikro-Tip pressure sensor (arrow points to rectangular sensing area on side of the device tip) and Delrin isolation tube; (b) sensors installed in fish within Delrin tubes and PTFE sleeving; (c) internal canal features of the robotic fish; (d) CAD image of assembled robot.

resembles the length and width characteristics of a Mottled sculpin (*Cottus baridi*) [93, 94], a fish previously studied for rheotactic response [95]. The height of the robotic fish (6 cm) reduced the three-dimensional effects of the flow near sensor locations. The fish was printed on a uPrint SEPlus printer (Stratasys Ltd) in three pieces with a hollow inner pocket and port holes with small canals for the sensors. Figure 4.1 shows the locations of the three pressure sensors used in these experiments. Sensor placement was based on the observability analysis described in Section 4.2. The sensors were piezoresistive pressure transducers with a straight end (size 3.5F), containing a small rectangular sensing region on the side of the device tip, as shown in Figure 4.5(a). The sensors connected to two PCU-2000 Pressure Control Units (Millar Instruments) and were embedded in canals to shield from direct flow impingement. The sensors read the static pressure, which enabled analysis using the potential-flow model as described in Section 4.1. The sensors were secured in small Delrin tubes within the robotic fish using Teflon tape (see Figures 4.5(a) and 4.5(b)). Calibration of each sensor was performed by submersion in a known hydrostatic pressure; all sensors in this work had calibration constants within 1% of the manufacturer-supplied value of 13.30 kPa/V. Soaking the sensors in water for 30 minutes prior to use reduced sensor drift. Further, pressure data was collected in still water; after each run, we verified that sensor drift had not exceeded 2%, similar to Venturelli *et al.* [13]. A NI-USB-6225 data acquisition board, with a BNC-2115 connector block (National Instruments) provided the link between the pressure sensors and the LabVIEW software interface. Sampling occurred at 1000 Hz (within the frequency response limits of the pressure sensors). However, using the mean of 200 samples as an individual measurement increased the signal-to-noise ratio; thus, the effective sampling rate for data collection was 5 Hz. The control loop frequency for all rheotaxis experiments was set to 1 Hz to account for differences in computation time between the control schemes.

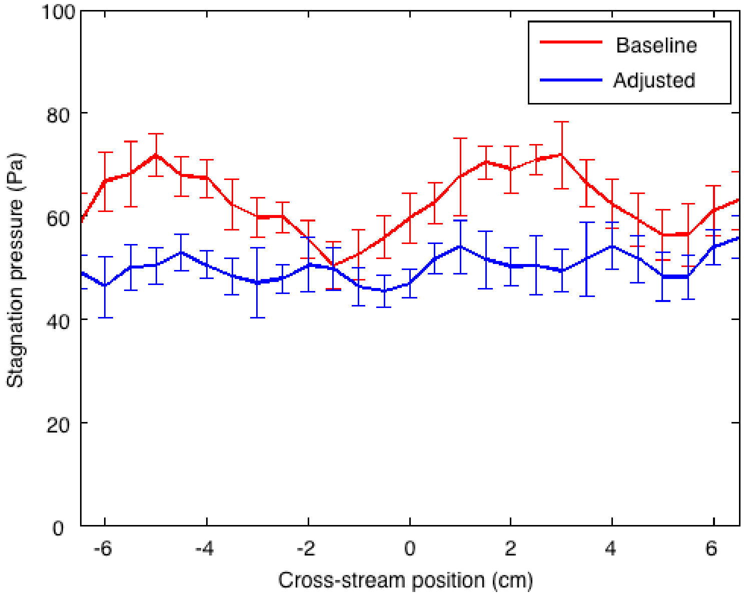

Figure 4.6: Cross-stream pressure survey (zero is channel center) of the Loligo 185L flow-tank, before and after modification. $U = 0.26$ m/s (both curves).

Figure 4.6 shows a time-averaged cross-stream pressure survey of the flow tank. It reveals periodic structures approximately 6 cm wide that align with the guide vanes located upstream of the flow straightener. The fluid-mechanical model presented in Section 4.1 does not account for such variations. We reduced these variations by including additional flow straightening structures. Adding two pieces of 3.5 cm wide, 3 mm pore size honeycomb (Nomex) and an additional flow straightener (Loligo Systems) with 7 cm spacing between each component reduced the cross-stream pressure variations as shown in the Figure 4.6. Note that, although the standard deviation (error bars) may increase at a given location, the overall maximum, minimum, and average standard deviations were reduced. Figure 4.7(b) illustrates the arrangement of the additional honeycomb in the swim channel.

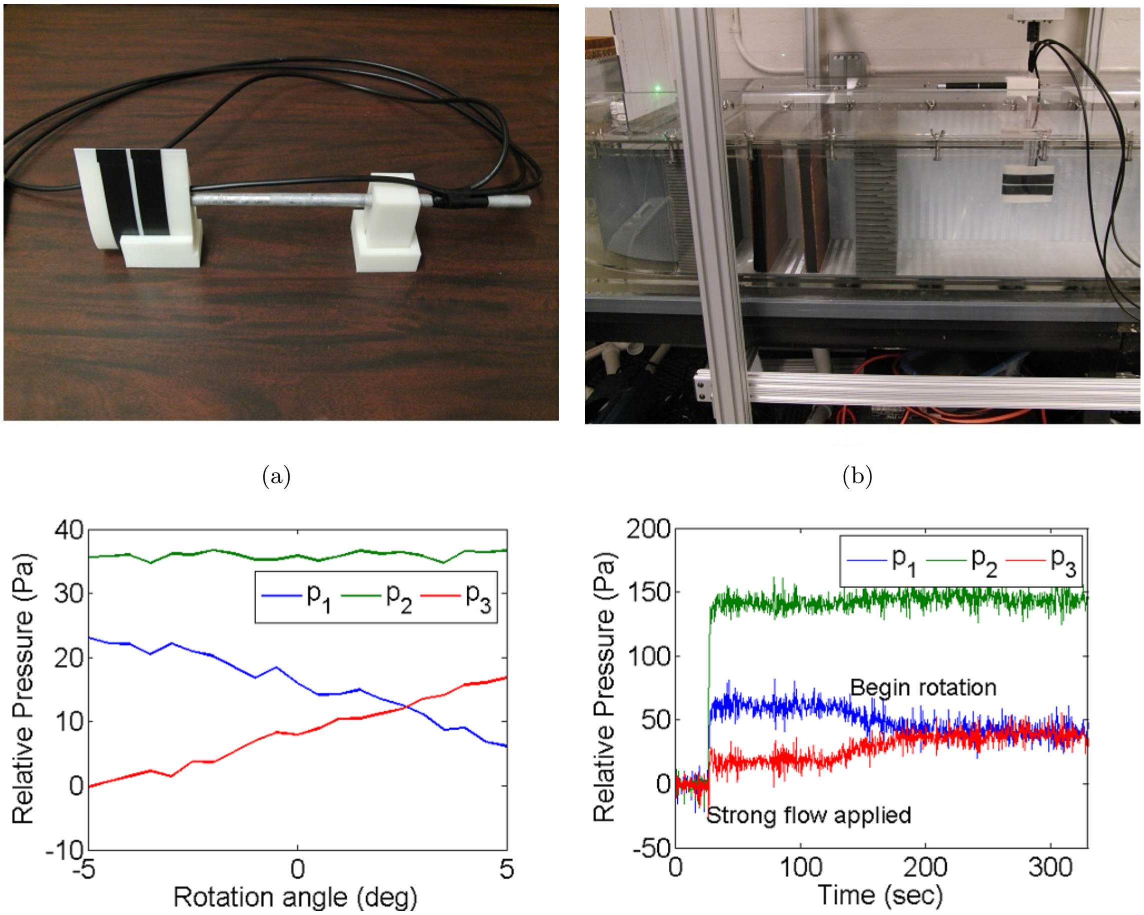

(a) (b)

(c) (d)

Figure 4.7: Initial fish alignment. (a) Custom 3D-printed tools for aligning the fish body and holder for a laser pointer; (b) Alignment of the robotic fish using a laser; (c) Time-averaged relative pressures ($U = 0.22$ m/s) during a rotary scan after laser alignment; (d) Final alignment: equalizing p_1, p_3 pressures.

Since the encoder in the rotary gantry motor provides only a relative rotational measurement, an initial alignment procedure was necessary. The fish body was first aligned to a holder for a laser pointer using 3D-printed tooling (see Figure 4.7(a)); next, the fish was rotated until the laser illuminated markings corresponding to the center of the test section (see Figure 4.7(b)). After this procedure, we performed a rotary sweep (±5°) collecting time-averaged pressure measurements. Figure 4.7(c) illustrates the time-averaged pressure measurements collected during a ±5° rotary sweep of the fish. Note that the p_2 signal is relatively flat and the p_1, p_3 signals cross at a location of equal pressure. Due to the symmetric placement of the sensors, the crossing of the signals at a location away from the zero orientation indicates an error that can be attributed to the manufacturing tolerances of the flow tank and the 3D-printed fish, uncertainties in the laser alignment process, and variations in the pressure field. To define the upstream zero orientation (zero angle of attack), we rotated the robotic fish in a strong flow ($U = 0.47$ m/s) until the p_1, p_3 pressures were equal. Figure 4.7(d) shows the pressure signals during this process. We note that the final alignment did not visually differ from the laser aligned condition, i.e., it was accurate to within 3° of the upstream direction.

4.4 Potential-flow model evaluation

This section presents an evaluation of the potential-flow model using computational fluid dynamics (CFD) simulations and the experimental test bed. To validate the potential-flow model from Section 4.1, we compared it with simulations from a commercially available CFD solver (COMSOL) and experimental sensor data. The COMSOL CFD simulations solved the Reynolds Averaged Navier Stokes equations with a Spalart-Allmaras turbulence model [96]. Figures 4.8(a), 4.8(c), and 4.8(e) show the pressure difference Δp_{13} for constant angles of attack. Figures 4.8(b), 4.8(d), and 4.8(f) show the pressure difference Δp_{13} for constant flow speeds. For low flow speeds and angles of attack, the potential-flow model accurately represents the physical phenomenon captured in the high-fidelity CFD model, with decreasing accuracy at higher speeds and angles. (We note that a small difference exists in the inlet boundary condition for the CFD simulations and experiments; the CFD inlet boundary condition is the free stream flow speed measured by the flow probe at the location occupied by the fish during testing, not the true flow speed of the inlet to the test section).

Discrepancies with experimental data are likely due to sensor noise, angular alignment uncertainty, disturbances in the free-stream flow, cross-stream flow non-uniformities, and unmodelled viscous effects. Figure 4.9 shows the onset of flow separation from the fish body, a viscous effect captured by the CFD simulations. When flow separation occurs, the streamlines of the flow no longer conform to the shape of the streamlined body, due to a region of backflow or recirculating flow on the upper surface of the fish, often leading to an unsteady, turbulent wake [90]. The potential-flow pressure-difference model of Section 4.1 assumes that the flow is steady, irrotational, inviscid, and conforms to the body of the fish. Further, the flow conditions considered here (0.05 m/s to 0.20 m/s) have free-stream Reynolds numbers that range from $12,500$ to $50,000$ in the test section. These values exceed the $2,300$ demarcation value for transition from laminar to turbulent flow that is often used for internal flows [92], clearly violating the laminar flow assumption of the potential-flow model. Nonetheless, the potential-flow model still proves useful in a control loop, because it captures the general shape of the pertinent physical relationships. Note that the accuracy of the potential-flow model increases as the angle of attack approaches zero. The potential-flow model is also a reduced-order model, offering the possibility of real-time implementation.

4.5 Estimation and control framework for rheotaxis

This section describes an approximate recursive Bayesian filter for estimating flow-field parameters from pressure measurements and a dynamic control framework for rheotaxis.

4.5.1 Recursive Bayesian filtering with pressure differences

We adapt the recursive Bayesian filter from Section 3.1.1 to the application of rheotaxis for robotic fish. In this application, the flow-field parameter vector Ω represents the system state. Under a quasi-static assumption, α is a flow-field parameter. However, α may equally represent the state of the robot turning in the flow. The output $y(t_k)$ at measurement time t_k is the vector of pressure differences corrupted by noise, $\Delta\tilde{p}$. The assumption of additive Gaussian measurement noise results in a Gaussian likelihood function

$$\pi(\Delta\tilde{p}|z,\Omega) \propto \exp\left(-\frac{1}{2}(\Delta\tilde{p}-\Delta p(z,\Omega))^T R^{-1}(\Delta\tilde{p}-\Delta p(z,\Omega))\right), \tag{4.8}$$

where R is the measurement covariance matrix. For the three-sensor case,

$$R = \mathrm{diag}\left(\sigma_1^2+\sigma_2^2, \sigma_1^2+\sigma_3^2, \sigma_2^2+\sigma_3^2\right),$$

otherwise $R = \left(\sigma_j^2 + \sigma_k^2\right)$ for a single p_j, p_k sensor pair. (The variances are chosen by collecting data from the pressure sensors and analyzing the noise statistics. Since the noise in the sensor measurements increases with free-stream flow speed, we choose the values based on measurements at the maximum relevant flow speed.) Note that we include the vector of sensor locations z in (4.8) for clarity. However, for a given robot geometry, z is a deterministic function of α and inclusion is not necessary.

Pressure sensors provide a sequence of measurements represented by $D_k \triangleq \{\Delta\tilde{p}(t_0), \ldots, \Delta\tilde{p}(t_k)\}$ for collection times $\{t_0, t_1, \ldots, t_k\}$. The posterior probability density from the previous t_{k-1} assimilation time is used as the prior density for assimilation at time t_k, yielding

$$\pi(\Omega(t_k)|D_k) \propto \pi\left(\Delta\tilde{p}(t_k)|\Omega(t_k)\right)\pi\left(\Omega(t_{k-1})|D_{k-1}\right). \tag{4.9}$$

4.5.2 Dynamic control design

We now present a model-based dynamic controller for rheotaxis for which a block diagram is shown in Figure 4.10. The kinematics of the robot turning at a commanded angular rate u are

$$\dot{\alpha} = u, \tag{4.10}$$

where u is the control input. The Bayesian filter produces estimates of $\hat{\alpha}$ and $\hat{U}$ as the robot moves. The estimate $\hat{\Omega}(t_k)$ is the maximum *a posteriori* estimate of (4.9), i.e.,

$$\hat{\Omega}(t_k) \triangleq \underset{\Omega}{\operatorname{argmax}}\, \pi\left(\Omega(t_k)|D_k\right). \tag{4.11}$$

The controller calculates the control input with the proportional control law [88]

$$u = -K_1 \hat{\alpha}. \tag{4.12}$$

Note that if $\hat{\alpha} = 0$, then the closed-loop system $\dot{\alpha} = -K_1 \hat{\alpha}$ is in equilibrium. Moreover, if the filter produces $\hat{\alpha}$ estimates that at least have the correct sign as the true orientation, then the robot will drive toward $\alpha = 0$, which is the direction of increasing model validity. We have shown previously that, if the estimation error is bounded, then the angle of attack error is uniformly, ultimately bounded, with ultimate bound inversely proportional to the control gain K [88]; this result is illustrated by the experimental results of Section 4.6. Since the Bayesian filter is applied in real-time, it is necessary to account for the fish motion during the estimation step. Let (3.8) serve as the evolution equation with process uncertainty so that the prior pdf for the next Bayesian assimilation cycle represents the best estimate of the system state. We choose $\pi\left(\Omega(t_{k+1})|\Omega(t_k)\right)$ to be a Gaussian transition density [88]

$$\pi\left(\Omega(t_{k+1})|\Omega(t_k)\right) = \mathcal{N}(\Psi, Q), \tag{4.13}$$

where $\Psi \triangleq [0, \Delta t \dot{\alpha}(t)]^T$, and Q is the process noise covariance matrix, which is tuned to maximize filter performance. Tuning may be performed by commanding known trajectories of the robotic fish while estimating the state of the system, increasing the process-noise variance for each run (from a small initial value) until desired estimation tracking is obtained.

4.6 Experimental demonstration of rheotaxis control

This section presents estimation results for angle of attack and flow speed using the potential-flow model and a Bayesian filter, assuming the true values are constant. It also includes results of a rheotaxis controller based on pressure-difference feedback control, and it compares these results to the performance of dynamic rheotaxis control based on recursive Bayesian filtering.

4.6.1 Constant angle-of-attack and flow-speed estimation

Results of Bayesian estimation for constant angle-of-attack and flow-speed experiments are shown in Figure 4.11. Figures 4.11(a) and 4.11(b) present the marginal pdf's and estimated parameter values (based on the mode of the joint posterior density) for an angle of attack of 4° and a fixed flow speed of 0.10 m/s. Figure 4.11(c) and 4.11(d) illustrate the case of an angle of attack of 14° and a fixed flow speed of 0.20 m/s. These two cases span a large portion of the desired operational range and are representative of the results in most configurations. In both cases, the Bayesian estimator provides a reasonable flow-speed estimate within only a few seconds. The flow-speed estimates are accurate thoroughout the remainder of the run. However, in all cases, the estimator systematically underestimates the angle of attack. Nonetheless, the angle-of-attack estimate always tended towards a steady value with the correct sign, similar to Figures 4.11(b) and 4.11(d). We attribute the filter's inability to estimate angle of attack to model errors. Note in the model comparison results of Figure 4.8 that the model fit to experimental results for flow speed at a constant angle of attack is superior to the model fit for angle of attack.

4.6.2 Rheotaxis via pressure-difference feedback control

We first implemented a feedback control for rheotaxis based directly on the Δp_{13} pressure difference from the p_1, p_3 pressure sensors located on opposing sides of the fish robot (see Figure 4.1). The control input u was calculated according to the proportional control law

$$u = -K_2 \Delta\tilde{p}_{13}, \tag{4.14}$$

where K_2 is a proportional gain. Figure 4.12 shows the results of the rheotaxis experiment using (4.14) for two separate flow speeds. Note that convergence to the desired orientation is not monotonic. Further, 20 to 40 seconds elapse before rheotaxis is achieved, and the convergence rate and variations in orientation are dependent on flow speed. It is evident that the pressure-difference signal is jagged and noisy. Although the proportional control law (4.14) is sufficient to accomplish rheotaxis, it lacks memory of past measurements, causing sensitivity to sensor noise, and also requires sensors to be arranged symmetrically on the fish.

4.6.3 Rheotaxis via dynamic control with Bayesian filtering

Figure 4.13 presents results from rheotaxis experiments using the estimation and control framework and the $[\Delta p_{12}, \Delta p_{13}, \Delta p_{23}]^T$ measurement signals from the sensor arrangement in Figure 4.1. Figures 4.13(a), 4.13(c), and 4.13(e) show an experiment with a flow speed of 0.12 m/s and an initial angle of attack of 30°. Figures 4.13(b), 4.13(d), and 4.13(f) present another experiment with a flow speed of 0.07 m/s and an initial angle of attack of $-30°$. Although the Bayesian filter typically underestimates the angle of attack as shown in the constant angle-of-attack estimation, in both cases the control loop drives the robotic fish to the correct upstream direction, because the estimation error vanishes at zero angle of attack. These results show that a dynamic controller based on the potential-flow model achieves rheotaxis from an uncertain initial orientation outside the accurate domain of the potential-flow model.

Although the Bayesian estimation approach increases the computational work required, one of its benefits over simple pressure difference control is reduced long-term sensitivity to sensor noise. Figure 4.13 shows the estimator transient response is short ($<$ 20 s). Although the estimator exhibits sensitivity to noise in the transient period, it maintains its final estimates without large excursions due to noisy data. This benefit is due in part to the filter's ability to assimilate Δp measurements from multiple sensor pairs. The 0.07 m/s case was selected for direct comparison to the performance of the simple pressure difference controller under the same conditons. The low flow-speed condition is challenging for both controllers due to the low pressure signal-to-noise ratio. The time history of the Bayesian controller results in a steady, long-term orientation of the robot. Note in Figure 4.13(b) the estimator initially generates an angle-of-attack estimate with the wrong sign, causing the robot to turn in the wrong direction, before correcting the filter's estimate and driving to zero angle of attack.

One advantage of the simple pressure difference approach is that only two sensors are needed. The results shown thus far for the Bayesian dynamic controller rely on three sensors. To allow further direct comparison to the simple pressure difference approach, we look at the case of only utilizing the p_1, p_3 sensors in the dynamic controller. Note that this case represents an example of how the dynamic rheotaxis controller performs if the p_2 nose sensor fails. Figures 4.14(a), 4.14(c), and 4.14(e) present the results of a rheotaxis experiment using the Δp_{13} signal. The robotic fish achieves rheotaxis with a long-term orientation that is robust to noise. Figures 4.14(b), 4.14(d), and 4.14(f) illustrate the performance of the Bayesian rheotaxis controller in the case of p_1 sensor failure (a sensor on one side of the fish). The robotic fish is able to achieve rheotaxis using only the Δp_{23} signal. This result is significant because the p_2, p_3 sensor pair is an asymmetric sensor configuration. We note that both cases of the two-sensor configurations shown here provide accurate estimates of the free-stream flow speed, which was accomplished by modifying the filter process noise variance.

As noted in Section 4.2, the joint state (U, α) is not observable for a single sensor pair at a constant angle of attack, but observability can be restored if the robot is allowed to move and measurements are integrated in time. Thus, initial conditions with small angle of attack resulted in poor estimator performance. Comparing the two-sensor experiments to the three-sensor experiments reveals that properly placed additional sensors can increase the observability of the flow field, improving robustness in the estimates and overall estimator performance.

Although empirical methods can be used for rheotaxis behavior in a robotic fish, the principled approach outlined here has the following additional advantages: it provides robust rheotaxis performance in the presence of noise; it provides estimates of both the angle of attack and flow speed, which can be used for more complex navigational tasks; it provides extensibility to more sophisticated fluid-mechanical models; it generalizes to asymmetric/arbitrary sensor configurations, requiring only evaluation of the flow model at these sensor locations; and it provides a framework in which information can easily be fused from multiple sensors and multiple sensory modalities.

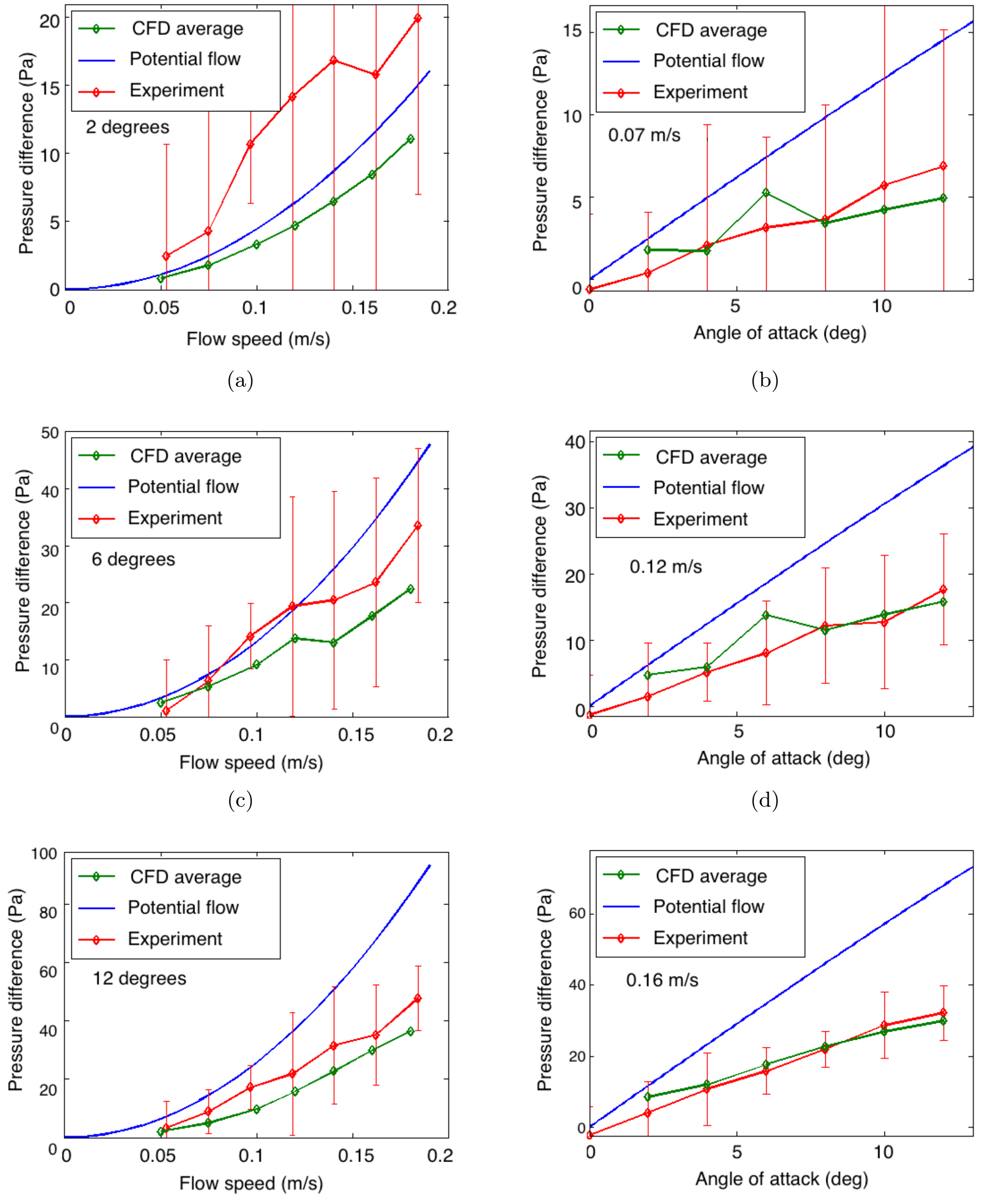

(a) (b)

(c) (d)

(e) (f)

Figure 4.8: Evaluation of the potential-flow model using CFD and experiments. (a), (c), and (e) Comparisons for constant angle of attack; (b), (d), and (f) comparisons for constant flow speed. Error bars represent the standard deviation of the experimental data.

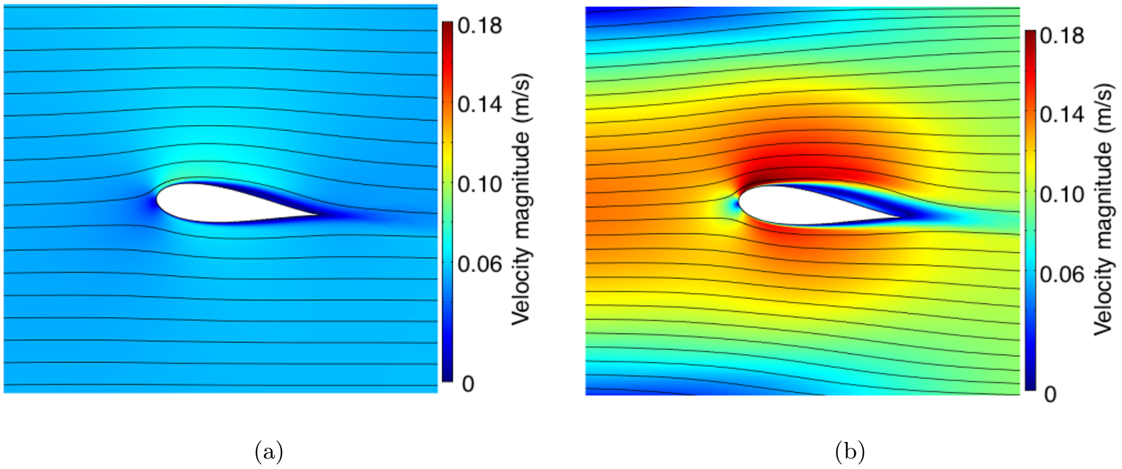

(a) (b)

Figure 4.9: CFD simulations showing the onset of flow separation. (a) 6° angle of attack, $U = 0.05$ m/s; (b) 6° angle of attack, $U = 0.14$ m/s

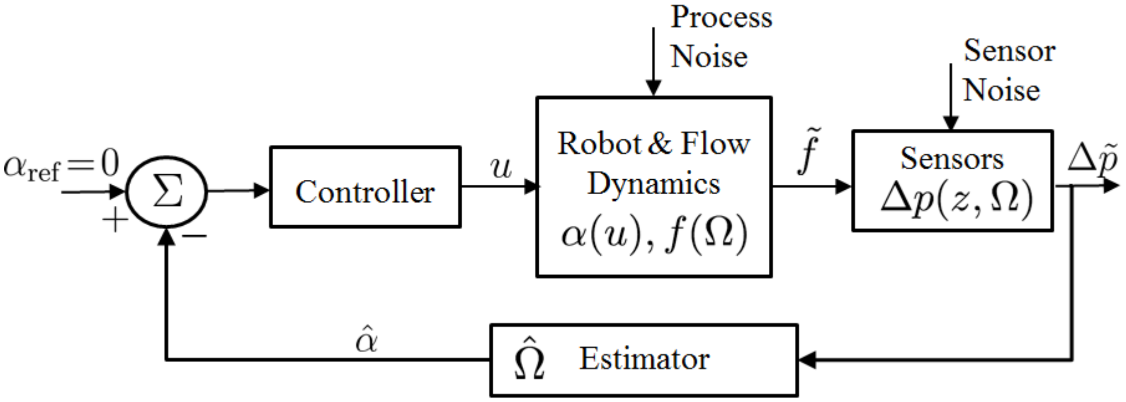

Figure 4.10: Flow-sensing, estimation and control framework for rheotaxis.

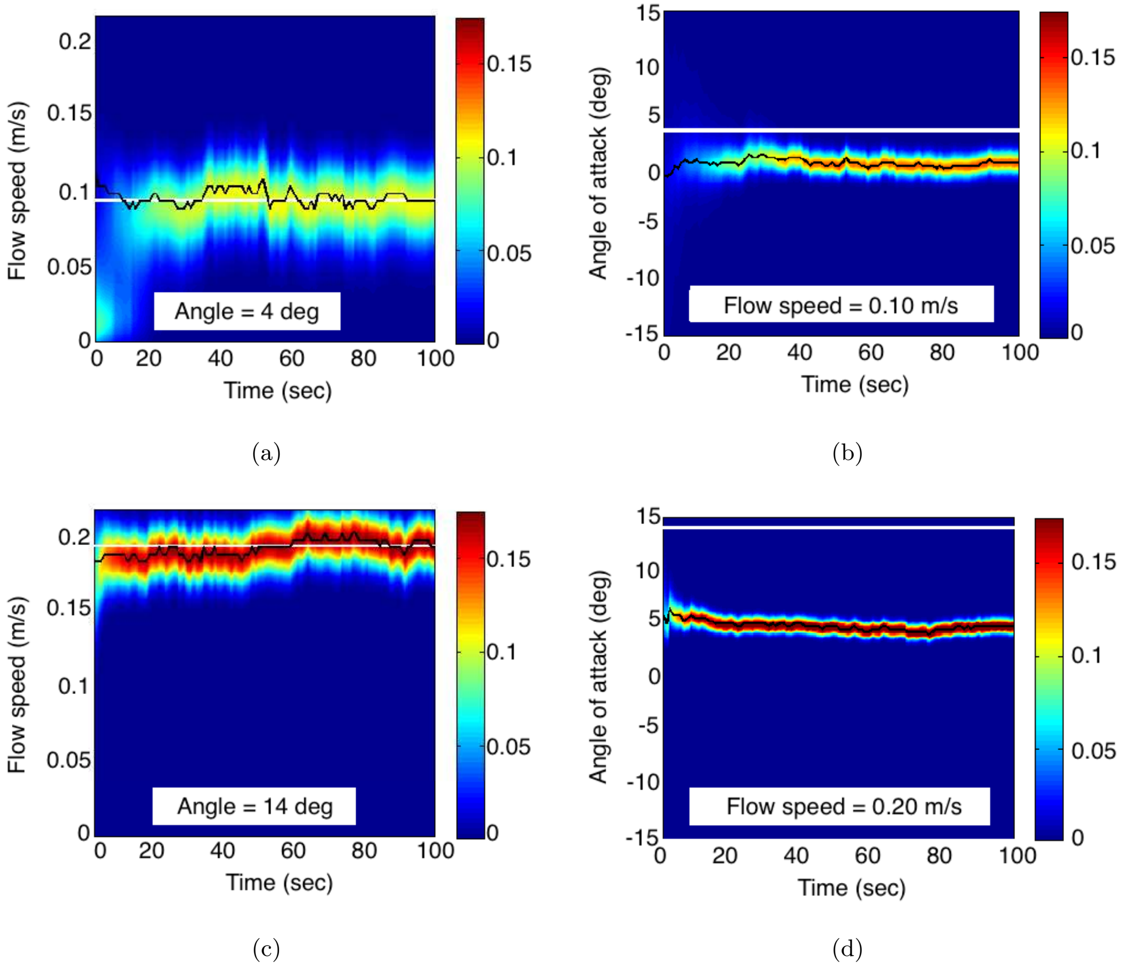

Figure 4.11: Estimation results for fixed angle of attack and flow speed. Contour plots show the marginal pdfs at each instant in time. The estimate (mode) is shown in black, and the white lines indicate the ground truth values.

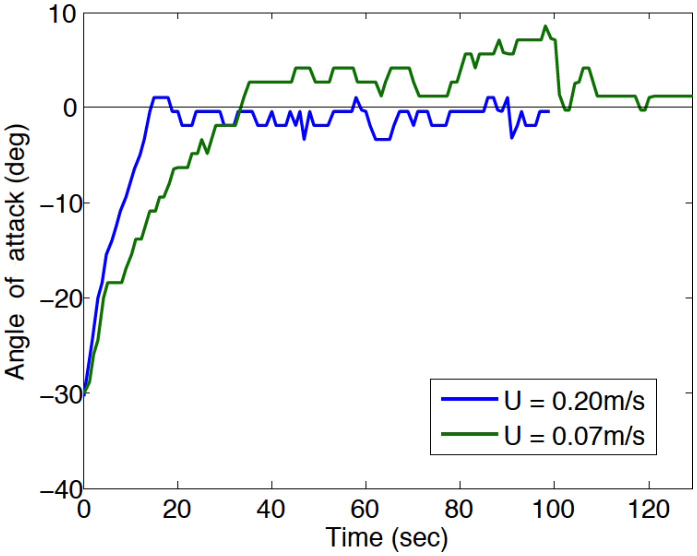

Figure 4.12: Results of robotic rheotaxis using a pressure-difference feedback control.

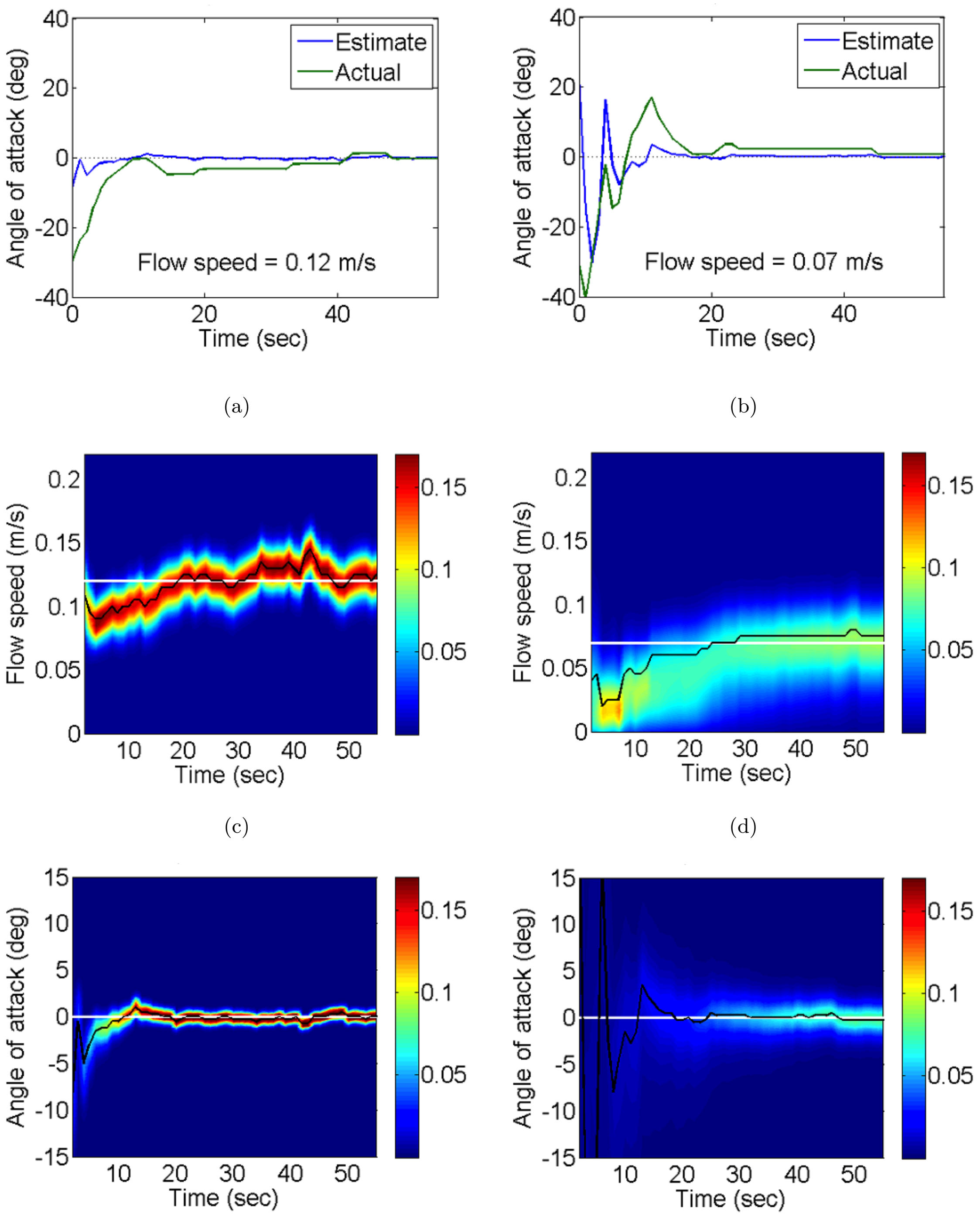

(a) (b) (c) (d) (e) (f)

Figure 4.13: Results from rheotaxis experiments using the Bayesian dynamic feedback controller with the $[\Delta p_{12}, \Delta p_{13}, \Delta p_{23}]^T$ pressure signals.

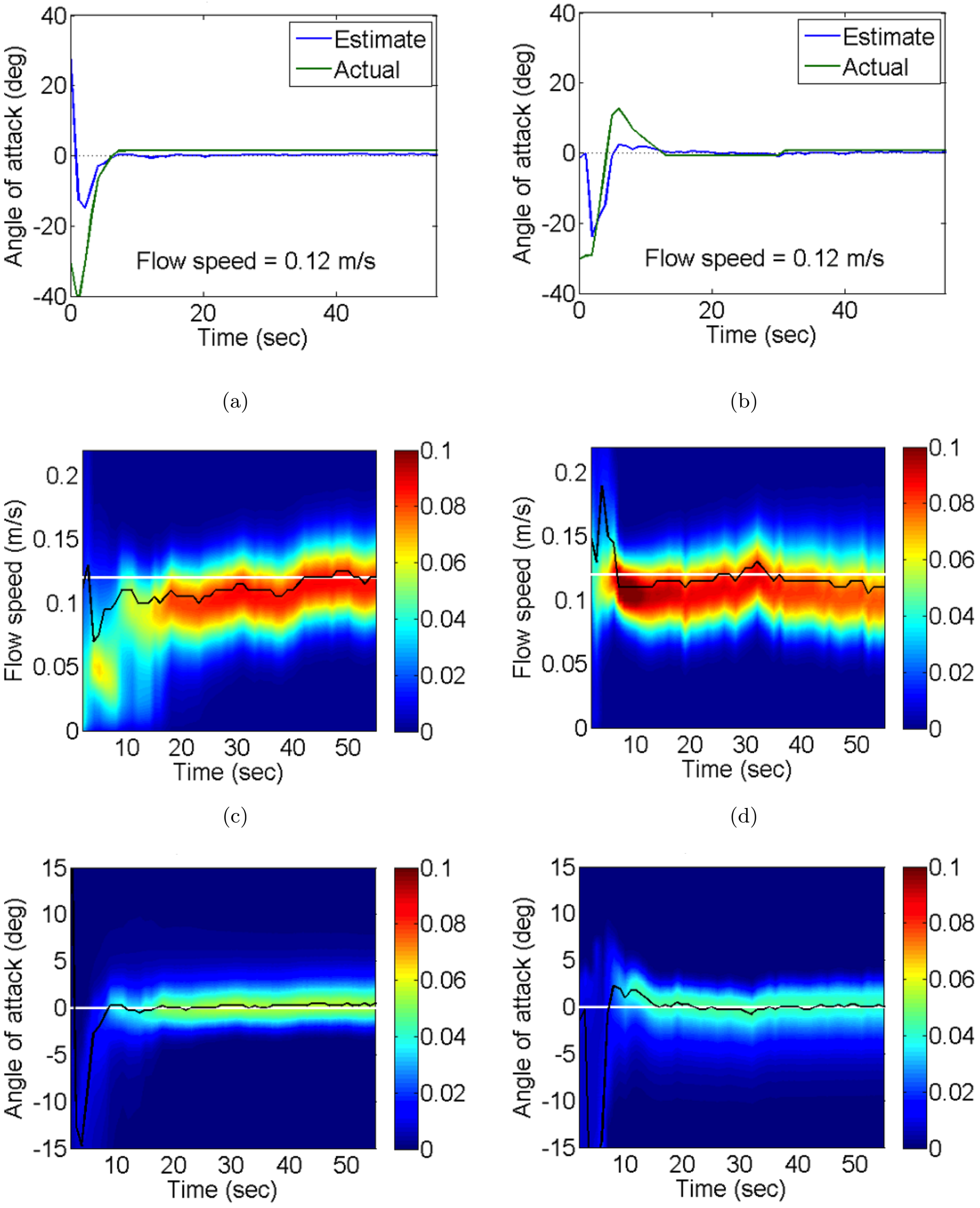

(a) (b)

(c) (d)

(e) (f)

Figure 4.14: Results from two rheotaxis experiments using the Bayesian dynamic feedback controller with two sensors. (a),(c),and (e) Using the Δp_{13} pressure signal only. (b),(d), and (f) using the Δp_{23} pressure signal only.

Chapter 5

Observability-based guidance, navigation, and control in planar flow fields

For flow-field sampling applications, such as the one presented in Chapter 7, to understand the most about the underlying flow field, a vehicle should plan paths that enhance observability of the flow field or flow-field parameters. Two possible approaches to incorporating observability in path planning are: (i) to steer the vehicle to highly observable regions of the flow field, and (ii) to select from a candidate set of controls or parameterized family of trajectories for the control that minimizes unobservability as measured by the unobservability index. The latter is referred to as observability-based path planning and is discussed in Section 5.3. This chapter combines these approaches. It first identifies multiple highly observable regions in the flow field, and use a hybrid steering controller to simulate guiding the vehicle to each of these regions. The control signals that are required for these simulations are collected into a set of candidate control signals. Observability-based path planning can then be performed utilizing this candidate set. The elements of the candidate set have the virtue that they each are guiding to a highly observable region. The observability-based path planning analysis then selects an optimizer from this set.

This chapter presents path planning of an autonomous sampling vehicle in a planar flow field using an observability-based, model-predictive control strategy. The chapter first presents how to identify highly observable regions of a flow field for a Lagrangian position sensor. It then describes a hybrid steering controller that steers the vehicle along a closed streamline in the flow field. We detail the region of validity within which convergence to a unique streamline is guaranteed. If the target streamline is chosen to be a separating boundary of invariant sets, then it corresponds with a highly observability path for a Lagrangian position sensor. By identifying high-observability regions in the flow field, simulating steering these regions, and performing observability analysis for selection of the candidate control input that maximizes observability, the result is an observability-based, model-predictive control strategy for path planning of an autonomous sampling vehicle.

5.1 Empirical observability of invariant-set boundaries

This section addresses how to find highly observable regions for sampling with a Lagrangian position sensor in the flow field. To identify such regions, it utilizes the empirical observability tool from Section 3.2 to evaluate the empirical observability index for a drifting vehicle in the two-vortex flow field from Section 2.3.1. A self-propelled vehicle will achieve different empirical observability indices, dependent on the control input. It is impossible to simulate the infinity of possible control signals for a sampling interval for this assessment. However, the influence of the flow on the self-propelled vehicle model (2.31) is the same for a drifting vehicle model (2.26) (i.e., the flow term directly impacts the vehicle's velocity). The observability results for a drifting vehicle can therefore be viewed as pertinent to a controlled vehicle.

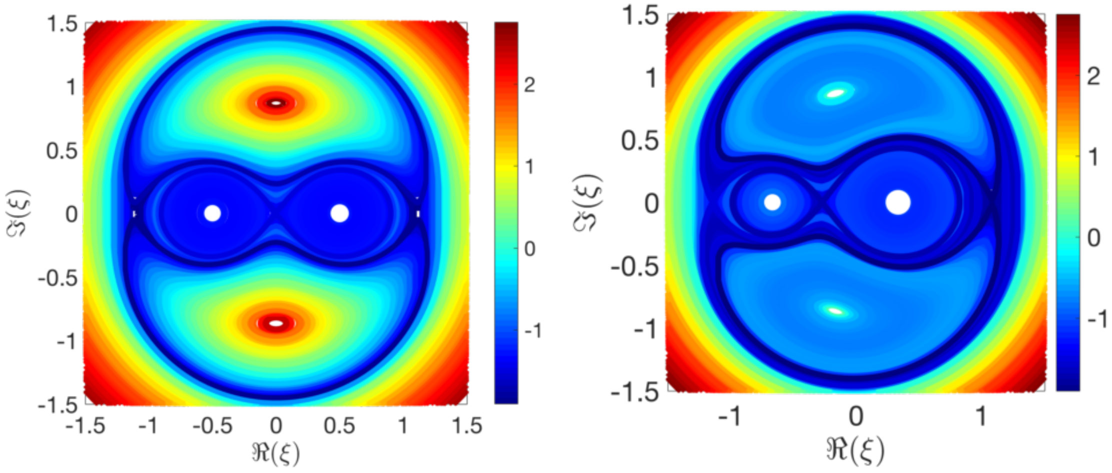

(a)

(b)

Figure 5.1: Log10 of the unobservability index for orbits in the two-vortex system for a) $\Gamma_2 = \Gamma_1$, and b) $\Gamma_2 = 2\Gamma_1$.

Orbits are of interest, both for drifting vehicles on extended deployments and for vehicles that actuate infrequently. Krener and Ide [60] examine the unobservability index over one period of the two-vortex system to assess launch locations for Lagrangian drifters. We extend this analysis to closed orbits in the following manner. First perform a grid-based unobservability analysis similar to [60], with a longer time horizon that ensures all of the drifters in the domain achieve at least one full orbit. For each orbit considered, assign to the curve the average value of the unobservability indices from the grid-based analysis. The grid-based analysis provides an estimate of the best launch location, whereas the orbit averages provide estimates from which dependence on the initial conditions has been removed. Figures 5.1(a) and 5.1(b) present the results of this calculation for equal-strength and unequal-strength cases, respectively, using 1000 orbits from random initial conditions selected from a uniform distribution over the domain and integrated over the time interval $[0, 24\pi]$. Less informative orbits in the two-vortex system occur near the center fixed points (in regions 2 and 3 for the equal-strength case in Figure 2.1(a)). Figures 5.1(a) and 5.1(b) show that the most informative orbits occur very close to the separating boundaries between invariant sets. The boundaries of invariant sets in a divergence-free flow are highly observable under Lagrangian position measurements due to the eventual distinction of neighboring trajectories by a downstream saddle point. These observations motivate Lagrangian sampling along the boundaries of invariant sets with frequent passage near saddle points.

5.2 Hybrid steering control for navigating invariant-set boundaries

The previous section identified invariant-set boundaries as highly observable regions. This section constructs a controller that steers a sampling vehicle along these paths. This section first presents a controller that can steer a controlled vehicle along a unique, closed streamline, as well as an analytical result on the region of validity for this controller based on the signed curvature of the streamline. Since the controller is not valid in all of the domain, a second controller is used to steer the vehicle to within the region of validity for the first controller. Together, these controllers comprise a hybrid steering controller.

5.2.1 Steering to unique, closed streamlines

This section extends the steering controller of Zhang and Leonard [77] in Theorem 1 to a vehicle in the presence of flow by combining it with the flow-relative transformation of [63]. Additionally, we utilize another existing technique of [97] to build a Bertand family of curves around a regular closed streamline. By synthesizing these results, we create a novel steering controller that steers a self-propelled vehicle to a unique, closed, regular streamline of an underlying flow field. Moreover, we provide precise specification of the region in which the controller is guaranteed to converge to the streamline.

Consider the self-propelled particle model in a time-invariant flow given by (2.31). Assume that the flow-relative transformation of [63] for the control signal u is valid, so that the model (2.31) may be viewed equivalently as model (2.30). Let the frame (a_1, a_2), the frame (b_1, b_2), the angle η, κ_a, and κ_b have the same meanings as defined in Section 2.4.2. Let target curve γ_0 be a twice-differentiable, simple, closed, and regular curve that may enclose a non-convex region of the plane. γ_0 also has orientation $\chi \in \{-1, +1\}$ for clockwise or countercounterwise, respectively. Appendix B describes how to create a target curve γ_0 in a given flow field by using the geometry of the saddle points and separatrices. Note that the separating boundaries of invariant sets do not meet the regularity condition at saddle points. However, smoothing of cusps using Bézier curves (see Section B.2) allows for the construction of boundaries avoiding saddles and numerically meeting these conditions.

Converging to γ_0 is accomplished by construction of a scalar orbit function $\Phi(z, \overline{z})$

for which γ_0 is a level curve (i.e., $\Phi(\gamma_0(s), \overline{\gamma_0(s)})$ is constant along the curve with arc length s). If curve γ_0 is a member of a parameterized family of curves γ_λ, such as a family of concentric ellipses, then the orbit function Φ may be constructed using the scalar parameter λ. Let the notation $(\cdot)'$ denote differentation with respect to arc length s. If γ_0 is a more general (simple, closed, and regular) curve, then an orbit function may be constructed using a Bertrand family of curves [62], i.e.,

$$\gamma_\lambda(s) = \gamma_0(s) + \lambda i \gamma_0'(s), \tag{5.1}$$

in which additional family members are formed by offsetting from γ_0 by a distance of $|\lambda|$ perpendicular to the curve (in either the positive or negative $i\gamma_0'(s)$ direction, depending on the sign of λ). The orbit function may be defined to be $\Phi(z, \overline{z}) = \lambda$ if z lies on the curve γ_λ [62]. The arc length s is measured along the reference orbit [62].

We impose the requirement that γ_0 be a streamline for a flow having stream function ψ. A unique orbit of the flow (using the Fundamental Theorem of Calculus) is

$$\gamma_0(t) = z(0) + \int_0^t -2i \frac{\partial \psi}{\partial \bar{z}}\bigg|_{z(\tau)} d\tau, \quad \text{for} \quad 0 \le t \le T, \tag{5.2}$$

where $z(0)$ is a point lying on the orbit and T is the period of the orbit. The arc length in (5.1) may be calculated using

$$s(t) = \int_0^t \left| -2i \frac{\partial \psi}{\partial \bar{z}}\bigg|_{z(\tau)} \right| d\tau. \tag{5.3}$$

To steer to the unique orbit γ_0, we construct a Bertrand family of curves γ_λ around the reference orbit so that $\Phi(z, \overline{z}) = \lambda$ is an orbit function that is zero when the vehicle lies on the curve γ_0.

Let z_c be the point on the curve γ_0 that is closest to z. Using (5.1), we can express the function $\Phi(z, \overline{z})$ as

$$\Phi(z, \overline{z}) = \langle z - z_c, b_2 \rangle \,. \tag{5.4}$$

By the construction of a Bertrand family, the orbit function's gradient $\partial\Phi/\partial\bar{z}$ is always perpendicular each Bertrand curve. Differentiating (5.4)

$$\frac{\partial \Phi}{\partial \bar{z}} = \frac{\partial}{\partial \bar{z}} \left(\frac{(z - z_0)\bar{b}_2 - (\bar{z} - \overline{z_0})b_2}{2} \right) = \frac{b_2}{2}, \tag{5.5}$$

shows that the b_2 direction also lies perpendicular to each Bertrand curve. Since we additionally require that γ_0 be a streamline of the flow, the direction b_2 can also be written in terms of a stream-function derivative evaluated at z_c, such that $b_2 = \left(\partial\psi/\partial\bar{z}/|\partial\psi/\partial\bar{z}|\right)|_{z_c}$.

Using (5.5), we calculate the remaining derivatives of Φ necessary to implement the control (2.36) in terms of the stream function as

$$\begin{aligned} \frac{\partial^2 \Phi}{\partial z \partial \bar{z}} &= \frac{1}{2\left|\frac{\partial \psi}{\partial \bar{z}}\right|} \left(\frac{\partial^2 \psi}{\partial z \partial \bar{z}} - \frac{\partial^2 \psi}{\partial z^2} b_2^2 \right), \\ \frac{\partial^2 \Phi}{\partial \bar{z}^2} &= \frac{1}{2\left|\frac{\partial \psi}{\partial \bar{z}}\right|} \left(\frac{\partial^2 \psi}{\partial \bar{z}^2} - \frac{\partial^2 \psi}{\partial z \partial \bar{z}} b_2^2 \right). \end{aligned}$$

The right-hand sides of these equations are evaluated at the point on the reference orbit

z_c nearest to the vehicle location z.

The preceding streamline steering control has assumed the existence of a unique closest point z_c on the reference curve γ_0. For a general location z in the plane near a simple, closed, and regular curve, this condition may not hold. However, by considering the signed curvature κ_s of the target curve, we define regions in which a unique closest point is guaranteed to exist. From differential curve theory, the signed curvature κ_s is defined such that [98]

$$\gamma''(s) = \kappa_s(s) i\gamma'(s). \tag{5.6}$$

Note that $\gamma'(s)$ is the tangent direction at s, and $i\gamma'(s)$ is the normal direction. According to (5.6), the signed curvature may be calculated by $\kappa_s(s) = \langle i\gamma'(s), \gamma''(s)\rangle$. The following theorem uses κ_s to define a region of validity Ω for the streamline steering control law.

Theorem 2. *Let curve γ_0 be a twice-differentiable, simple, closed, and regular curve in the plane. Let γ_I and γ_E be interior and exterior Bertrand curves, respectively, with constant offsets*

$$\begin{aligned} \lambda_I &= \frac{\chi}{\sup\limits_{\sigma} (\kappa_s(\sigma)\chi)}, \\ \lambda_E &= \frac{\chi}{\min(0, \inf\limits_{\sigma} (\kappa_s(\sigma)\chi))}, \end{aligned} \tag{5.7}$$

respectively, such that $|\lambda_I|, |\lambda_E| > 0$.[1] *Let Ω be the domain between the Bertrand curves γ_I and γ_E. If γ_I and γ_E are both simple, closed curves, then for every $z \in \Omega$, there exists*

---

[1] Note for a curve γ_0 enclosing a convex region, γ_E lies at infinity.

a unique, closest point z_c that minimizes the Euclidean distance.

Proof. The necessary and sufficient conditions for $\gamma_0(s) = z_c$ to minimize $|z - \gamma_0(s)|$ locally are

$$\left\langle \gamma_0'(s), z - z_c \right\rangle = 0, \tag{5.8}$$

$$\left\langle \gamma_0''(s), z - z_c \right\rangle < 1. \tag{5.9}$$

We prove the theorem for a point z that lies between γ_0 and γ_I; corresponding arguments hold for points between γ_0 and γ_E. Since $|\lambda_I| > 0$, and γ_I is simple by assumption, it does not have self-intersections and cannot cross γ_0. Since $|\lambda_I| \geq 0$, for every z between γ_0 and γ_I, there exists a λ and an arc length s such $0 \leq |\lambda| < |\lambda_I|$ and z lies on the Bertrand curve γ_λ. Let $z_c = \gamma_0(s)$. Plugging $z - z_c = i\lambda\gamma_0'(s)$ into the left-hand side of (5.8) yields

$$\lambda \left\langle \gamma_0'(s), i\gamma_0'(s) \right\rangle = 0,$$

so z_c satisfies the first-order necessary condition (5.8). Using (5.6) transforms the second-order condition (5.9) to

$$\kappa_s(s) \left\langle i\gamma_0'(s), z - \gamma_0(s) \right\rangle < 1 \quad \Longrightarrow \quad \kappa_s(s)\lambda < 1. \tag{5.10}$$

This inequality is trivially satisified if $\kappa_s(s) = 0$, $\lambda = 0$, or if $\kappa_s(s)\lambda < 0$, which occurs if γ_0 turns away from z for increasing s. Consider the case of $\kappa_s(s)\lambda > 0$ so that γ_0 curves towards z. Upper bounding $\kappa_s(s)\lambda$ gives

$$\kappa_s(s)\lambda \leq |\kappa_s(s)||\lambda| < \frac{|\kappa_s(s)|}{\left|\sup_{\sigma}(\kappa_s(\sigma)\chi)\right|}.$$

For an interior point z for which $\gamma_0(s)$ turns towards z, the quantity $\kappa_s(s)\chi$ is positive. Hence, the supremum operation will yield a positive value, and we have

$$\frac{\kappa_s(s)\chi}{\sup_{\sigma}(\kappa_s(\sigma)\chi)} \leq 1,$$

so that $\kappa_s(s)\lambda < 1$, satisfying condition (5.9).

For uniqueness of z_c, note that by (5.7) and the requirement that γ_0 be regular, γ_λ for each λ such that $0 \leq |\lambda| < |\lambda_I|$ does not pass through a center of curvature. Hence, γ_0 may be homotoped (i.e., continuously deformed without changing topology) using (5.1) to γ_λ for any λ in $0 \leq |\lambda| < |\lambda_I|$. z lies on only one Bertrand curve with offset λ. From above, z_c is the closest point, and this point is unique. □

Theorem 2 defines a domain Ω in which control law (2.36) using the streamline steering strategy in (5.2)–(5.7) is guaranteed to converge. We remark that it is necessary to require γ_I and γ_E to be simple curves since the offsets (5.7) may produce self-intersecting curves when used in (5.1) for some pathological curves γ_0 (e.g., when segments of γ_0 with opposing orientation have relatively close approaches, γ_I may have a self-intersection). When non-simple bounding curves result from the choice (5.7), one may reduce $|\lambda|$ until (5.1) produces bounding curves that are simple. Figure 5.2(a) illustrates the definition of

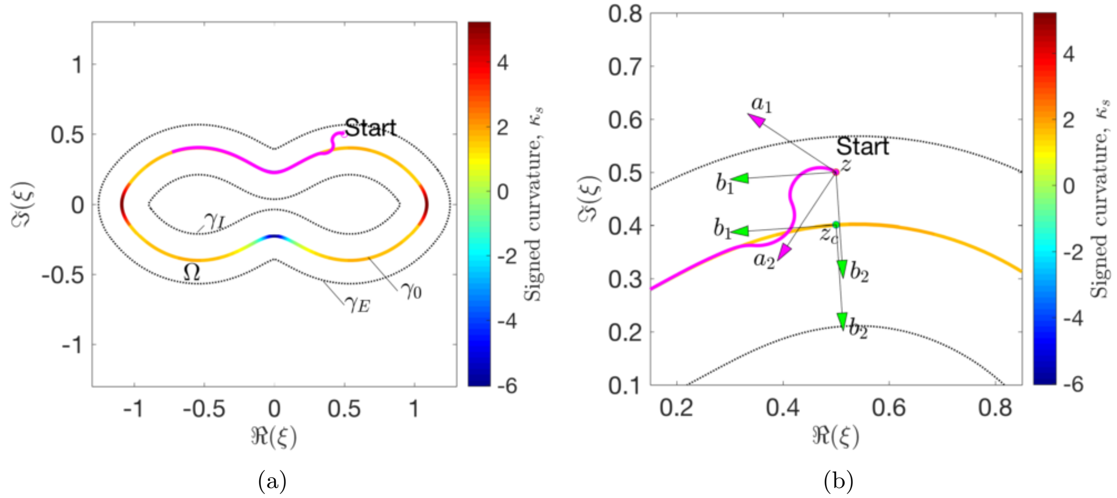

(a) (b)

Figure 5.2: a), b) Example of steering to a unique, non-convex boundary curve in the presence of flow. The inner and outer Bertrand curves γ_I and γ_E defined based on the signed curvature are shown in a); the zoom-in b) shows the necessary reference frames along with the unique, closest initial point z_c.

the domain Ω and presents an example of this steering controller for driving to a unique, closed streamline. Figure 5.2(b) shows the frames needed to utilize steering control law (2.36) for the scalar field (5.4) created by a Bertrand family of curves around a unique streamline of the flow.

5.2.2 Steering towards boundaries

The streamline controller of the previous subsection may have a limited domain of validity Ω for a given reference curve γ_0. To address this issue, we create an additional steering controller that is valid outside of Ω by allowing the stream function ψ (or ψ_R if the co-rotating frame is used, as in Chapter 7) to serve as the scalar Θ function given in Theorem 1. When a vehicle is not within an applicable domain Ω of a boundary curve, then we take the stream-function value of the closest boundary curve as the target value Θ^d from Theorem 1. This controller drives the vehicle towards the boundaries of invariant sets. Once the vehicle enters the domain Ω of a boundary curve, it steers according to the unique streamline controller described previously. Working together, these two controllers comprise a hybrid control strategy.

5.3 Observability-based path planning

Observability-based path planning of autonomous sampling platforms for flow estimation is a technique by which candidate trajectories are evaluated based on their ability to enhance the observability of underlying flow-field parameters. Observability-based path planning refers to the evaluation of a finite set of l possible control signals $\{u^j(\cdot)\}_{j=1}^l$ over a forward-looking time interval $[t_0, T_h]$ based on the anticipated observability of the output. The candidate signal may be generated by another control policy (e.g., steering to the

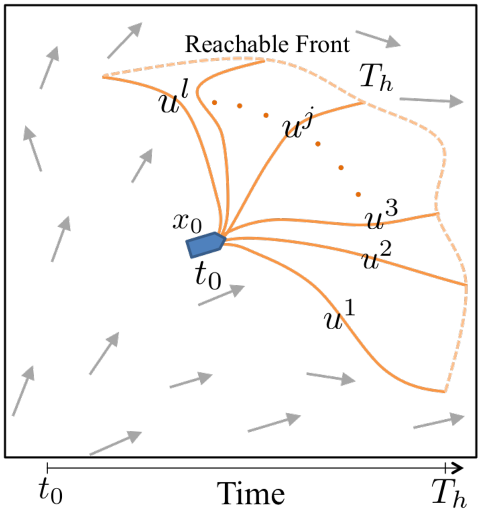

Figure 5.3: Candidate trajectories in observability-based path planning.

boundaries of invariant sets) or generated from a parameterized family of possible vehicle trajectories (e.g., circular loops [88] or superellipses [99]). Each control signal is scored using its unobservability index (3.21). The control signal that minimizes the unobservability index is selected, and the process may be repeated when re-planning is desired [69]. Figure 5.3 illustrates this process.

Chapter 6

Augmented observability-based path planning

Until now, observability-based path planning (as presented in Chapter 5) has optimized path selection for observability without consideration of where the vehicle has already been or what may already known about the system under observation. A motivating example in this chapter shows that vehicle path history alters the optimal path in observability-based path planning and that vehicle history must be considered in planning.

Performing observability-based path planning in an estimated environment requires observability computations using a state or parameter vector that may contain uncertainties. This chapter presents a novel approach that makes use of the background error covariance at the current time to account properly for uncertainty of the underlying flow. The reduced Hessian of an optimal data-assimilation strategy, Incremental 4D-Var, properly accounts for prior information (under a Gaussian uncertainty assumption) in the linear case and must be full rank to infer the initial state. The reduced Hessian represents an observability Gramian *augmented* with an inverse prior covariance. We extend augmented observability to the nonlinear case through the use of an empirical Gramian, yielding a new criterion for scoring candidate trajectories: the empirical augmented unobservability index.

The augmented observability Gramian has strong connections to other inference matrices in estimation theory and information theory. Solving the differential Riccati equation for the covariance of the Kalman Filter under deterministic dynamics also properly accounts for prior information in the linear case, but at a later time. The solution to this equation reveals the important distinctions between observability-based, augmented observability-based, and anticipated covariance-based path planning. Section 6.4.2 makes a connection to information theory by showing that the empirical observability Gramian is a numerical approximation to the Fisher information matrix for inference of the initial condition.

A numerical experiment in this chapter shows that by augmenting the forward-looking observability analysis with prior information, the optimal vehicle path is the path with observability content most complementary to the prior information for inferring the initial state of the system. In addition, this chapter expands augmented observability path-planning to non-Gaussian prior distributions represented by a GMM. This extension involves an approximate expected-cost calculation for the augmented unobservability index using the components of the GMM as weighted realizations from the non-Gaussian distribution.

6.1 Motivating example: Effect of vehicle history on path selection

The following example motivates the need to evaluate forward-looking paths with consideration of where the vehicle has already been or what the vehicle already knows, i.e., to incorporate prior information in observability-based path planning.

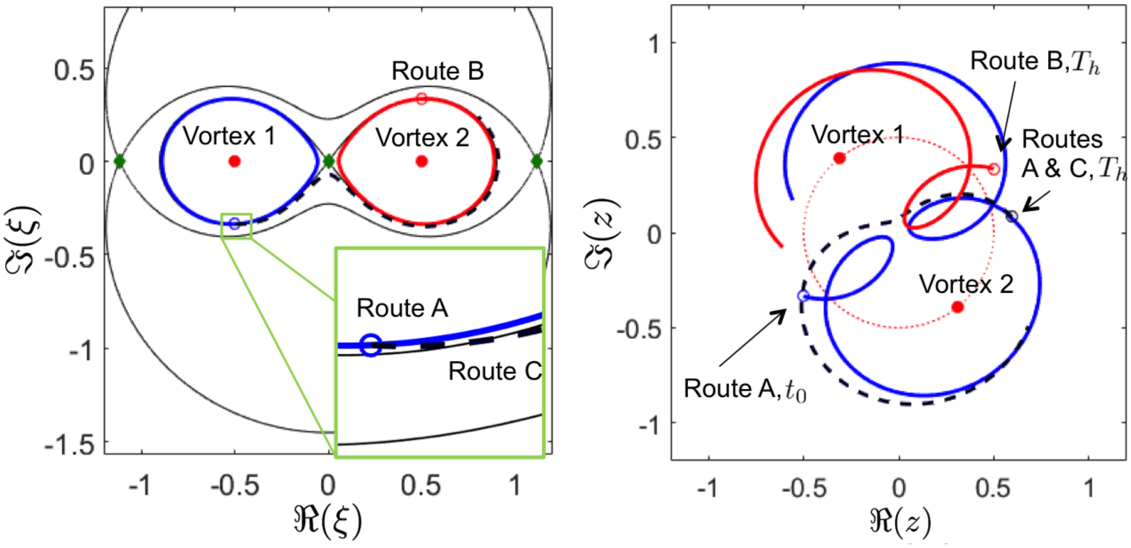

(a) (b)

Figure 6.1: (a) Routes in the observability example in the co-rotating frame. (b) Routes in the observability example in the inertial frame. Initial conditions for Route A: $x(0) = (1, -.5, 0, 1, .5, 0, -.5, -.335)^T$; Route B: $x(0) = (1, -.5, 0, 1, .5, 0, .5, .335)^T$; Route C: $x(T_h) = (1, .45, -.22, 1, -.45, .22, .60, .081)^T$.

Consider a drifting ocean vehicle located at z, advecting with the flow of two nearby vortices. Assume, for simplicity, that we are able to able apply control $u(t) \in \mathbb{C}$ directly to the vehicle velocity, leading to the kinematic model

$$\dot{z}(t) = f_1(z(t)) + f_2(z(t)) + u(t), \tag{6.1}$$

where f_j is the flow contribution from the jth vortex according to (2.21). Note empirical observability calculations in which a control signal is prescribed over a time interval are unaffected by the point of entry of the control term since it only acts as a prescribed function of time over the specified interval. Figures 6.1(a) and 6.1(b) show the setup for this motivating example in the co-rotating and inertial frames, as described for the two-vortex system in Chapter 2.

Assume that the vehicle has traversed Route A encircling Vortex 1 during time interval $[0, T_h]$, as shown in Figure 6.1(a); T_h is approximately 8.44 time units, corresponding to the time for the drifting vehicle to complete the blue orbit and return to its starting location in the co-rotating frame. After time T_h, the vehicle will again approach the saddle location at $\xi = 0$. Figure 6.1(a) shows two possible choices at $t = T_h$: the vehicle can remain on Route A encircling Vortex 1, or switch to Route C, which requires a brief control action to cross the nearby separating boundary. (Route B will be addressed in Section 6.5.) After crossing, a vehicle traveling along Route C drifts to the right of the saddle at $\xi = 0$ and partially encircles Vortex 2. Should the vehicle remain on Route A for the subsequent time interval $[T_h, 2T_h]$ or exert a brief control effort to switch to Route C?

Table 6.1 shows the unobservability indices for the upper 6×6 submatrix of $\mathcal{W}_{\text{eo}}$ corresponding to the observability of the flow-field parameters and states γ_1, $\Re(z_1)$, $\Im(z_1)$, γ_2, $\Re(z_2)$, and $\Im(z_2)$, for these routes. Forward looking-observability on $[T_h, 2T_h]$ shows Route A as preferable to Route C. However, if the previous empirical observability Gramian from $[0, T_h]$ for Route A is included in the evaluation, the route combination (A, C) yields the most observable path. The value of the unobservability index over the interrupted intervals $[0, T_h], [T_h, 2T_h]$ differs from the index over the continuous interval $[0, 2T_h]$, since new perturbed initial conditions are selected at time T_h in the interrupted case. Moreover, note that the unobservability index for Route A differs between intervals $[0, T_h]$ and $[T_h, 2T_h]$, because the vortices in the inertial frame are at a different phase of rotation for these times.

Table 6.1: Unobservability analysis of Routes A and C

Time span: $[0, T_h]$		$[T_h, 2T_h]$		$[0, T_h], [T_h, 2T_h]$	
Route	Unobs.	Route	Unobs.	Routes	Unobs.
A	6.222	A	8.444	(A,A)	0.2927
C	-	C	27.50	(A,C)	0.2537

The results of this numerical experiment show that the historical information changes route selection. Moreover, including the observability for the portion of path already covered by a vehicle appears to be an appropriate method for incorporating historical information. However, the states of the vehicle and the flow field may be uncertain. Such evaluations should involve the best estimate of the system state at time t_0 and ideally incorporate the uncertainty about that state. In the sequel, all prior information of the system up until time t_0 is assumed to be encoded in a background error covariance matrix P_0.

6.2 Observability with stochastic measurements

This section presents the linear observability Gramian for the case of stochastic measurements, as well as the empirical version. We subsequently use these expressions in Section 6.3.

6.2.1 Error covariance and stochastic observability

Consider the stochastic system (3.1), with state vector $x(t) \in \mathbb{R}^n$, output vector $y(t) \in \mathbb{R}^p$, real-valued, time-varying matrices $A(t)$, $G(t)$, and $C(t)$, white Gaussian process noise $w(t)$ with covariance $Q(t)$, and white Gaussian measurement noise $v(t)$ with covariance $R(t)$ [100]. For notational simplicity, we suppress time-dependence in what follows.

The continuous-time Kalman Filter provides the optimal, minimum-variance, unbaised estimate for the system (3.1). In addition, the Kalman Filter provides an estimate of the error covariance, which describes the uncertainty in the state estimates. The error covariance $P(t) \in \mathbb{R}^{n\times n}$ evolves according to the differential Riccati equation [100]

$$\dot{P} = AP + PA^T + GQG^T - PC^TR^{-1}CP. \tag{6.2}$$

Consider (3.1) with deterministic dynamics such that $Q(t) \equiv 0$. Gelb *et al.* multiply the left- and right-hand sides of the (6.2) by $-P^{-1}$ and P^{-1}, respectively, then use the identity $\dot{P}^{-1} = -P^{-1}\dot{P}P^{-1}$ to transform the differential Riccati equation (6.2) into a differential Lyapunov equation in terms of the precision matrix P^{-1}, i.e.,[100]

$$\frac{d}{dt}\left(P^{-1}\right) = -P^{-1}A - A^T P^{-1} + C^T R^{-1} C, \tag{6.3}$$

with $P^{-1}(t_0) = 0_{n\times n}$ for the case of no prior information. With the use of Liebniz's rule, the solution to this equation, verified via substitution, is [100]

$$P^{-1}(t) = \int_{t_0}^{t} \Phi^T(\tau,t) C^T R^{-1} C \Phi(\tau,t) d\tau. \tag{6.4}$$

The right-hand side of (6.4) must be positive definite for some $t > t_0$ for observability [100]. This integral closely resembles the linear observability Gramian (3.16), except the arguments of Φ are (τ,t) instead of (τ,t_0). Multiplying (6.4) on the left by $\mathbb{I} = \Phi^T(t,t_0)^{-1}\Phi^T(t,t_0)$ and on the right by $\mathbb{I} = \Phi(t,t_0)\Phi(t,t_0)^{-1}$, and using the composition property $\Phi(\tau,t_0) = \Phi(\tau,t)\Phi(t,t_0)$ yields

$$\begin{aligned} P^{-1}(t) &= \Phi^T(t_0,t)\left(\int_{t_0}^{t} \Phi^T(\tau,t_0) C^T R^{-1} C \Phi(\tau,t_0) d\tau\right)\Phi(t_0,t) \\ &= \Phi^T(t_0,t)\mathcal{W}_{\text{so}}(t_0,t)\Phi(t_0,t), \end{aligned} \tag{6.5}$$

where $\mathcal{W}_{\text{so}}$ defines the stochastic observability Gramian for (3.1) with $Q(t) \equiv 0$. $\mathcal{W}_{\text{so}}$ resembles the linear deterministic observability Gramian with an inclusion of R^{-1} for measurement noise. Aoki [101] defined an analogous discrete-time stochastic observability Gramian containing the measurement noise covariance. The connection between error covariance and observability is apparent in the linear case: the inverse of the error covariance of the optimal filter for a linear time-varying system with deterministic dynamics is given by the stochastic observability Gramian transformed by $\Phi^T(t_0, t)$ and $\Phi(t_0, t)$.

6.2.2 Empirical observability with stochastic measurements

Consider the nonlinear system (3.17) with the addition of measurement noise,

$$\begin{aligned} \dot{x}(t) &= g(t, x(t)) \\ y(t) &= h(t, x(t)) + v(t), \end{aligned} \tag{6.6}$$

where $v(t)$ is white Gaussian noise with covariance $R(t)$. The dynamics in (6.6) are unaffected by the inclusion of the measurement noise. Hence, the reference trajectory x_r defined in Section 3.2 is unaffected by this change. If we specify that the output reference trajectory should be the ensemble-averaged output corresponding to the x_r trajectory, then we recover y_r without the need to change notation, and (3.18) similarly holds.

We construct an empirical Gramian for system (6.6) in the same manner as Krener and Ide [60], however, we include the measurement covariance $R(t)$ to mirror the linear, stochastic observability Gramian. Hence, with a slight abuse of notation, we replace (3.19) with

$$\mathcal{W}_{\text{eo}}(t_0, t_f, x(t_0)) = \int_{t_0}^{t_f} \Psi_{\text{e}}(\tau, t_0, x(t_0))^T R^{-1}(\tau) \Psi_{\text{e}}(\tau, t_0, x(t_0)) d\tau, \tag{6.7}$$

if stochastic measurements are present. The sensitivity matrix Ψ_{e} is still defined by (3.20).

Note that in the limit $\epsilon \to 0$, (6.7) converges to the local, stochastic observability

Gramian $\mathcal{W}_{\mathrm{so}}$ in (6.5) for the tangent-linear model (3.18). Inclusion of the $R(\tau)^{-1}$ term accounts for the affect of measurement covariance on observability and matches its placement within the linear stochastic observability Gramian. Krener and Ide [60] omit the $R(\tau)^{-1}$ term but note that the outputs can be scaled so that the noise has unit covariance.

6.3 Augmented observability

This section considers the variational data assimilation strategy Incremental 4D-Var with deterministic, linear dynamics and uncertain measurements. These dynamics correspond to a tangent-linear approximation of a nonlinear system, similar to the tangent-linear model used in the definition of empirical observability by Krener and Ide [60]. The optimal solution of this problem requires inversion of a matrix known as the reduced Hessian. Since the reduced Hessian consists of the linear stochastic observability Gramian with the addition of an inverse background error covariance, we refer to it as the augmented observability Gramian. For nonlinear systems, we utilize an empirical Gramian within augmented observability to yield empirical augmented observability and an index associated with its minimum eigenvalue that is useful for path planning. We also derive a useful upper bound on the empirical augmented unobservability index.

6.3.1 Incremental 4D-Var for optimal linear estimation

Incremental 4D-Var is a technique in data assimilation originating in numerical weather prediction and oceanography that provides smoothed estimates[1] of a trajectory

---

[1] The term smooth does not refer to differentiablility here. A smoothing algorithm uses measurements over the entire estimation time interval simultaneously during each estimation step.

of a dynamical system [102]. The name originates from the use of spatial, dynamical models of the weather and ocean (3D in space + 1D for time) as well as techniques from the calculus of variations. Under deterministic dynamics, solving for the optimal initial condition estimate $\hat{x}_0$ that results in a trajectory that is best fit to the data is equivalent to solving for the entire best-fit trajectory $\hat{x}(\cdot)$ over time interval $[t_0, t_f]$. Consider the following continuous-time, optimal estimation problem with a linear dynamical constraint. Given an estimate $\hat{x}_0$ of the initial state with covariance P_0, let $\hat{x}(\cdot)$ denote the nonlinear trajectory resulting from $\hat{x}_0$. Let $C(t)$ denote the observation operator of the tangent-linear model (3.18), and let $\Delta y(t) = y(t) - \hat{y}(t)$ be the difference between measurement $y(t)$ and the expected measurement $\hat{y}(t)$ corresponding to estimate $\hat{x}_0$. Incremental 4D-Var seeks an updated estimate $\hat{x}_0 + \delta x_0$ of the initial condition for which the update δx_0 minimizes (with τ arguments suppressed)

$$J(\delta x) = \frac{1}{2}\int_{t_0}^{t_f} \Big(\Delta y(\tau) - C(\tau)\delta x(\tau)\Big)^T R^{-1}(\tau)\Big(\Delta y(\tau) - C(\tau)\delta x(\tau)\Big) d\tau + \frac{1}{2}\delta x(t_0)^T P_0^{-1} \delta x(t_0) \tag{6.8}$$

subject to

$$\frac{d}{dt}\left(\delta x(t)\right) = \frac{\partial f}{\partial x}\Big|_{\hat{x}_r(t)} \delta x(t) \qquad \text{with} \qquad \delta x(t_0) = \delta x_0. \tag{6.9}$$

The cost function (6.8) has continuous-time measurements but is otherwise identical to the Incremental 4D-Var approach of Courtier *et al.* [103]; eqn. (6.8) can therefore be thought of as the incremental cost function in the inner loop of an Incremental 4D-Var implementation. Since the dynamics are linear and deterministic, we may solve (6.9) in terms of δx_0, i.e.,

$$\delta x(t) = \Phi(t, t_0)\delta x_0. \tag{6.10}$$

Using (6.10) and $\delta x(t_0) = \delta x_0$ converts (6.8) to the unconstrained cost function (with most τ arguments suppressed)

$$J_0(\delta x_0) = \frac{1}{2}\int_{t_0}^{t_f} \Big(\Delta y - C\Phi(\tau, t_0)\delta x_0\Big)^T R^{-1} \Big(\Delta y - C\Phi(\tau, t_0)\delta x_0\Big) d\tau + \frac{1}{2}\delta x_0^T P_0^{-1} \delta x_0. \tag{6.11}$$

A first-order necessary condition for optimality results from requiring the Fréchet derivative of J_0 evaluated along perturbation direction η to vanish for all η, i.e.,

$$\frac{d}{d\epsilon} J_0(\delta x_0 + \epsilon\eta)\Big|_{\epsilon=0} = 0 \qquad \forall \eta. \tag{6.12}$$

Since P_0^{-1} and R^{-1} are symmetric matrices, this yields

$$\eta^T \left(-\int_{t_0}^{t_f} \Phi(\tau, t_0)^T C^T R^{-1} \Big(\Delta y - C\Phi(\tau, t_0)\delta x_0\Big) d\tau + P_0^{-1}\delta x_0 \right) = 0.$$

Since this expression is zero for any η, the parenthesized terms must be identically zero, yielding the linear equation for δx_0

$$\left(\int_{t_0}^{t_f} \Phi(\tau, t_0)^T C^T R^{-1} C \Phi(\tau, t_0) d\tau + P_0^{-1} \right) \delta x_0 = \int_{t_0}^{t_f} \Phi(\tau, t_0)^T C^T R^{-1} \Delta y \, d\tau. \tag{6.13}$$

Note the left-hand side of (6.13) contains both the linear stochastic observability Gramian $\mathcal{W}_{\text{so}}(t_0, t_f)$ and the background error covariance. This equation may be solved uniquely for δx_0 if and only if the matrix inverse of the parenthesized term in (6.13) exists, i.e., it is full rank. Typically, the observability Gramian should be full rank to able to infer the initial state of the system. Here this requirement is relaxed because the presence of P_0^{-1} ensures invertibility. In Incremental 4D-Var data assimilation, the parenthesized term is known as the reduced Hessian [104]. Due to the formulation in terms of observability with the addition of prior inverse covariance P_0, we refer to this matrix as the augmented observability Gramian

$$\mathcal{W}_{\text{ao}}(t_0, t_f) = \mathcal{W}_{\text{so}}(t_0, t_f) + P_0^{-1}. \tag{6.14}$$

For linear, discrete-time dynamics, Li and Navon [104] have shown the equivalence of 4D-Var and Kalman Filter estimates. They have also shown a connection between the inverse of the reduced Hessian and the covariance of the Kalman Filter in discrete-time. These results motivate the solution in the next section on the covariance of the Kalman Filter for deterministic dynamics in continuous time.

6.3.2 Empirical augmented observability

To extend the linear augmented observability Gramian $\mathcal{W}_{\text{ao}}$ in (6.14) to nonlinear dynamics, we replace the linear stochastic observability Gramian $\mathcal{W}_{\text{so}}(t_0, t_f)$ with the stochastic version of the empirical observability Gramian $\mathcal{W}_{\text{eo}}(t_0, t_f)$ defined in (3.19). The empirical augmented observability Gramian is

$$\mathcal{W}_{\text{ea}}(t_0, t_f, x(t_0), P_0) = \int_{t_0}^{t_f} \Psi_{\text{e}}(\tau, t_0, x(t_0))^T R(\tau)^{-1} \Psi_{\text{e}}(\tau, t_0, x(t_0)) d\tau + P_0^{-1}$$

$$= \mathcal{W}_{\text{eo}}(t_0, t_f, x(t_0)) + P_0^{-1}. \tag{6.15}$$

We suppress the dependence of $\mathcal{W}_{\text{ea}}$ on $x(t_0)$ and P_0, except when it is needed for clarity.

We also define the empirical augmented unobservability index to be

$$\nu_a\left(\mathcal{W}_{\text{ea}}\right) = \frac{1}{\lambda_{\min}(\mathcal{W}_{ea})} = \frac{1}{\lambda_{\min}\left(\mathcal{W}_{eo} + P_0^{-1}\right)}. \tag{6.16}$$

We use this index in Section 6.5 and Chapter 7 for path planning.

For two matrices V and W, it can be shown through use of an eigenvector of $V + W$ and Rayleigh quotients that $\lambda_{\min}(V) + \lambda_{\min}(W) \leq \lambda_{\min}(V + W)$ [105]. This identity leads to the upper bound on the index (6.16), given by

$$\nu_a\left(\mathcal{W}_{\text{ea}}\right) \leq \frac{\nu\left(\mathcal{W}_{\text{eo}}\right)}{1 + \nu\left(\mathcal{W}_{\text{eo}}\right)/\lambda_{\max}\left(P_0\right)}, \tag{6.17}$$

where we have used the fact that $\lambda_{\min}\left(P_0^{-1}\right) = 1/\lambda_{\max}\left(P_0\right)$. Note that if we have perfect initial knowledge of the state so that $P_0 \to 0$, then the ν_a index tends to zero, indicating that the system is perfectly observable based on prior information alone. Similarly, if $\nu \to 0$, then ν_a goes to zero, so that perfect observability in $\mathcal{W}_{\text{eo}}$ leads to perfect observability in $\mathcal{W}_{\text{ea}}$. Also note that if we have no initial knowledge of the system state, i.e., $P_0 \to \infty$, then $\nu_a \leq \nu$.

6.4 Connections to existing inference matrices

The minimum-variance solution for a posterior filter covariance is given by the continuous-time Kalman Filter, which provides a differential Riccati equation describing its evolution. The analytical solution to this differential Riccati equation connects the inverse covariance of a Kalman Filter to the augmented observability Gramian. The empirical augmented observability Gramian also connects to information theory since the empirical observability Gramian (without prior information) can be shown to be an approximation to the Fisher information matrix for initial condition inference.

6.4.1 Connection to the Kalman Filter covariance

The solution (6.4) to (6.3) (equivalently (6.2) with $Q(t) \equiv 0$) requires the assumption of zero prior information. The solution to (6.2) when prior information is present was noted to exist [79] in the work of Levin [106]. However, the solution in [106] requires knowledge of all entries of a state transition matrix for an associated Hamiltonian dynamical system (which is not easily found, even in the time-invariant case), and the solution is not given explicitly in terms of the stochastic observability Gramian. This section presents a solution for the inverse covariance of the continuous-time Kalman Filter for deterministic dynamics.

Since augmented observability $\mathcal{W}_{\text{ao}}(t_0, t_f)$ is a quantity that results from a smoothing operation (Incremental 4D-Var) and applies at time t_0 and (6.3) is a filtering equation applicable at time t_f, to solve (6.3) the augmented observability $\mathcal{W}_{\text{ao}}(t_0, t_f)$ must be transformed by $\Phi^T(t_0, t_f)$ and $\Phi(t_0, t_f)$ similar to (6.5). This observation suggests the following solution to (6.3).

Theorem 3. *The inverse covariance of the continuous-time Kalman Filter under deterministic linear dynamics and in the presence of initial covariance P_0 is*

$$\begin{aligned} P^{-1}(t) &= \Phi^T(t_0,t)\mathcal{W}_{ao}(t_0,t)\Phi(t_0,t) \\ &= \Phi^T(t_0,t)\left(\mathcal{W}_{so}(t_0,t)+P_0^{-1}\right)\Phi(t_0,t). \end{aligned} \tag{6.18}$$

Proof. Note at $t = t_0$, $\Phi(t_0,t_0)=\mathbb{I}$ and $\mathcal{W}_{\text{so}}(t_0,t_0)=0$, hence $P^{-1}(t_0)=P_0^{-1}$ as desired. We must verify that (6.18) is a solution to (6.3). Consider the left-hand side of (6.3) by differentiating the proposed solution, which gives

$$\frac{d}{dt}\left(P^{-1}(t)\right) = \dot{\Phi}^T\left(\mathcal{W}_{\text{so}}+P_0^{-1}\right)\Phi + \Phi^T\frac{d}{dt}\Big(\mathcal{W}_{\text{so}}\Big)\Phi + \Phi^T\left(\mathcal{W}_{\text{so}}+P_0^{-1}\right)\dot{\Phi}, \tag{6.19}$$

where $\Phi = \Phi(t_0,t)$ and $\mathcal{W}_{\text{so}} = \mathcal{W}_{\text{so}}(t_0,t)$. Differentiation of $\mathcal{W}_{\text{so}}(t_0,t)$ yields

$$\frac{d}{dt}\Big(\mathcal{W}_{\text{so}}(t_0,t)\Big) = \Phi^T(t,t_0)C^T(t)R^{-1}(t)C(t)\Phi(t,t_0). \tag{6.20}$$

Recall from linear systems theory [107] the transition matrix property

$$\dot{\Phi}(t_0,t) = -\Phi(t_0,t)A(t). \tag{6.21}$$

Substituting (6.20) into (6.19) and using the composition property to show $\Phi^T(t_0,t)$ $\Phi^T(t,t_0) = \mathbb{I}$ and $\Phi(t,t_0)\Phi(t_0,t) = \mathbb{I}$ results in the desired left-hand side. Plugging (6.18) into the right-hand side of (6.3) gives a matching expression. □

This result is important because it connects the optimal filter covariance to the augmented observability Gramian and enables the following distinctions between path-planning methods given in Section 6.5.1.

6.4.2 Connection to the Fisher information matrix

This section connects empirical and empirical augmented observability to Fisher information for the system (6.6) with an uncertain initial condition $x(t_0) \sim \mathcal{N}(x_0, P_0)$ and constant measurement noise covariance R.

Let $p(Z|\Omega)$ denote the conditional probability density associated with measurements Z of the output of a system with an underlying parameter vector Ω. Let $\mathbb{E}[\cdot]$ denote the expectation operator. From information theory, the Fisher information matrix (FIM), defined component-wise by [108]

$$[\mathcal{F}(Z, \Omega)]_{jk} = -\mathbb{E}\left(\frac{\partial^2}{\partial \Omega_j \partial \Omega_k} \log p(Z|\Omega)\right), \tag{6.22}$$

assesses the informativeness of measurements Z in the inference of Ω. The FIM inverse provides the Cramér-Rao lower bound on the covariance $C_{\hat{\Omega}}$ of estimates $\hat{\Omega}$ generated by an unbiased estimator (i.e., $C_{\hat{\Omega}} \geq F^{-1}$) [108].

One may distinguish versions of the FIM by the pdf substituted for $p(Z|\Omega)$. Linear information filters, which are Kalman Filters formulated to propagate the inverse of the state covariance, use the filtering density $p(y(t_f)|x)$ for the measurement vector $y(t_f)$

conditioned on the signal $x(\cdot)$ over the interval $[t_0, t_f]$ to obtain $\mathcal{F}\left(y(t_f), x\right) = P^{-1}(t_f)$ given in (6.4). Powel and Morgansen [89] connect the time-derivative of the empirical observability Gramian to $F\left(y(t_f)|x(t_0)\right)$, which is based on the latest measurement and the initial condition, in the limit of (3.20) as $\epsilon \to 0$. Here, we consider the likelihood density $p(y|x(t_0))$ for the continuous-time signal $y(\cdot)$ over the interval $[t_0, t_f]$, conditioned on the uncertain initial condition $x(t_0)$.

Calculation of the FIM using the $p(y|x(t_0))$ density for signal $y(\cdot)$ requires stochastic analysis that properly accounts for the nonconstant offset $h(t, x(t))$ in the output equation of (6.6); we follow Law *et al.* [109], who derive a related expression for a posterior density. Consider a constant measurement covariance $R(t) = R$. Define the integrated stochastic process $Y(t) = \int_{t_0}^{t} y(\tau) d\tau$ and let $\beta \in \mathbb{R}^m$ be a standard Brownian motion with time shift t_0 such that $\beta(t_0) = 0$ and $\mathbb{E}\left(\beta(t_0+1)^2\right) = 1$. For a given $x(t_0)$ and the corresponding trajectory $\phi(\cdot, t_0, x(t_0))$, the output equation of (6.6) can be represented by the Itô process [109]

$$dY(t) = h(t, \phi(t, t_0, x(t_0)))dt + \sqrt{R} d\beta(t). \tag{6.23}$$

Let $Y_R(\cdot)$ be an associated reference process that is the solution to the driftless version of (6.23), i.e., when $h(\cdot, \phi(\cdot, t_0, x(t_0))) \equiv 0$, over the time interval $[t_0, t_f]$. For brevity, we suppress the arguments of ϕ. For (6.23) with uncertain $x(t_0)$, Girsanov's formula [109, 110]

$$\frac{p\left(Y, x(t_0)\right)}{p\left(Y_R, x(t_0)\right)} = \exp\left(-\frac{1}{2}\int_{t_0}^{t_f} \|h(\tau, \phi(\tau, t_0, x(t_0)))\|_R^2 d\tau + \int_{t_0}^{t_f} \left\langle h(\tau, \phi(\tau, t_0, x(t_0))), dY(\tau)\right\rangle_R\right). \tag{6.24}$$

provides a means of obtaining the relevant joint density $p(Y, x(t_0))$ in relation to a driftless reference system. The second integral in (6.24) is an Itô integral, where the bracketed integrand is the weighted inner product $\langle a, b\rangle_R = (R^{-1/2}a)^T(R^{-1/2}b)$. Girsanov's formula enables the following connection between empirical observability and the FIM.

Theorem 4. *For system* (6.6) *with an uncertain initial condition* $x(t_0) \sim \mathcal{N}\left(x_0, P_0\right)$ *and measurement noise* $v(t) \sim \mathcal{N}\left(0, R\right)$*, the empirical observability Gramian* (3.19) *is a numerical approximation to the Fisher information matrix* $\mathcal{F}(y, x(t_0))$ *if the likelihood density* $p\left(y|x(t_0)\right)$ *is differentially smooth.*

Proof. First, note that $p(Y|x(t_0)) = p(y|x(t_0))$ for signals $Y(\cdot)$ and $y(\cdot)$. The independence of Y_R and $x(t_0)$ implies

$$\frac{p\left(Y, x(t_0)\right)}{p\left(Y_R, x(t_0)\right)} = \frac{p\left(Y|x(t_0)\right)}{p\left(Y_R\right)}. \tag{6.25}$$

By the property of logarithms $\log\left(A/B\right) = \log A - \log B$ and the absence of $x(t_0)$ from $p(Y_R)$, note that

$$\frac{\partial^2}{\partial x(t_0)_j \partial x(t_0)_k} \log p\left(Y|x(t_0)\right) = \frac{\partial^2}{\partial x(t_0)_j \partial x(t_0)_k} \log \frac{p\left(Y|x(t_0)\right)}{p\left(Y_R\right)}. \tag{6.26}$$

Combining (6.26) with (6.22) yields FIM entries

$$[\mathcal{F}\left(y,x(t_0)\right)]_{jk}=\mathbb{E}\left(\frac{\partial^2}{\partial x(t_0)_j\partial x(t_0)_k}\left(\frac{1}{2}\int_{t_0}^{t_f}\|h(\tau,\phi(\tau,t_0,x(t_0)))\|_R^2 d\tau\right.\right.$$
$$\left.\left.-\int_{t_0}^{t_f}\langle h(\tau,\phi(\tau,t_0,x(t_0))),dY(\tau)\rangle_R\right)\right). \tag{6.27}$$

By the smoothness assumption on $p\left(y|x(t_0)\right)$, the expectation and the partial differentiation operations may commute. The expectation of an Itô integral is zero [109], so the second term provides zero contribution. Differentiation of the first term yields

$$\mathcal{F}\left(y,x(t_0)\right)=\int_{t_0}^{t_f}\frac{\partial h\left(\tau,\phi\right)}{\partial x(t_0)}^T R^{-1}\frac{\partial h\left(\tau,\phi\right)}{\partial x(t_0)}d\tau. \tag{6.28}$$

Following [89] in passing (6.6) to a limit as $\epsilon\to 0$ gives

$$\lim_{\epsilon\to 0}\mathcal{W}_{\text{eo}}(t_0,t_f)=\mathcal{F}\left(y,x(t_0)\right). \tag{6.29}$$

This expression reveals that $\mathcal{W}_{\text{eo}}(t_0,t_f)$ is an approximation to $\mathcal{F}\left(y,x(t_0)\right)$ for nonvanishing values of ϵ. □

The FIM assesses the inference certainty due to measurement data alone [111], so prior information does not appear in (6.29). Including prior information, the relation between the FIM and $\mathcal{W}_{\text{ea}}$ becomes

$$\lim_{\epsilon\to 0}\mathcal{W}_{\text{ea}}(t_0,t_f)=\mathcal{F}\left(y,x(t_0)\right)+P_0^{-1}. \tag{6.30}$$

6.5 Augmented observability-based path planning

This section discusses the use of the empirical augmented unobservability index (6.16) for path planning. It compares the method to other path planning strategies and concludes with an experiment showing that planning according to the novel index (6.16) yields the desired autonomous behavior in the presence of Gaussian prior uncertainty.

6.5.1 Distinctions in path-planning strategies

Previous adaptive-sampling works (e.g., Bishop *et al.* [30] and Davis *et al.* [31]) have analyzed the anticipated reduction in error covariance as a relevant quantity for planning of adaptive sampling in the presence of prior information (conversely, existing uncertainty). Anticipated error covariance analysis is similar in the case of a linear deterministic model to augmented observability. In the nonlinear case, the approaches differ because the anticipated reduction in covariance approach depends on the estimation scheme. We define empirical augmented observability independently of the estimator; it includes only the system dynamics, output equations, and the background error covariance.

The optimal inverse covariance (6.18) is a transformed version of the augmented observability. Alternately, write (6.18) by factoring out an inverse, i.e.,

$$P(t_f) = \Phi(t_f, t_0)\mathcal{W}_{\text{ao}}^{-1}(t_0, t_f)\Phi^T(t_f, t_0). \tag{6.31}$$

Since a covariance matrix P transforms under dynamics from t_1 to t_2 according to $P(t_2) =$

$\Phi(t_2, t_1)P(t_1)\Phi^T(t_2, t_1)$ [100], the filtering covariance $P(t_f)$ at time t is related to the inverse of the augmented observability $\mathcal{W}_{\text{ao}}^{-1}(t_0, t_f)$ by propagation under the dynamics. Equation (6.31) highlights the differences between path planning strategies in the linear case. Planning based on $\mathcal{W}_{\text{so}}$ alone does not account for prior covariance P_0. Planning based on the augmented observability Gramian $\mathcal{W}_{\text{ao}}$ accounts for both $\mathcal{W}_{\text{so}}$ and P_0, but still differs from filtering-covariance planning by the additional transformation of the dynamics.

These distinctions lead to the following interpretations of the strategies: (i) planning based on $\mathcal{W}_{\text{so}}$ is equivalent to selecting the candidate path that results in highest observability for the time interval $[t_0, t_f]$; (ii) planning based on $P(t_f)$ selects the candidate path that results in the most certainty in the antipicated posterior covariance at time t_f; (iii) planning based on $\mathcal{W}_{\text{ao}}$ selects the candidate path with observability that is the most complementary to information in the prior inverse covariance P_0^{-1} at time t_0. Planning based on $\mathcal{W}_{\text{ao}}$ and $P(t_f)$ are not guaranteed to yield the same results since the transformation by the dynamics in (6.31) may affect the eigenvalues of the $\mathcal{W}_{\text{ao}}$. However, three practical advantages of planning with $\mathcal{W}_{\text{ao}}$ instead of $P(t_f)$ are (i) since the true state and flow-field parameters are not known for a flow estimation application, propagation of $\mathcal{W}_{\text{ao}}$ may not lead to a reliable anticipated posterior covariance; (ii) for nonlinear dynamics, the anticipated posterior probability density function may be multimodal and not well represented by $P(t_f)$; and (iii) the influence on path selection of the prior information encoded within P_0 may be easier to interpret since P_0 does not receive additional transformation.

6.5.2 Experiment in automated turn selection using augmented empirical observability

Consider again the two-vortex system and the routes shown in Figure 6.1. Route A reflected about both the real and imaginary axes yields Route B. Over the time interval $[T_h, 2T_h]$, Routes A and B yield identical ν indices of 8.444, whereas Route C has a ν index of 27.50. Now consider the 3×3 block submatrices in $\mathcal{W}_{\mathrm{eo}}(T_h, 2T_h)$ corresponding to the vortex states. Table 6.2 provides the ν indices for the vortex submatrices for each route. Route A and Route B yield identical yet interchanged values. Traversing Route A around Vortex 1 provides more observability of Vortex 1 than Vortex 2, and traversing Route B around Vortex 2 provides more observability of Vortex 2 than Vortex 1. Route C is more complex, because it provides more observability of Vortex 1 even though it departs from Vortex 1 and begins to encircle Vortex 2.

Table 6.2: Unobservability analysis of vortex states only for Routes A–C

Time span: $[T_h, 2T_h]$		
Route	Unobs., Vortex 1	Unobs., Vortex 2
A	0.2631	0.5933
B	0.5933	0.2631
C	0.1430	2.6468

The following numerical experiment illustrates the use of the empirical augmented observability for path planning. At time $t = T_h$, assume the vehicle has no prior observability information, but has a prior covariance $P_0 = \mathrm{diag}(\alpha\,\mathbb{I}_{3\times3}, \beta\,\mathbb{I}_{3\times3}, 0.001\,\mathbb{I}_{2\times2})$. That is, the vehicle knows its position with relative certainty and it has $\alpha, \beta \in \mathbb{R}^+$ multipliers for diagonal covariances on the states of Vortices 1 and 2, respectively. If $\alpha > \beta$, then the vehicle has more initial uncertainty about Vortex 1 as compared to Vortex 2, and vice versa. For the planning interval $[T_h, 2T_h]$, the vehicle chooses a route using the augmented observability index ν_a. For ease of interpretation of the results, first consider the case in which the vehicle may impulsively switch to Route B. Define the quantity

$$\frac{\nu_{a,j} - \nu_{a,A}}{\max\left(\nu_{a,A}, \nu_{a,j}\right)} \tag{6.32}$$

for Routes $j = B, C$ as a measure of turn confidence. When $\nu_{a,j} > \nu_{a,A}$, turn confidence is positive and the vehicle should remain on Route A. When $\nu_{a,j} < \nu_{a,A}$, the vehicle should switch to Route j for $j = B, C$. The denominator maps the quantity to the interval $[-1, 1]$.

Figures 6.2(a) and 6.2(b) show the results of numerically altering the α and β prior variances. For large, uncertain α or β values, the prior covariance term determines the turn selection in Figure 6.2(a), and the vehicle appropriately selects the route that explores the more uncertain vortex. In Figure 6.2(b), the behavior is more complex due to the observability results associated with this route in Table 6.2. Route C provides more observability of Vortex 1 relative to Vortex 2, and it also provides more observability of Vortex 1 than Route A does. Route A provides more observability of Vortex 2 than Route C. Correspondingly, turn selections in Figure 6.2(b) have reversed. Also note that Figure 6.2(b) displays a region where the diagonal decision boundary bends. In this region, α and β are large and uncertain, so the vehicle's decision defaults to the observability analysis without prior information in Table 6.1; Route A is selected because it is more observable

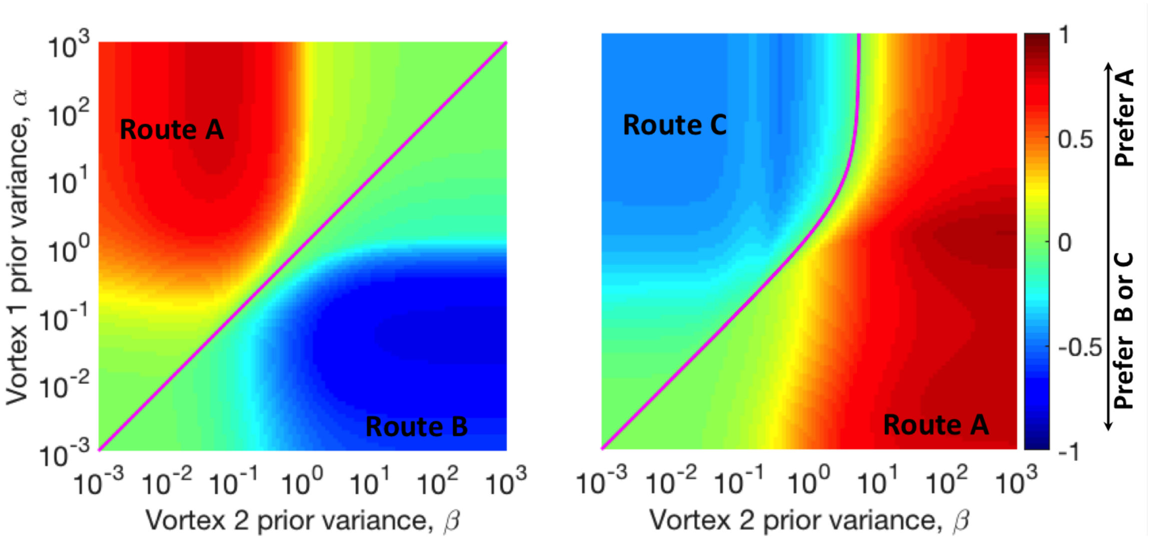

(a)

(b)

Figure 6.2: Turn confidence in selecting either (a) Route A or Route B, or (b) Route A or Route C, for a 100 × 100 grid of α and β values. Decision boundaries where $\nu_{a,j} = \nu_{a,A}$ are shown as magenta lines.

than Route C. These experiments suggest that the augmented unobservability index yields a criterion for automated path selection that coincides with intuitive use of observability in a manner that complements the prior information of the background error covariance P_0. This example demonstrates that augmenting observability with prior information improves sampling by changing the optimal path in an intuitive manner.

6.6 Augmented observability-based path planning with non-Gaussian densities

The previous sections develop augmented observability in the presence of Gaussian prior uncertainty. This section extends augmented observability-based path planning to the case of non-Gaussian prior uncertainty.

Assume that the prior pdf $p(x)$ may be well approximated by the Gaussian mixture model (3.10). Given a GMM $p(x) = \sum_{m=1}^{M} w_m \mathcal{N}\left(x; \underline{x}_m, P_m\right)$, one may generate a random sample from the pdf by selecting Gaussian m with probability w_m and subsequently sampling from Gaussian m using standard methods for random sampling of a multivariate normal distribution (e.g., see [85]). This interpretation of a Gaussian mixture model as the sum of disjoint probabilities that x is distributed according to Gaussian m motivates the selection of $\{\underline{x}_m\}_{m=1}^{M}$ for a sampling of the GMM with weights $\hat{w}_j = w_m$. That is, select each component Gaussian with probability w_m and represent each component Gaussian by its mean to generate a sparse, approximate representation of the prior pdf. Choosing the component modes of a GMM as a sparse pdf sampling is natural because each mode is associated with an accumulation of probability mass, by construction of the mixture. Indeed, only the means, covariances, and weights of a Gaussian mixture are needed to perfectly recover the first and second moments of the overall pdf (see for example (3.13) and (3.14)).

Denote a list of candidate control signals (perhaps generated by another control policy or other means) by $\{u_j(\cdot)\}_{j=1}^{K}$, where K is the total number to be evaluated. For each control signal, calculate an empirical augmented unobservability index $\nu_a(\mathcal{W}_{\text{ea}}(t_0, t_f, \underline{x}_m, P_m, u_j))$ for each component m in the GMM using the mean $\underline{x}_m$ and covariance P_m. Then, an approximate expected cost J_{ν_a} in augmented unobservability index for a prescribed control

u_j may be found by summing over all components in the mixture

$$J_{\nu_a}(u_j) \approx \sum_{m=1}^{M} w_m \nu_a(\mathcal{W}_{ea}(t_0, t, \underline{x}_m, P_m, u_j)). \tag{6.33}$$

Equation 6.33 defines the expected cost in augmented unobservability that the vehicle pays if it decides to implement control signal u_j. The expected cost is a weighted sum of the augmented unobservability indices over all mixture components. Note that this calculation includes evaluating the candidate control u_j over all state realizations $\underline{x}_m$ for $m = 1, \ldots, M$. If control u_j was generated assuming that a realization $\underline{x}_p$ represented the truth, then these calculations correspond to implementation of the selected control across all state realizations, $\underline{x}_m$ for $m = 1, \ldots, M$, even those that were assumed to be incorrect during the control's construction (i.e., for $m \neq p$). One may then compare the expected cost in augmented unobservability across all candidate control inputs and select the minimizer.

Chapter 7

Application II: Adaptive Lagrangian sampling of a two-vortex flow field

The flow measurements of ocean-sampling vehicles are often their Lagrangian data, i.e., measurements of the vehicle position under the influence of the flow. Sensor platforms like gliders are minimally actuated to extend endurance; planning efficient, feasible, and informative routes is therefore essential. A comprehensive path planning framework for guiding Lagrangian sensors for maximal observability of the underlying flow field is still needed.

This chapter focuses on the development of an autonomous estimation and control framework to enable a Lagrangian sampling vehicle capable of steering and flow-relative propulsion to estimate a potential-flow field with unknown parameters. The adaptive-sampling architecture guides a hypothetical oceanographic vehicle along paths of high flow-field observability. High observability of flow-field parameters is obtained from sampling trajectories along the boundaries of invariant sets with close approaches to saddle points.

This chapter also utilizes augmented observability to account for uncertainty in the path-planning portion of a model-predictive control architecture.

The adaptive-sampling framework includes a model-predictive controller, known as the Augmented-Observability Planner (A-OP), that simulates candidate trajectories of the vehicle steering to invariant-set boundaries and selects the most informative one based on the empirical augmented unobservability index. Empirical augmented observability (developed in Chapter 6) is an extension of empirical observability to account for prior uncertainty of the system state in observability-based path planning. When non-Gaussian prior uncertainty is present, the A-OP performs augmented observability analysis using an approximate, expected cost calculation (see Section 6.6).

After selecting a trajectory, the vehicle collects Lagrangian measurements (i.e., measurements of its own position after accounting for control action) and assimilates these data in the GMKF, a nonlinear, non-Gaussian filter. The vehicle recursively improves its flow-field map using the posterior uncertainty and plans new vehicle paths for adaptive sampling. The performance of the flow-estimation framework is shown in an idealized model of an ocean eddy pair based on potential flow theory.

The nonstationary estimation problem of inferring the strengths and locations of two co-rotating vortices, which is pertinent to ocean sampling, provides a challenging test case for this framework. The periodic motion of two point vortices in relative equilibrium (e.g., rotating together at a constant rate) represents an idealized model of a naturally-occurring ocean eddy pair. Further, it is a demonstrative problem for studying autonomous navigation, because when viewed from a co-rotating frame, this system contains invariant sets that can be used to study the role of coherent structures in navigation and flow-field estimation.

7.1 Framework for adaptive Lagrangian sampling

This section presents a novel architecture for guided-Lagrangian adaptive sampling for nonlinear flow-field estimation that uses augmented observability-based path planning. Figure 7.1 shows the proposed framework for adaptive sampling and estimation of a flow field using a guided-Lagrangian sensor. This adaptive-sampling, estimation, and control loop consists of the true system dynamics (i.e., the ocean currents and vehicle dynamics), Lagrangian measurements of vehicle position, a nonlinear/non-Gaussian GMKF estimator, and the Augmented-Observability Planner with expected cost (A-OP).

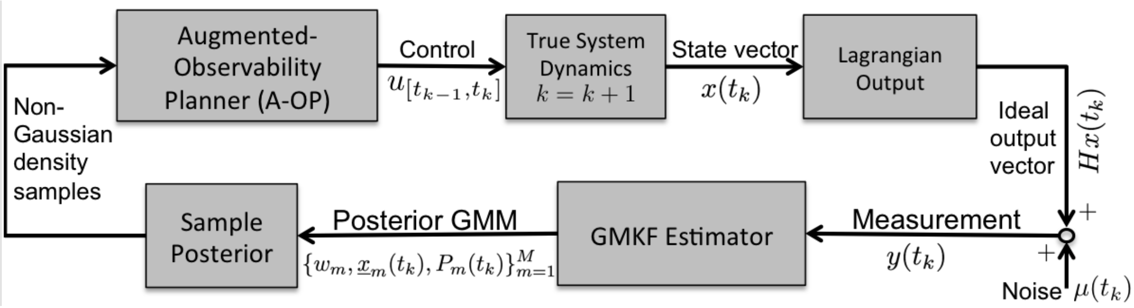

Figure 7.1: Adaptive-sampling, estimation, and control loop.

As presented in Chapter 3, the GMKF accommodates nonlinear dynamics and non-Gaussian probability densities by approximating them with a mixture of Gaussians selected to minimize the BIC, thereby yielding the simplest (based on the number of parameters) fit of a Gaussian mixture to the data [84]. The GMKF algorithm is well-suited for assimilation of Lagrangian data due to the linear observation operator present in such problems. The GMKF combines the measurement with a prior pdf in the form of a Gaussian mixture. The result of this non-Gaussian inference is a posterior pdf that encodes all uncertainty of the flow-field parameters and the vehicle state.

The A-OP is the other key component in this framework, because it encodes the augmented observability guidance strategy, making use of the posterior pdf for planning. An observability analysis requires an individual state estimate for the initial condition. An augmented-observability analysis requires an individual state estimate together with a covariance matrix, which characterizes the uncertainty. The GMKF is capable of non-Gaussian inference, and extracting a single estimate or statistic from the posterior pdf for use by the path planner does not fully utilize the pdf. We make additional use of the posterior density by extracting multiple state realizations (the GMM component modes with their associated covariances) for processing by the A-OP. An expected cost calculation as detailed in Section 6.6 enables the use of a multimodal posterior pdf for planning, rather than a single state estimate.

Figure 7.2 details the A-OP. At pre-determined intervals, the A-OP uses a parameterized model of the flow-field dynamics and calculates a flow-field map for each $\underline{x}_m$ and the associated invariant-set boundaries. The A-OP uses these target boundaries to generate candidate control inputs based on virtually steering to each nearby boundary using the hybrid steering controller from Chapter 5. The hybrid controller creates candidate trajectories by driving the vehicle along paths of high observability, which align with the separating boundaries of invariant sets. (Appendix B describes in detail how to construct

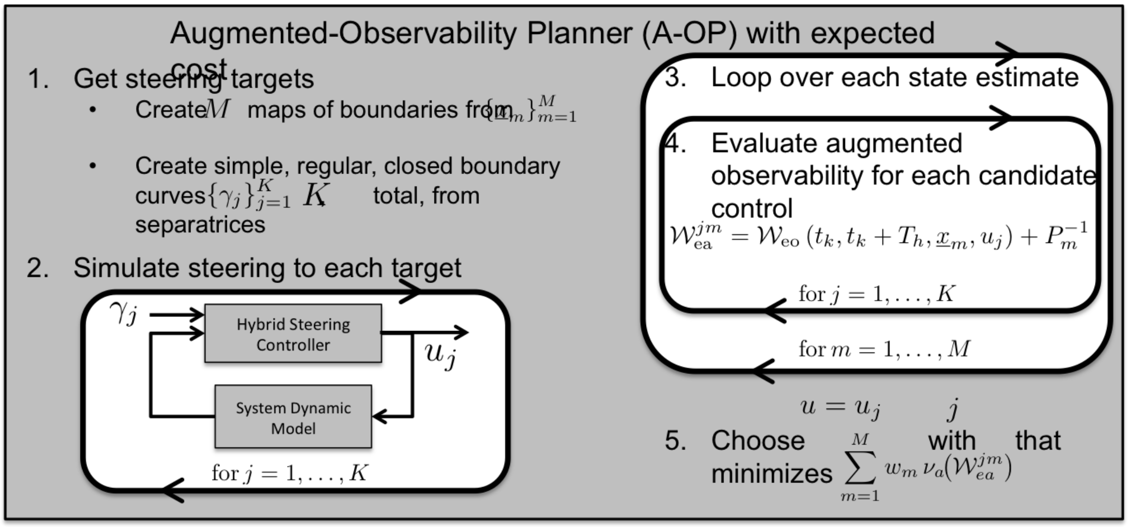

Figure 7.2: Augmented-Observability Planner (A-OP) with expected cost.

target curves for the hybrid steering controller and provides examples in the two-vortex system.) The A-OP subsequently assesses the candidate control signals using augmented observability analysis with approximate, expected cost and selects the most informative path.

The vehicle attempts to execute the planned trajectory until the next planning period by open-loop execution of the control signal u that corresponds with the intended vehicle trajectory. Position measurements of the vehicle are periodically taken and supplied to the GMKF. The GMKF assimilates Lagrangian data (after accounting for the vehicle's own control effort) to produce more informed estimates of the parameters, completing the estimation and control loop.

This framework is novel because it properly accounts for uncertainties in observability-based path planning by sharing state realizations and covariances between the estimation and planning sub-blocks. The shared samples are used in an approximate, expected cost calculation employed during the augmented observability analysis.

7.2 Adaptive Lagrangian sampling numerical experiments

This section presents numerical experiments necessary to demonstrate the efficacy of the proposed adaptive-sampling framework. First, this section presents the necessary formulae and transformations needed for these simulations. Second, it describes simulation setup, initial conditions, and example calculations of the closed-loop system. Third, it provides a comprehensive comparison of simulation cases in which various components of the framework (e.g., the non-Gaussian estimator, adaptive refinement of the flow-field map, augmented observability planning, and expected cost evaluation) are sequentially engaged.

7.2.1 Simulations in the two-vortex system

Chapter 2 presents the two-vortex system, including the necessary formulae and transformations for the inertial and co-rotating frames. (Chapter 2 presents the hybrid steering controller. Chapter 5 presents the flow-relative transformation that the hybrid steering controller utilizes.) Figure 7.3 provides a summary of all relevant reference frames, coordinates, and conversions needed for the numerical experiments of this chapter. The subscript R decorates quantities defined in the co-rotating frame. Coherent structures that are targets for the hybrid steering controller are visible in the co-rotating frame. The flow-relative control transformation allows calculation of a control that accounts for the influence of the flow in the co-rotating frame. The control signal is converted back to the inertial frame for simulation. All simulation and filtering calculations occur in the inertial frame.

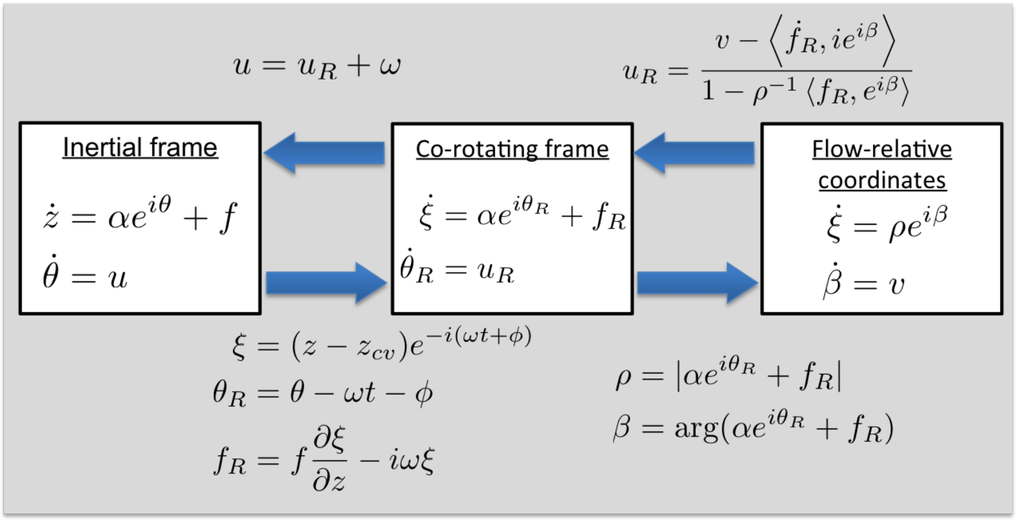

Figure 7.3: Diagram of reference frames, coordinates, and conversions for the two-vortex system with flow-relative steering control.

7.2.2 Experimental setup and example runs

Assume two vortices of fixed, but unequal strength. The vortices co-rotate about a conserved center of vorticity z_{cv} and have a conserved separation distance d. The locations and strengths of the vortices are estimated. Fix simulation parameters such as sampling frequency and duration, planning time constants, filter and controller gains, the initial estimate and uncertainty of the system state, and the vortex and vehicle parameters. Detailed information on parameter selection is in Appendix C. Large variances in the initial condition estimates for vortex circulation strength and position represent large uncertainty in the initial state estimate. These choices challenge the GMKF to perform proficiently in estimating the system state from uncertain initial conditions.

The GMKF converges over a wide range of initial conditions, however, convergence is not guaranteed for arbitrary initial conditions (e.g., if the initial vortex estimates are far from accurate or if a drifting vehicle is launched in a region of low observability). To demonstrate robustly the performance benefits of this framework, we perform Monte Carlo simulations from random initial conditions throughout the initial-condition sample space. The initial conditions of primary importance are the vehicle launch location and orientation as well as the phase of vortex rotation relative to the vehicle initial position. We sample 100 vehicle positions uniformly from a 3×3 square-unit area in the domain of interest. The vehicle initial orientation and the true initial phase of rotation for the vortices are sampled uniformly from the interval $[0, 2\pi]$. Figure 7.4 shows the initial vehicle locations and orientations for the simulations. It also shows the initial estimate of the vortex locations and the associated separatrices in green. For clarity, only one realization of the true-vortex locations is shown; other realizations are rotations about the same center of vorticity.

Figures 7.5(a)–7.5(f) are three representative test cases for a single initial condition that is one of the random initial conditions in Figure 7.4. The co-rotating frame in Figures 7.5(a), 7.5(c), and 7.5(e) is based on the true vortex-pair rotation rate ω. Figures 7.5(b), 7.5(d), and 7.5(f) show the inertial frame and Lagrangian measurements that the vehicle uses to estimate the flow-field parameters. Figures 7.5(a) and 7.5(b) show the trajectory of a drifting vehicle in the true co-rotating frame and the inertial frame, respectively. In the inertial frame, the vehicle traces out a near-circular trajectory that precesses around the

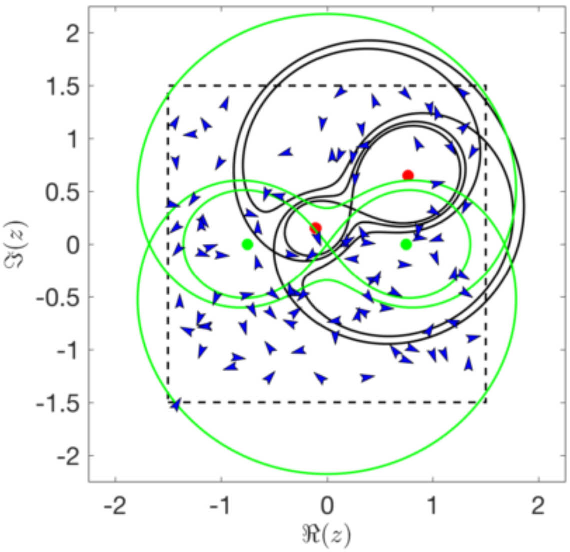

Figure 7.4: Initial conditions used in numerical experiments; arrow heads are initial vehicle locations and orientations; initial conditions of the vortices and their separatrices are shown in green (estimated) and black (truth).

vortices. In the co-rotating frame, the vehicle remains on a closed streamline, confined to the outermost invariant set. This launch location yields a rather unobservable trajectory since the motion the drifter in the outermost invariant set closely resembles the motion that results from many other vortex-pair realizations. Figures 7.5(c) and 7.5(d) show a self-propelled vehicle with a planner that knows the true flow-field parameters navigating along boundary paths to minimize the unobservability index over a forward-looking time horizon. Only results from the time interval $[0, 2.5]$ are shown for clarity. Magenta diamonds denote planning times. Note that the trajectory in the co-rotating frame explores the invariant-set boundaries, without specification of navigation targets *a priori*. In the inertial frame, the path contains spirographic segments corresponding to the vehicle navigation around the innermost invariant sets. Portions of the inertial trajectory also appear more jagged as the vehicle changes course at planning times to follow a more observable route.

Figures 7.5(e) and 7.5(f) show an example run of the full closed-loop, adaptive Lagrangian sampling framework over the time interval $[0, 2.5]$ (shortened for clarity). Neither the planner nor the estimator know the flow-field parameters; the vehicle uses feedback control to adapt the flow-field map according to Lagrangian measurements. The path of the vehicle in the true co-rotating frame does not clearly navigate along boundary curves. However, each trajectory segment between planning times does in fact steer towards separating boundaries if viewed in the co-rotating frame of the instantaneous state estimate; the resulting trajectory is the accumulation of navigation choices that minimize the expected augmented unobservability index over the candidate control signals and flow-field maps that the vehicle evaluates. As the state estimate improves later in the simulation, the vehicle navigates more closely along the true separating boundaries, similar to Figure 7.5(c).

Figure 7.6 displays the GMKF estimation results that correspond to the run in Figures 7.5(e) and 7.5(f) for the full closed-loop system. The GMKF automatically selects the necessary number of Gaussians for the GMM in the forecast pdf prior to each data-assimilation step. Figures 7.6(a) to 7.6(f) show time histories of the marginalized pdfs for the vortex states. White lines represent the true state trajectory. From incorrect and uncertain initial estimates with large variances, the closed-loop system effectively identifies and tracks the two-unequal vortices. Although each of the marginalized pdfs for vortex strength appear to be close to Gaussian at any given point in time, non-Gaussianity is clearly evident in the marginalized pdfs for vortex location in Figures 7.6(c)–7.6(f), highlighting the importance of using a non-Gaussian filter in this application.

In many trial runs, the GMKF converged to a trajectory in which the Vortex 1 estimate agreed with the Vortex 2 true state and vice versa. This condition is not problematic because the system dynamics are invariant to an exchange of the vortex labels. After simulation, the minimum of the estimation error between the two labeling conventions reveals which labeling convention the estimator selects for each run. Prior to calculation of the data in Table 7.2, vortex labels were adjusted to best match the results of the estimator.

7.2.3 Test of performance gains

Eight cases in Table 7.1 test for performance gains from each feature of the sampling framework. The selected options indicate the realization of the framework components for each case. For each case, 100 Monte Carlo simulations were performed using the initial conditions provided in Figure 7.4. Table 7.2 contains a bar graph of the estimation error results, averaged over all simulation trials for a particular case and normalized by the mean of Case 8, an idealized case. Error bars represent one standard deviation from the mean.

Case 1 represents a drifting vehicle using an EnKF estimator; this case is similar to many experiments currently performed in practice (e.g., see [53]). Case 2 also contains a drifting vehicle, however the GMKF is used for estimation. The large reduction in estimation error achieved by Case 2 in comparison to Case 1 shows the benefit the GMKF over an EnKF. Examination of individual runs for Case 1 reveals that often the estimator fails to identify the system accurately for the range of parameters considered. More

Table 7.1: Matrix of numerical experiments in adaptive Lagrangian sampling

Cases	Planning & Control						Estimation	
	Off	On					EnKF	GMKF
		Non-adaptive	Adaptive					
		Single Estimate	Single Estimate		Expected Cost			
		Forward Obs.	Forward Obs.	Aug. Obs.	Forward Obs.	Aug. Obs.		
1	X						X	
2	X							X
3		X						X
4			X					X
5				X				X
6					X			X
7						X		X
8*		X						X

* Flow known by the planner but not by the estimator

Table 7.2: Table of results for numerical experiments in adaptive Lagrangian sampling

Cases	Results
	Estimation error averaged over 100 trials $\sum_k \|\underline{x}(t_k) - x^{\text{true}}(t_k)\|_2$ (nondimensional, $\times 10^3$, normalized by Case 8)
1	2.95
2	1.52
3	1.49
4	1.31
5	1.26
6	1.03
7	1.02
8*	1.00

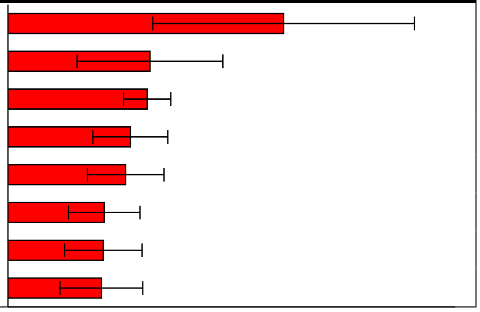

* Flow known by the planner but not by the estimator

sophisticated constructions of the EnKF algorithm exist that include features such as covariance localization and covariance inflation [112] that could improve the performance of the EnKF in these simulations. However, we implement a basic form of the EnKF for direct comparison to the GMKF, for which the only change is an increased capacity of $M \geq 1$ Gaussians.

Cases 3–7 perform adaptive sampling based on an estimated map of the flow field. Case 3 uses a self-propelled vehicle with an observability-based planner that considers empirical observability calculated forward-in-time and based on the mean estimate extracted from the Gaussian mixture pdf. The map of the flow field used for generating candidate control signals is based on the initial estimate of the system only and does not update at later times (i.e., the vehicle does not adapt its map to new state estimates). Case 3 shows a benefit of self propulsion in flow-field estimation as it outperforms Case 2. Cases 4–7 show that alternate navigation of a self-propelled vehicle can achieve better estimation. The use of a non-adaptive flow-field map in Case 3 steers the vehicle towards invariant-set boundaries in its flow-field map, which may actually correspond to less observable paths in the true flow-field map, since the initial estimate is incorrect. This case highlights the need for a self-propelled vehicle to be appropriately guided. Note that the variance in estimation results is the smallest for Case 3, which is attributable to the use of a non-adaptive flow-field map.

Case 4 contains a planner that makes sampling decisions based on forward-looking observability analysis, similar to Case 3. However, Case 4 adapts its flow-field map based on the overall mean estimate of the posterior pdf after each estimation cycle. Case 4 demonstrates a large improvement over Case 3 in estimation performance. Case 5 also plans adaptively using the mean estimate of the posterior pdf, but it performs an augmented observability analysis based on the overall mean estimate and the overall covariance matrix for the posterior pdf. For the parameter values selected, augmented observability-based path planning in Case 5 yields better estimation performance than forward-looking observability-based path planning in Case 4. This finding extends the results of [66], which did not perform estimation using a closed-loop, adaptive-sampling setup. Note that although the posterior pdf may be multimodal, Cases 3 and 4 only use the mean of the pdf, and Case 5 only uses the mean and covariance. Use of a single estimate from the posterior pdf does not fully utilize the information present in the pdf, but it is consistent with traditional output-feedback control.

The approximate expected-cost calculation for planning in the presence a posterior pdf represented by a Gaussian mixture model allows the planner to use more than a single estimate from the posterior pdf. Case 6 adaptively plans using multiple samples, the component modes, from the posterior pdf. For each sample, the planner generates an individual flow-field map, creates candidate control inputs using the hybrid steering controller, and completes an approximate expected-cost calculation for the unobservability indices for a forward-in-time observability analysis. Relative to Cases 4 and 5, Case 6 shows an improvement that highlights the benefit of an expected cost analysis. Case 7 utilizes the complete framework for augmented-observability path planning with approximate expected cost. Case 7 performs an approximate expected-cost calculation of the augmented unobservability index for multiple state realizations, whereas Case 6 uses the unobservability index without augmentation. Case 7 offers a slight improvement estimation error over Case 6. Note that the improvement is not as large as the improvement of Case 5 relative to Case 4. The expected cost calculation of Case 6 inherently includes additional prior information from the posterior pdf through its use of multiple samples, so the improvement from Case 6 to Case 7 is present but less substantial.

The planner in Case 8 knows the true flow-field parameters, whereas the estimator does not. This case represents a vehicle that knows the most observable regions of the flow field for sampling. The average estimation error for this case is the smallest of all cases. Note that the cumulative benefits of the adaptive-sampling framework cause the average estimation error of Case 7 to closely approach the best-case error in Case 8.

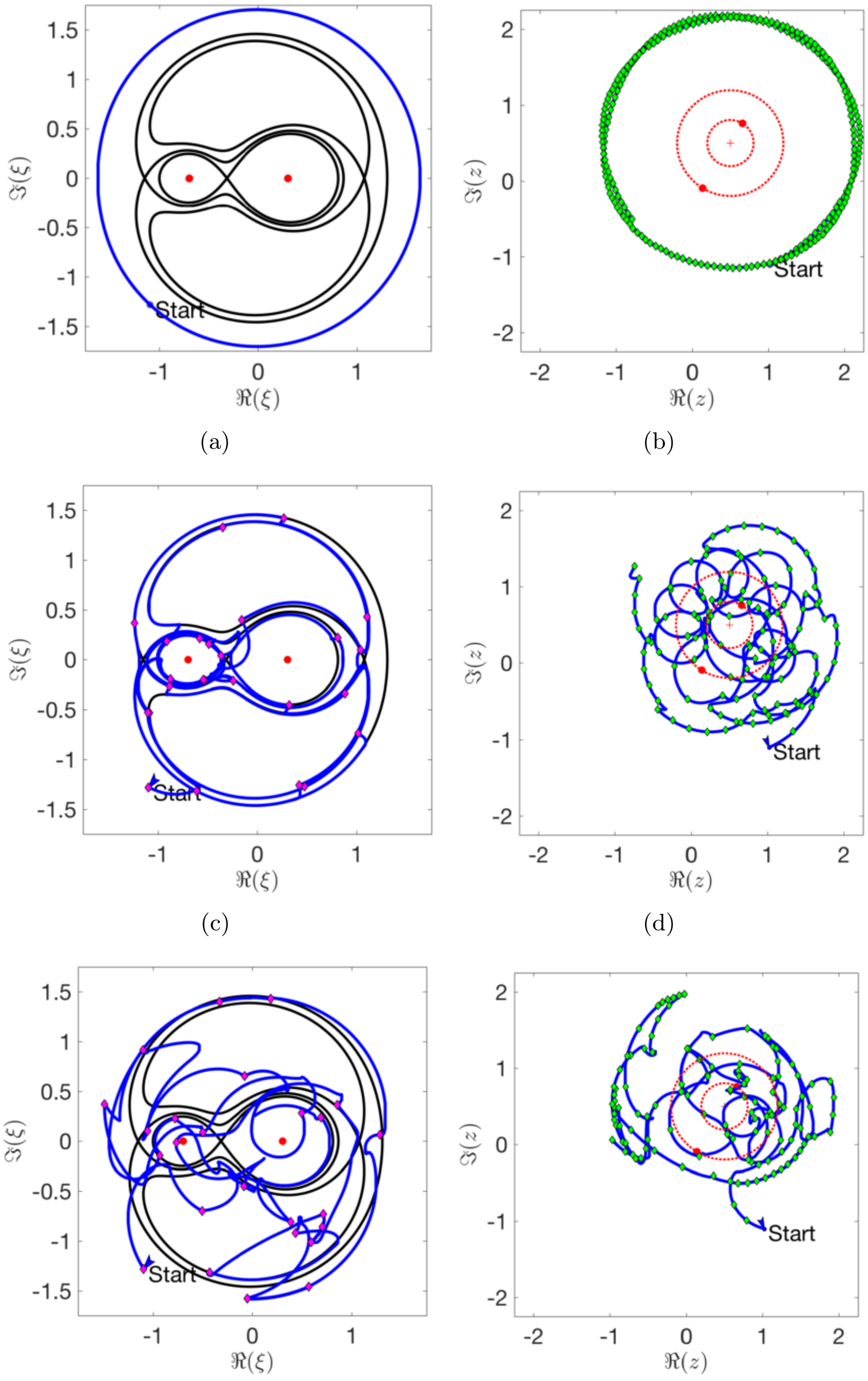

(a) (b)

(c) (d)

(e) (f)

Figure 7.5: Vehicle trajectories in the true co-rotating (a,c,e) and inertial (b,d,f) frames for a drifting vehicle (a and b) over time interval $[0, 5]$, an observability-guided vehicle with a known flow-field map (c and d) over time interval $[0, 2.5]$ (shortened for clarity), and a vehicle navigating according to the A-OP with an estimated flow-field map (e and f) over time interval $[0, 2.5]$ (shortened for clarity); green diamonds are measurement-time markers; magenta diamonds are planning-time markers; red lines record the paths of the vortices.

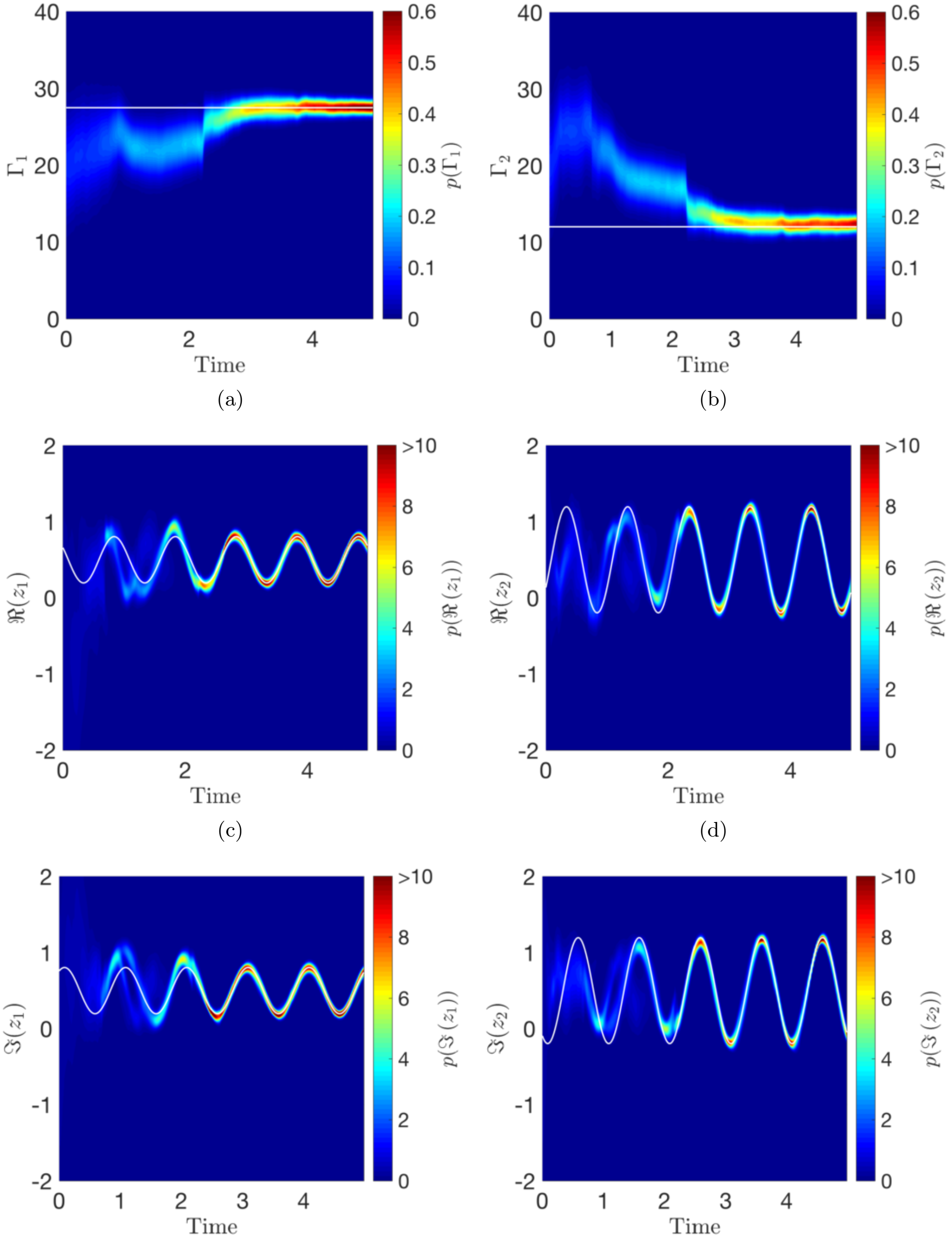

(a) (b) (c) (d) (e) (f)

Figure 7.6: Estimation results for the closed-loop sampling framework. a)-f) Time histories of the marginalized pdfs for the vortex states.

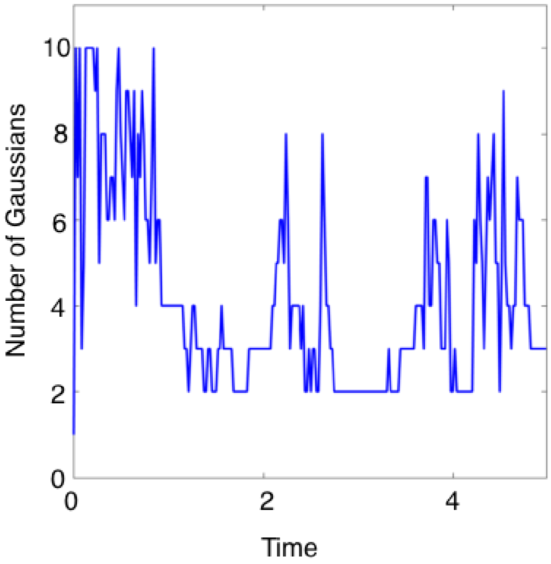

Figure 7.7: Time history of the number of Gaussian components used by the GMKF.

Chapter 8

Conclusion

This chapter reviews the primary contributions of this dissertation in detail and provides suggestions for future research.

8.1 Summary of contributions

This dissertation addresses the problem of autonomous flow sensing by mobile robotic platforms in challenging fluid flows. The dissertation specifically divides the range of applications into two classes: vehicle-scale flow-sensing problems, and long-range flow-sensing problems. Vehicle-scale flow-sensing problems require rapid understanding of the flow field, as a primary objective may be vehicle stabilization. Long-range flow-sensing problems have the distinctions that additional time is available for deliberative path planning and often a global picture of the fluid environment is sought.

Common tools may be utilized for both classes of problems, including observability-based sensor placement and routing, nonlinear/non-Gaussian estimation, and output feedback control. For two specific applications, rheotaxis of a robotic fish and adaptive Lagrangian sampling for flow-field monitoring, this dissertation provides estimation and control frameworks that successfully accomplish their respective objectives. In the framework for long-range path planning using observability, it is necessary to address the question of how to choose informative vehicle paths using both a forward-looking observability analysis and prior information from previous estimation cycles. The answer to this question is a novel path planning index: the empirical augmented unobservability index.

8.1.1 Output-feedback control for rheotaxis of robotic fish

Understanding the flow around a fish-like body is essential for robotic fish applications. Rheotaxis of a robotic fish is a vehicle-scale flow-sensing application in Chapter 4 that involves estimation of the flow field and subsequent control action to achieve the desired upstream orientation. To accomplish this task, Section 4.1 employs a fluid-mechanical model for flow around a robotic fish based on potential-flow theory and provides estimates of both the fish's orientation and the free-stream flow speed. Pressure-difference measurements are inspired by the canal neuromast sensing modality in fish. The pressure differences also permit elimination of a flow-specific constant in Bernoulli's equation. Using the fluid-mechanical model, Section 4.2 places pressure sensors on the fish body based on an empirical observability analysis. Section 4.3 describes our experimental test bed, and Section 4.4 evaluates the validity of the potential flow model using the test bed and CFD calculations.

Section 4.5 presents a feedback controller based on the difference between pressure measurements collected on opposite sides of the robotic fish. It also describes a dynamic rheotaxis controller based on a potential-flow model and a Bayesian filter that uses two or more pressure sensors in an arbitrary, distributed arrangement. Experimental results show the dynamic rheotaxis controller reliably achieves rheotaxis despite model error and sensor noise, while providing accurate flow-speed estimates. The estimation-control framework produces a dynamic controller that is less sensitive to noise than a pressure-difference controller and is able to achieve rheotaxis from an initial orientation outside the accurate domain of the potential-flow model. This framework also generalizes to arbitrary sensor placement. The primary contribution of Chapter 4 is a framework for rheotaxis and flow-speed estimation based on pressure-difference information that does not require fitting model parameters to flow-field conditions. The contributions of this chapter are significant because rheotaxis and flow speed estimation can be achieved without fitting parameters empirically. The pressure-difference measurement equation proposed in Chapter 4 has been subsequently used in [23, 25, 72, 113].

Limitations of this rheotaxis approach include: reliance on reduced model error in the zero angle-of-attack orientation, causing reduced performance for orientation control to a non-zero angle of attack; and reliance on a relatively uniform flow. Improvement of the estimator performance for angle of attack through implementation of a higher fidelity model may enable orientation control to a nonzero angle.

8.1.2 Observability-based guidance, navigation, and control in planar flows

To incorporate observability tools into long-range flow-sensing applications, Chapter 5 uses observability-based path planning, in which an optimal-control signal is selected from a finite set based on an evaluation of how much observability the candidate signals provide of the underlying flow field, as measured by the unobservability index. We also utilize observability tools to assess of the most informative regions of the flow to sample using Lagrangian position measurements. By considering the empirical observability of drifting orbits, Section 5.1 concludes that the most observable paths closely follow the separating boundaries of invariant sets, making close approaches to saddle points.

Using the most observable streamlines as steering targets, Section 5.2 develops a hybrid steering controller. The hybrid steering controller includes a streamline controller and a stream-function-value controller. The streamline controller is a novel combination of a flow-relative transformation and a steering control built around a Bertrand family of curves to steer to a unique, closed streamline of the flow. Theorem 2 analytically establishes the region of validity for the streamline controller. The stream-function-value controller guides the vehicle to within the valid region of the streamline controller.

The primary contributions of Chapter 5 are the identification of invariant-set boundaries as highly observable to a Lagrangian sampling vehicle, and Theorem 2 regarding the region of validity of the streamline control law used in the hybrid steering controller.

8.1.3 Augmented observability-based path planning

In using observability-based path planning for long-range flow-sensing applications, Section 6.1 shows that past vehicle history changes the optimal route selected. It is therefore necessary to develop a principled approach to performing observability-based path planning in the presence of prior information. Chapter 6 addresses this problem with augmented observability.

This chapter addresses automatic route selection in path planning for flow estimation by scoring candidate trajectories using a new measure called the empirical augmented unobservability index. This measure includes a background error covariance as well as a forward-looking observability analysis. Section 6.3 defines augmented observability by drawing insight from the continuous-time reduced Hessian in Incremental 4D-Var data assimilation. Section 6.3 also derives the optimal inverse posterior covariance for a continuous-time Kalman Filter with deterministic dynamics. Section 6.4 compares augmented observability to the optimal, anticipated inverse covariance for a linear, deterministic continuous-time system with measurement noise, and it highlights distinctions between path-planning strategies.

Augmented observability can be extended to the nonlinear setting using empirical observability, yielding the empirical augmented unobservability index. Using numerical experiments, Section 6.5 shows that path planning based on this novel index yields the desired behavior for a guided Lagrangian sensor performing turn selection in a two-vortex flow field in the presence of prior information. Section 6.6 concludes the chapter by suggesting how augmented observability-based path planning may be extended to non-Gaussian prior densities through the use of a mixture of Gaussians and an approximate expected-cost calculation. The primary contributions of Chapter 6 are the derivation and definition of augmented observability, as well as the construction of the empirical augmented unobservability index for path planning.

8.1.4 Adaptive Lagrangian sampling of a two-vortex flow field

Chapter 7 presents a principled approach to estimate the parameters of a two-vortex flow that models a double-eddy system in the ocean. The adaptive Lagrangian sampling framework guides a self-propelled Lagrangian sensor along highly observable paths. The main components of the framework are a hybrid steering controller guided to invariant-set boundaries, the Gaussian Mixture Kalman Filter, and the Augmented-Observability Planner with approximate expected cost.

Section 7.1 builds the adaptive Lagrangian sampling framework and describes the functions and interactions of its subcomponents. The Gaussian Mixture Kalman Filter is a dynamic nonlinear filter that produces a non-Gaussian posterior distribution capturing the uncertainty in the state of the system in the form of a Gaussian mixture model. From the Gaussian mixture model, the Augmented-Observability Planner considers the component means and their covariances as possible state realizations and associated uncertainties. For each candidate realization, the Augmented-Observability Planner generates a family of candidate control signals constructed using the hybrid steering controller and the estimated flow-field map. The Augmented-Observability Planner evaluates the augmented unobservability index, a measure of the complementarity of a forward-looking observability analysis with a prior background error covariance, for all control signals and all candidate state realizations. The Augmented-Observability Planner performs an approximate expected cost calculation by taking a weighted sum of the augmented unobservability indices according to the component weights from the Gaussian mixture model.

The Augmented-Observability Planner then selects the minimizing control signal across all candidate control signals. The resulting control signal minimizes the empirical augmented unobservability index weighted across possible state realizations; hence, this control signal provides the most informative vehicle trajectory given prior information and other possible state realizations.

Section 7.2 provides numerical experiments showing the benefit of this adaptive sampling framework in a two-vortex flow field. The primary contribution of Chapter 7 is the adaptive Lagrangian sampling framework built around a nonlinear/non-Gaussian estimator and the augmented observability tools of Chapter 6.

8.2 Suggestions for future research

8.2.1 Vehicle-scale flow sensing and control

Dealing with complex vehicle-scale flow interactions presents many questions still open to investigation and further development. Work is needed to perform increasingly complex flow estimation using time-varying flows, flows for which a stream function must be approximated, and flows for which a parameterized flow model is not known *a priori*. Data-driven approaches for construction of reduced-order flow models, such as dynamic mode decomposition [114], offer rich possibilities for high-fidelity flow-field estimation that surpasses the potential-flow based flow models used in the application problems of this dissertation. Data-driven approaches have the potential to represent flow effects such as viscous effects and turbulence that are not captured in the above modeling approaches.

Further, these reduced-order, data-driven models may still allow for rapid computation that may be implemented on-board the vehicle.

One important estimation question in flow sensing that needs to be addressed is how to identify structures in the flow field or flow-field characteristics that are pertinent to the vehicle dynamics and the desired trajectory. Not all aspects of the infinite dimensional surrounding fluid flow are important, and some can and must be neglected for computational efficiency. Additionally, some flow aspects may dictate the features of a reduced-order model, leading to the question of model selection as a preliminary step preceeding detailed flow estimation. Future work should address how and when to engage one of a family of reduced-order models in flow estimation by a flow-sensing vehicle.

8.2.2 Long-range flow sensing and control

This dissertation addresses long-range flow sensing for an ocean-sampling application with a single guided, Lagrangian position sensor. Future work is needed to extend this research to multiple, cooperative sampling agents. Existing research has looked at distributed estimation and control [36, 115–119] for environmental estimation. However, these approaches have not been observability-based or augmented observability-based. Chapter 6 made connections between empirical observability and information theory. From this discussion it is apparent that further connections may be possible. Specifically, it would be useful to strengthen the connections between information-theoretic adaptive sampling approaches (e.g., [120]) and the augmented observability-based approach.

Augmented observability addresses prior information as well as measurement uncertainty. However, it does not address randomness that enters through process noise. Future research is needed to address the inclusion of stochastic forcing in the dynamics and to assess its impact on augmented observability-based path planning.

Appendix A

Complex-variable mathematics

This appendix provides all necessary background material for handling the functions of complex variables that appear in this dissertation. Section A.1 describes the correspondence between the $\mathbb{C}$ plane and the $\mathbb{R}^2$ plane. It also reviews complex notation and some fundamentals. Section A.2 is a collection of complex identities useful in manipulations.

A.1 The $\mathbb{C} - \mathbb{R}^2$ correspondence

A useful and notationally compact way to represent a planar vector in $\mathbb{R}^2$ is through its direct correspondence to a complex value in the $\mathbb{C}$ plane. Let $(x, y)^T$ be a vector in $\mathbb{R}^2$. The corresponding value in the $\mathbb{C}$ plane is

$$z = x + iy,$$

where $i = \sqrt{-1}$ is the imaginary unit. Although this simplification may seem trivial, working with complex variables instead of vectors in $\mathbb{R}^2$ reduces vector equations to scalar equations over $\mathbb{C}$, in effect reducing the number of equations by one half. For example, the equation of a circle of radius r in $\mathbb{R}^2$ may be written parameterically as a function of an angle $\theta \in [0, 2\pi)$ as

$$\begin{bmatrix} x \\ y \end{bmatrix} = \begin{bmatrix} r\cos\theta \\ r\sin\theta \end{bmatrix}.$$

In complex notation, this equation becomes $z = r\cos\theta + ir\sin\theta$. Even more compactly, the use of Euler's identity,

$$e^{i\theta} = \cos\theta + i\sin\theta,$$

yields

$$z = re^{i\theta}.$$

Under the $\mathbb{C} - \mathbb{R}^2$ correspondence, a complex variable in $\mathbb{C}$ may represent either a point in the plane or a vector extending from the origin, analogous to the representation of a variable in $\mathbb{R}^2$. A vector in the complex plane may be represented with its *modulus* [121]

$$|z| = \sqrt{x^2 + y^2},$$

and with an angle measured counterclockwise from the positive real axis, called the *argument* $\arg(z)$, which satisfies [121]

$$\tan(\arg(z)) = \frac{y}{x}.$$

The *principle value* of $\arg(z)$ is the value satisfying the above relation and lying within $(-\pi, \pi]$.

The operators $\Re(\cdot)$ and $\Im(\cdot)$ extract the real and imaginary components of a complex number, respectively. Further, $\bar{(\cdot)}$ denotes complex conjugation, or mirroring of a complex number about the real axis, so that

$$\bar{z} = x - iy.$$

It is straightforward to show that for complex variables, the commutative, associative, and distributive relations hold similar to real-valued expressions [121]

$$z_1 + z_2 = z_2 + z_1$$

$$z_1 z_2 = z_2 z_1$$

$$(z_1 + z_2) + z_3 = z_1 + (z_2 + z_3)$$

$$(z_1 z_2) z_3 = z_1 (z_2 z_3)$$

$$z_1(z_2 + z_3) = z_1 z_2 + z_1 z_3.$$

One may accomplish division by multiplying top-and-bottom by the complex conjugate of the denominator, i.e.,

$$\frac{z_1}{z_2} = \frac{z_1 \bar{z}_2}{z_2 \bar{z}_2} = \frac{z_1 \bar{z}_2}{|z_2|^2},$$

where the numerator is the multiplication of two complex numbers, and the denominator becomes a real-valued scalar [121].

An inner product is a useful tool for quantifying the angular relation between two vectors. In this dissertation, the inner product for complex numbers is

$$\langle z_1, z_2 \rangle = \Re(\bar{z}_1 z_2). \tag{A.1}$$

One readily sees that this expression naturally agrees with the dot product of two vectors in $\mathbb{R}^2$ under the $\mathbb{C} - \mathbb{R}^2$ correspondence.

A function f of a complex variable z is denoted $f(z)$ if f depends on z only and not on $\bar{z}$. Treating z and $\bar{z}$ as separate variables, $f(z, \bar{z})$ denotes a function that depends on both z and $\bar{z}$.

Differentiation in complex is defined such that the function $f(z)$ is said to be differentiable at z if

$$\lim_{\xi \to z} \frac{f(\xi) - f(z)}{\xi - z}$$

exists for all directions of approach to the point z in the plane [121]. A function that has this property is called *analytic*, and we denote its derivative by df/dz. Let $u_x = \Re(f)$ and $u_y = \Im(f)$. Analytic functions are a very special class of complex-valued functions, because they possess the structure that their real and imaginary components evaluated at $z = x + iy$ satisfy [121]

$$\frac{\partial u_x}{\partial x} = \frac{\partial u_y}{\partial y} \quad \text{and} \quad \frac{\partial u_x}{\partial y} = -\frac{\partial u_y}{\partial x}, \tag{A.2}$$

which are known as the Cauchy-Riemann equations.

If a complex-valued function is not analytic (i.e., complex differentiable), we may still consider weaker notions of differentation, specifically the Wirtinger derivatives [73],

$$\frac{\partial}{\partial z} = \frac{1}{2}\left(\frac{\partial}{\partial x} - i\frac{\partial}{\partial y}\right) \quad \text{and} \quad \frac{\partial}{\partial \bar{z}} = \frac{1}{2}\left(\frac{\partial}{\partial x} + i\frac{\partial}{\partial y}\right). \tag{A.3}$$

Using (A.3), one may show that Cauchy-Riemann equations (A.2) are equivalent in complex notation to [73]

$$\frac{\partial f}{\partial \bar{z}} = 0. \tag{A.4}$$

Thus, the Cauchy-Riemann equations are a statement that an analytic function has no dependence on the $\bar{z}$ variable. Confer with [121] for further details on analytic functions.

A.2 Useful complex-variable identities

This section provides a collection of mathematical identities that are useful in the manipulation of expressions and functions of complex variables. Some of the identities can be easily derived from others, however some redundancy increases the ease of reference. This collection of identities stem from a variety of sources, including [7], [73], and [76].

In these identities, the expression $\bar{f}$ means $\overline{f(z,\bar{z})}$, not $\bar{f}(z,\bar{z})$ (cf. Equation (A.13)). Additionally, interpret $f(z)$ to mean that the complex-valued function f has no functional dependence on $\bar{z}$. Interpret $\overline{f(z,\bar{z})}$ to mean such dependence is present. Care should be taken, as some authors use $f(z)$ to also represent $f(z,\bar{z})$.

$\Re(\cdot)$ and $\Im(\cdot)$ operator identities

$$\Re(z) = \frac{z + \bar{z}}{2} \tag{A.5}$$

$$\Im(z) = \frac{z - \bar{z}}{2i} \tag{A.6}$$

$$\Re(a) = \Im(ia) \tag{A.7}$$

$$\Im(a) = -\Re(ia) \tag{A.8}$$

Inner product identities

$$\langle a, b \rangle = \langle b, a \rangle \tag{A.9}$$

$$\langle a, b \rangle = \left\langle \bar{a}, \bar{b} \right\rangle \tag{A.10}$$

$$\left\langle a, \bar{b} \right\rangle = \langle \bar{a}, b \rangle \tag{A.11}$$

$$\langle a, ib \rangle = -\langle ia, b \rangle \tag{A.12}$$

Function identities

$$\bar{f} = \overline{f(z, \bar{z})} = \bar{f}(\bar{z}, z) \neq \bar{f}(z, \bar{z}) \tag{A.13}$$

$$\overline{\log(z)} = \log(\bar{z}) \qquad \text{for } z \neq 0 \tag{A.14}$$

Differentiation identities

$$\frac{\partial}{\partial z} = \frac{1}{2}\left(\frac{\partial}{\partial x} - i\frac{\partial}{\partial y}\right) \tag{A.15}$$

$$\frac{\partial}{\partial \bar{z}} = \frac{1}{2}\left(\frac{\partial}{\partial x} + i\frac{\partial}{\partial y}\right) \tag{A.16}$$

$$\dot{f} = \frac{\partial f}{\partial z}\dot{z} + \frac{\partial f}{\partial \bar{z}}\dot{\bar{z}} \tag{A.17}$$

$$\overline{\frac{\partial f}{\partial z}} = \frac{\partial \bar{f}}{\partial \bar{z}} \tag{A.18}$$

$$\frac{\partial\left(f \circ g\right)}{\partial z}(z_0) = \frac{\partial f}{\partial z}(g(z_0))\frac{\partial g}{\partial z}(z_0) + \frac{\partial f}{\partial \bar{z}}(g(z_0))\frac{\partial \bar{g}}{\partial z}(z_0) \tag{A.19}$$

$$\frac{\partial\left(f \circ g\right)}{\partial \bar{z}}(z_0) = \frac{\partial f}{\partial z}(g(z_0))\frac{\partial g}{\partial \bar{z}}(z_0) + \frac{\partial f}{\partial \bar{z}}(g(z_0))\frac{\partial \bar{g}}{\partial \bar{z}}(z_0) \tag{A.20}$$

$$\frac{\partial}{\partial z}\left\langle f, g\right\rangle = \frac{1}{2}\left(\frac{\partial f}{\partial z}\bar{g} + f\frac{\partial \bar{g}}{\partial z} + \frac{\partial \bar{f}}{\partial z}g + \bar{f}\frac{\partial g}{\partial z}\right) \tag{A.21}$$

$$\frac{\partial}{\partial \bar{z}}\left\langle f, g\right\rangle = \frac{1}{2}\left(\frac{\partial f}{\partial \bar{z}}\bar{g} + f\frac{\partial \bar{g}}{\partial \bar{z}} + \frac{\partial \bar{f}}{\partial \bar{z}}g + \bar{f}\frac{\partial g}{\partial \bar{z}}\right) \tag{A.22}$$

Appendix B

Construction of targets for the hybrid steering controller

This appendix addresses the construction of targets for the hybrid steering controller of Chapter 5. As an example, it considers the two-vortex system that is used in the adaptive Lagrangian sampling simulations of Chapter 7.

B.1 Extraction of closed curves from the geometry of separatrices

Observability analysis shows that separatrices in the flow are highly observable paths (under Lagrangian position measurements) for a sampling vehicle to explore. The separatrix geometry may be constructed numerically through the following steps: (i) identify saddle fixed points in the flow field; (ii) from each saddle point, numerically integrate along the unstable manifolds in forward time and along the stable manifolds in reverse time until a close approach of another saddle or exit from the domain of interest; (iv) eliminate redundant separatrix curves that may have been generated; and (v) form a graph data structure that contains the saddle points as the vertices and separatrix curves as the directed edges of the graph. The result of these operations is a graph data structure (shown visually in the center of Figures B.1(a) and B.1(b)) that contains geometric information regarding the flow field, including unique identifiers for all saddle points and separatrices, coordinates of points numerically constituting these objects, and saddle-separatrix connection information. Figure B.1(a) shows an example of a saddle graph for a two-equal vortex case. The saddle graph consists of three saddle vertices, four heteroclinic connections (i.e., separatrices that connect two distinct saddle points), and two homoclinic connections (i.e., separatrices that begin and end at the same saddle point). Figure B.1(b) shows an example of a saddle graph for a two-unequal vortex case. In the unequal case, the saddle graph consists of three isolated saddle points that only have self-loops formed by homoclinic connections.

The hybrid steering controller in Chapter 5 requires simple, closed, regular curves as inputs for steering targets. All possible closed curves consisting of separatrices can be obtained by enumerating every elementary cycle in the saddle graph. Using an adjacency-list data structure to represent the saddle graph, the cycle-finding algorithm of Hawick and James [122] enumerates all elementary cycles in the graph. This algorithm is unique from other cycle-finding algortihms, because the adjacency-list data structure permits multiple edges between vertices, as well as self edges, which are necessary for representing homoclinic separatrices. The elementary cycles in the saddle graph are lists of saddle-vertex identifiers to which separatrix objects can be associated to generate closed curves. After extraction of all closed-curve cycles in the saddle graph, it is necessary to smooth

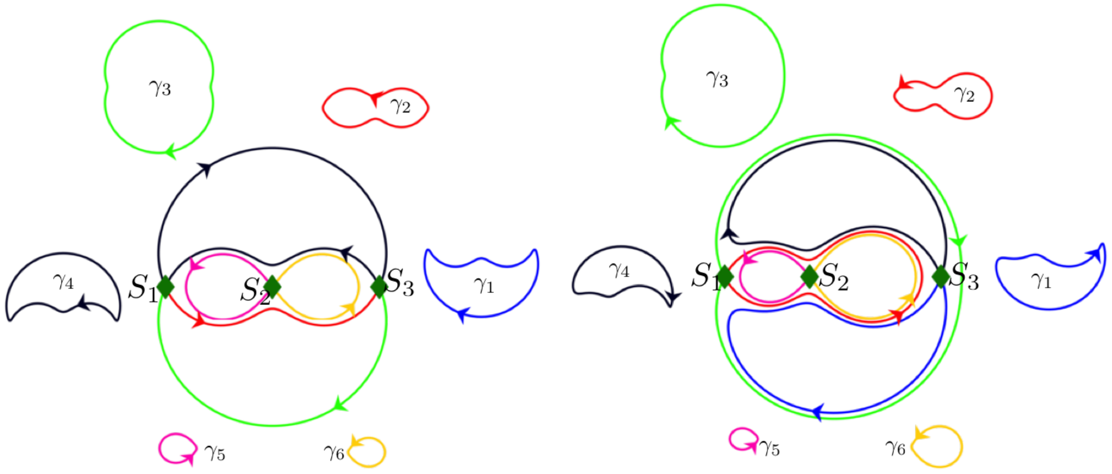

(a) (b)

Figure B.1: Extraction of closed, smooth separating-boundary curves in the two-vortex system for b) $\Gamma_2 = \Gamma_1$, and d) $\Gamma_2 = 2\Gamma_1$. The center portions of each subfigure are graph structures with saddle points at the vertices and separatrices as the edges. The surrounding curves in each subfigure are scaled, smoothed cycles formed by the separatrices.

cusps that occur at saddle points. The next section describes one means of addressing this issue.

B.2 Bézier curve smoothing

To create simple, closed, and regular target curves built from separatrices, one can smooth the closed curves near saddle points using fourth-order Bézier curves to meet the regularity requirement of the steering control law. These curves allow for the user to specify the beginning and ending tangent lines for a continuously differentiable connection to the remainder of the boundary curve.

A fourth-order Bézier curve γ_B parameterized by $\sigma \in [0, 1]$ is given in terms of contol points $c_0, c_1, c_2, c_3 \in \mathbb{C}$ by [123]

$$\gamma_B(\sigma) = (1-\sigma)^3 c_0 + 3(1-\sigma)^2 \sigma c_1 + 3(1-\sigma)\sigma^2 c_2 + \sigma^3 c_3. \tag{B.1}$$

Let r_1 and r_2 denote the radii of two concentric circles located at the saddle point S with $r_2 > r_1$ as shown in Figure B.2. Let c_0 and c_3 denote the entering and exiting intersection

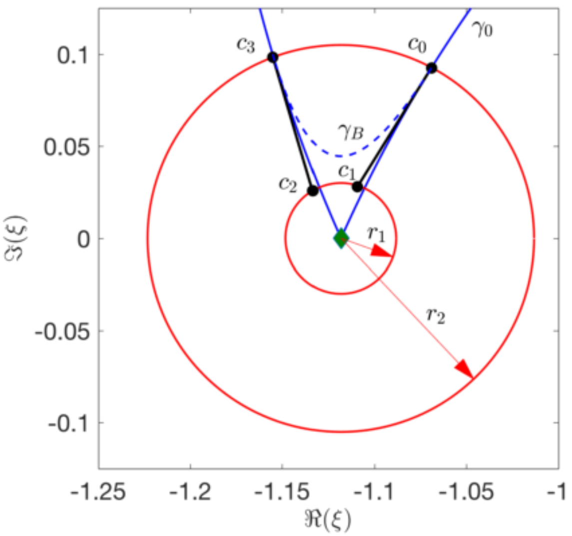

Figure B.2: Notation for smoothing near a saddle point using a Bézier curve.

points of the boundary curve γ_0 with the outer circle, respectively. Define c_1 and c_2 to be the respective intersections of tangent lines extended from c_0 and c_3 towards the inner circle, such that

$$c_1 = c_0 + \lambda_1 \frac{\gamma_0'}{|\gamma_0'|}\Big|_{c_0} \tag{B.2}$$

$$c_2 = c_3 - \lambda_2 \frac{\gamma_0'}{|\gamma_0'|}\Big|_{c_3}, \tag{B.3}$$

where

$$\lambda_1 = -\left\langle \frac{\gamma_0'}{|\gamma_0'|}\Big|_{c_0}, c_0 - S \right\rangle - \sqrt{\left\langle \frac{\gamma_0'}{|\gamma_0'|}\Big|_{c_0}, c_0 - S \right\rangle^2 - \left(r_2^2 - r_1^2\right)}, \tag{B.4}$$

$$\lambda_2 = \left\langle \frac{\gamma_0'}{|\gamma_0'|}\Big|_{c_3}, c_3 - S \right\rangle - \sqrt{\left\langle \frac{\gamma_0'}{|\gamma_0'|}\Big|_{c_3}, c_3 - S \right\rangle^2 - \left(r_2^2 - r_1^2\right)}. \tag{B.5}$$

The projected tangent lines intersect the inner circle provided the second terms in (B.4) and (B.5) are real numbers. If intersection does not occur, the values of r_1 and r_2 may be adjusted to satisfy this requirement.

Scaled examples of the resulting smoothed, closed-curve steering targets for the two-vortex system are shown surrounding the saddle graphs in Figures B.1(a) and B.1(b).

Appendix C

Parameter selection for numerical experiments in adaptive Lagrangian sampling

Parameters for the simulations performed in Chapter 7 were selected based on approximate comparison to long-endurance buoyancy-driven ocean-sampling platforms currently in use in field experiments (e.g., see [37, 49, 50, 77]). Assume a one-month deployment during which the vortex system completes approximately five full rotations. Assume a vortex separation distance of approximately 10 kilometers, comparable with submesoscale vortex pairs observed in the oceans [57]. Table C.1 tabulates the simulation parameters for this paper, many of which are linked to the mission, flow field, and hardware assumptions. Other parameters in the table are user-specified. The simulations use nondimensionalized values; the characteristic length scale corresponds with the vortex separation distance d, and the characteristic time scale corresponds with the period of revolution for the vortex pair.

Table C.1: Simulation parameters for numerical experiments in adaptive Lagrangian sampling

Symbol	**Parameter**	**Nominal value (Nondimensional)**	**Approximate representation**	**Basis for selection**
Simulation and vortex parameters				
T_{vort}	Period of vortex pair rotation	1	$\approx$ 5 periods per month	Flow-specific
T_{sim}	Simulation duration	5	1 month, $\approx$ 5 vortex periods	Hardware-specific, Mission-specific
T_{samp}	Time between measurements	0.0205	$\approx$ 3 hours	Mission-specific
d	Vortex separation distance	1	$\approx$ 10 km	Flow-specific
$\Gamma_1 + \Gamma_2$	Total circulation strength	$4\pi^2$	$\approx$ 5 periods per month	Constrained by T_{vort}, d
Vehicle parameters				
α	Through-water speed of vehicle	15.77	$\approx$ 0.3 m/s	Hardware-specific
$u_{\max}$	Magnitude of maximum steering rate	7890	$\approx$ 20m turning radius at rate α	Hardware-specific
Planning and control parameters				
T_{plan}	Time until re-evaluating plan	$5T_{\text{samp}}$	$\approx$ 15 hours	User-specified
T_h	Time horizon for planning	$2.5T_{\text{plan}}$	$\approx$ 37.5 hours	User-specified
K_1,K_2	Closed-curve steering control gains	5, 100	N/A	User-specified
K_3,K_4	Stream-function-value steering control gains	1000, 100	N/A	User-specified
Estimation parameters				
N_e	Number of ensemble members	5000	N/A	User-specified
R	Measurement noise covariance in the GMKF	diag([0.02,0.02])	N/A	User-specified, lower-bounded
Q	Process noise covariance in the GMKF	diag([1,0.1,0.1,1,0.1, 0.1,0.01,0.01])T_{samp}	N/A	User-specified, flow-specific
τ_{relax}	Time constant for model penalty relaxation	50	Initial data collection portion of mission	User-specified
`MaxIter`	Max EM iterations in Gaussian mixture fitting	200	N/A	User-specified
`MaxComplexity`	Number of Gaussians permitted in mixture model	10	N/A	User-specified
r_1, r_2	Radii for smoothing using Bèzier curves	0.05, $3.5r_1$	N/A	User-specified
Estimation initial condition				

P_0	Initial estimate covariance	diag([20,3,3,20, 3,3,0.01,0.01])	N/A	User-specified, flow-specific

Bibliography

[1] C. Huet and F. Mastroddi. “Autonomy for underwater robots - A European perspective”. In: *Autonomous Robots* 40.7 (2016), pp. 1113–1118.

[2] F. Maurelli et al. “Guest editorial: Special issue on long-term autonomy in marine robotics”. In: *Autonomous Robots* 40.7 (2016), pp. 1111–1112.

[3] R. C. Nelson. *Flight stability and automatic control.* 2nd. New York: McGraw-Hill Education, 1998, p. 456.

[4] C. Peterson and D. A. Paley. “Multivehicle coordination in an estimated time-varying flowfield”. In: *Journal of Guidance, Control, and Dynamics* 34.1 (2011), pp. 177–191.

[5] J.-M. P. Franosch et al. “Biomimetic lateral-line system for underwater vehicles”. In: *2010 IEEE Sensors* (2010), pp. 2212–2217.

[6] T. Salumäe and I Ranó. “Against the flow: A Braitenberg controller for a fish robot”. In: *IEEE International Conference on Robotics and Automation.* 2012, pp. 4210–4215.

[7] L. DeVries and D. A. Paley. “Multivehicle control in a strong flowfield with application to hurricane sampling”. In: *Journal of Guidance, Control, and Dynamics* 35.3 (2012), pp. 794–806.

[8] S. Coombs. “Smart skins: Information processing by lateral line flow sensors”. In: *Autonomous Robots* 11.3 (2001), pp. 255–261.

[9] J. Tao and X. B. Yu. “Hair flow sensors: from bio-inspiration to bio-mimicking - a review”. In: *Smart Materials and Structures* 21.113001 (2012), pp. 1–23.

[10] Y. Yang et al. “Artificial lateral line canal for hydrodynamic detection”. In: *Applied Physics Letters* 99.2 (2011), pp. 023701–3.

[11] A. T. Abdulsadda and X. Tan. “An artificial lateral line system using IPMC sensor arrays”. In: *International Journal of Smart and Nano Materials* 3.3 (2012), pp. 226–242.

[12] A. Klein and H. Bleckmann. “Determination of object position, vortex shedding frequency and flow velocity using artificial lateral line canals.” In: *Beilstein Journal of Nanotechnology* 2 (2011), pp. 276–283.

[13] R. Venturelli et al. "Hydrodynamic pressure sensing with an artificial lateral line in steady and unsteady flows." In: *Bioinspiration and Biomimetics* 7.036004 (2012), pp. 1–12.

[14] J. C. Montgomery, C. F. Baker, and A. G. Carton. "The lateral line can mediate rheotaxis in fish". In: *Nature* 389.6654 (1997).

[15] Y. Yang et al. "Artificial lateral line with biomimetic neuromasts to emulate fish sensing." In: *Bioinspiration and Biomimetics* 5.16001 (2010), pp. 1–9.

[16] A. Dagamseh et al. "Dipole-source localization using biomimetic flow-sensor arrays positioned as lateral-line system". In: *Sensors and Actuators A: Physical* 162.2 (2010), pp. 355–360.

[17] Y. Yang et al. "Distant touch hydrodynamic imaging with an artificial lateral line." In: *Proceedings of the National Academy of Sciences of the United States of America* 103.50 (2006), pp. 18891–5.

[18] Z. Ren and K. Mohseni. "A model of the lateral line of fish for vortex sensing". In: *Bioinspiration and Biomimetics* 7.036016 (2012), pp. 1–14.

[19] A. G. P. Kottapalli et al. "A flexible liquid crystal polymer MEMS pressure sensor array for fish-like underwater sensing". In: *Smart Materials and Structures* 21.11 (2012), p. 115030.

[20] A. Kottapalli et al. "Polymer MEMS pressure sensor arrays for fish-like underwater sensing applications". In: *Micro and Nano Letters* 7.12 (2012), pp. 1189–1192.

[21] M. Asadnia et al. "Polymer MEMS pressure sensor arrays for fish-like underwater sensing applications". In: *Micro and Nano Letters* 7.12 (2012), pp. 1189–1192.

[22] T. Salumäe and M. Kruusmaa. "Flow-relative control of an underwater robot". In: *Proceedings of the Royal Society A* 469.20120671 (2013), pp. 1–19.

[23] L. DeVries et al. "Distributed flow estimation and closed-loop control of an underwater vehicle with a multi-modal artificial lateral line". In: *Bioinspiration and Biomimetics* 10.2 (2015), p. 025002.

[24] O. Akanyeti et al. "FILOSE for Svenning: A flow sensing bioinspired robot". In: *IEEE Robotics and Automation Magazine* 21.3 (2014), pp. 51–62.

[25] F. Zhang et al. "Distributed flow sensing for closed-loop speed control of a flexible fish robot". In: *Bioinspiration and Biomimetics* 10.6 (2015), p. 65001.

[26] Y. Xu and K. Mohseni. "Bioinspired hydrodynamic force feedforward for autonomous underwater vehicle control". In: *IEEE/ASME Transactions on Mechatronics* 19.4 (2014), pp. 1127–1137.

[27] B. T. Hinson, M. K. Binder, and K. A. Morgansen. "Path planning to optimize observability in a planar uniform flow field". In: *American Control Conference.* Washington, DC, 2013, pp. 1394–1401.

[28] J. D. Quenzer and K. A. Morgansen. “Observability based control in range-only underwater vehicle localization”. In: *2014 American Control Conference* (2014), pp. 4702–4707.

[29] N. E. Leonard et al. “Coordinated control of an underwater glider fleet in an adaptive ocean sampling field experiment in Monterey Bay”. In: *Journal of Field Robotics* 27.6 (2010), pp. 718–740.

[30] C. H. Bishop, B. J. Etherton, and S. J. Majumdar. “Adaptive sampling with the Ensemble Transform Kalman Filter. Part I: Theoretical aspects”. In: *Monthly Weather Review* 129.3 (2001), pp. 420–436.

[31] R. E. Davis, N. E. Leonard, and D. M. Fratantoni. “Routing strategies for underwater gliders”. In: *Deep Sea Research Part II: Topical Studies in Oceanography* 56.3-5 (2009), pp. 173–187.

[32] F. Lekien and N. E. Leonard. “Nonuniform coverage and cartograms”. In: *SIAM Journal on Control and Optimization* 48.1 (2009), pp. 351–372.

[33] R. Cui, Y. Li, and W. Yan. “Mutual information-based multi-AUV path planning for scalar field sampling using multidimensional RRT*”. In: 46.7 (2015), pp. 1–12.

[34] J. Das et al. “Coordinated sampling of dynamic oceanographic features with underwater vehicles and drifters”. In: *The International Journal of Robotics Research* 31.5 (2012), pp. 626–646.

[35] B. Mourre and A. Alvarez. “Benefit assessment of glider adaptive sampling in the Ligurian Sea”. In: *Deep Sea Research Part I: Oceanographic Research Papers* 68 (2012), pp. 68–78.

[36] D. Zhang, C. Colburn, and T. Bewley. “Estimation and adaptive observation of environmental plumes”. In: *American Control Conference.* San Francisco, CA, 2011, pp. 4281–4286.

[37] S. Ramp et al. “Preparing to predict: The Second Autonomous Ocean Sampling Network (AOSN-II) experiment in the Monterey Bay”. In: *Deep Sea Research Part II: Topical Studies in Oceanography* 56.3-5 (2009), pp. 68–86.

[38] M. J. Hoffman et al. “An advanced data assimilation system for the Chesapeake Bay: Performance evaluation”. In: *Journal of Atmospheric and Oceanic Technology* 29.10 (2012), pp. 1542–1557.

[39] A. Melet, J. Verron, and J.-M. Brankart. “Potential outcomes of glider data assimilation in the Solomon Sea: Control of the water mass properties and parameter estimation”. In: *Journal of Marine Systems* 94 (2012), pp. 232–246.

[40] C. J. Cannell and D. J. Stilwell. “A comparison of two approaches for adaptive sampling of environmental processes using autonomous underwater vehicles”. In: *Proceedings of the MTS/IEEE OCEANS Conference* (2005), 1514 –1521 Vol. 2.

[41] D. L. Rudnick and S. T. Cole. “On sampling the ocean using underwater gliders”. In: *Journal of Geophysical Research* 116.C08010 (2011), pp. 1–12.

[42] P. F. J. Lermusiaux et al. “Science of autonomy: Time-optimal path planning and adaptive sampling for swarms of ocean vehicles”. In: *Springer Handbook of Ocean Engineering: Autonomous Ocean Vehicles, Subsystems and Control*. Ed. by T. Curtin. Springer-Verlag, 2013, pp. 481–498.

[43] T. Lolla et al. “Path planning in time dependent flow fields using level set methods”. In: *International Conference on Robotics and Automation (ICRA)*. IEEE, 2012, pp. 166–173.

[44] K. Mallory et al. “Distributed allocation of mobile sensing swarms in gyre flows”. 2013.

[45] J. H. Talley, Lynne D., Pickard, George L., Emery, William J., Swift. *Descriptive physical oceanography: An introduction*. 6th. London: Academic Press, Elsevier, 2011, pp. 347–349.

[46] M. Belbeoch. *Argo: Part of the integrated global observation strategy*. URL: `http://www.argo.ucsd.edu/` (visited on 01/01/2014).

[47] A. Alvarez, B. Garau, and A. Caiti. *Combining networks of drifting profiling floats and gliders for adaptive sampling of the Ocean*. 2007.

[48] B. Eakins and G. Sharman. *Volumes of the world’s oceans from ETOPO1*. 2014. URL: `http://www.ngdc.noaa.gov/mgg/global/etopo1oceanvolumes.html` (visited on 01/01/2014).

[49] D. Paley, F. Zhang, and N. Leonard. “Cooperative control for ocean sampling: The Glider Coordinated Control System”. In: *IEEE Transactions on Control Systems Technology* 1063-6536 (2008), pp. 1–10.

[50] R. N. Smith et al. “Persistent ocean monitoring with underwater gliders: Adapting sampling resolution”. In: *Journal of Field Robotics* 28.5 (2011), pp. 714–741.

[51] D. N. Subramani et al. “A stochastic optimization method for energy-based path planning”. In: *Dynamic Data-driven Environmental Systems Science Conference*. 2014, pp. 347–358.

[52] E. Forgoston et al. “Set-based corral control in stochastic dynamical systems: making almost invariant sets more invariant.” In: *Chaos* 21.1 (2011), p. 013116.

[53] H. Salman, K. Ide, and C. K.R. T. Jones. “Using flow geometry for drifter deployment in Lagrangian data assimilation”. In: *Tellus A* 60.2 (2008), pp. 321–335.

[54] L. Billings and I. B. Schwartz. “Identifying almost invariant sets in stochastic dynamical systems.” In: *Chaos* 18.2 (2008), p. 023122.

[55] S. C. Shadden et al. “The correlation between surface drifters and coherent structures based on high-frequency radar data in Monterey Bay”. In: *Deep Sea Research Part II: Topical Studies in Oceanography* 56.35 (2009), pp. 161–172.

[56] S. Ravela. “Quantifying uncertainty for coherent structures”. In: *Procedia Computer Science* 9 (2012), pp. 1187–1196.

[57] I. Koszalka. “Mesoscale vortices, Lagrangian transport and marine ecosystem dynamics”. PhD thesis. Politecnico Di Torino, 2008, p. 104.

[58] M. A. Hsieh et al. “Robotic manifold tracking of coherent structures in flows”. In: *International Conference on Robotics and Automation (ICRA)*. 2012, pp. 4242 –4247. arXiv: `arXiv:1204.4600v1`.

[59] M. Pazos. *The GDP drifter data assembly center (DAC): Hurricane drifter array, NOAA AOML*. URL: `http://www.aoml.noaa.gov/phod/dac/dacdata.php`.

[60] A. J. Krener and K. Ide. “Measures of unobservability”. In: *Proceedings of the 48h IEEE Conference on Decision and Control (CDC) held jointly with 2009 28th Chinese Control Conference*. IEEE, 2009, pp. 6401–6406.

[61] R. Ghabcheloo et al. “Coordinated path-following in the presence of communication losses and time delays”. In: *SIAM Journal on Control and Optimization* 48.1 (2009), pp. 234–265.

[62] F. Zhang and N. E. Leonard. “Coordinated patterns of unit speed particles on a closed curve”. In: *Systems and Control Letters* 56.6 (2007), pp. 397–407.

[63] D. A. Paley and C. Peterson. “Stabilization of collective motion in a time-invariant flowfield”. In: *Journal of Guidance, Control, and Dynamics* 32.3 (2009), pp. 771–779.

[64] F. D. Lagor et al. “Bio-inspired flow sensing and control: Autonomous rheotaxis using distributed pressure measurements”. In: *Journal of Unmanned System Technology* 1.3 (2013), pp. 78–88.

[65] F. D. Lagor, K. Ide, and D. A. Paley. “Incorporating prior knowledge in observability-based path planning for ocean sampling”. In: *Systems and Control Letters* 97 (2016), pp. 169–175.

[66] F. D. Lagor, K. Ide, and D. A. Paley. “Non-Gaussian estimation of a potential flow using a controlled Lagrangian sensor guided to invariant set boundaries by augmented observability”. In: *(Submitted)* (2016).

[67] F. D. Lagor et al. “Bio-inspired flow sensing and control: Autonomous underwater navigation using distributed pressure measurements”. In: *18th International Symposium on Unmanned Untethered Submersible Technology*. Portsmouth, NH, 2013, pp. 1–8.

[68] F. D. Lagor, K. Ide, and D. A. Paley. “Touring the invariant sets of a two-vortex system using streamline control”. In: *Conference on Decision and Control (CDC)*. Osaka, JP, 2015, pp. 2217–2222.

[69] F. D. Lagor et al. “Non-Gaussian estimation of a two-vortex flow using a Lagrangian sensor guided by output feedback control”. In: *2016 American Control Conference (ACC)*. Boston, MA, 2016, pp. 1030–1035.

[70] F. D. Lagor and D. A. Paley. "Active singularities for motion planning in an N-vortex system". In: *Dynamic Data-driven Environmental Systems Science.* Ed. by S. Ravela and A. Sandu. Springer, 2015, pp. 334–346.

[71] F. Zhang et al. "Distributed flow sensing using Bayesian estimation for a flexible fish robot". In: *Proc. of the ASME 2015 Dynamic Systems and Control Conference (DSCC).* Columbus, OH, 2015, pp. 1–10.

[72] F. Zhang et al. "Robotic Fish: Flow-relative control behaviors using distributed flow sensing". In: *ASME Mechanical Engineering Magazine* 138.3 (2016), S2–S5.

[73] K. Kreutz-Delgado. "The complex gradient operator and the CR-calculus". In: *arXiv preprint arXiv:0906.4835* (2009), pp. 1–74. arXiv: `0906.4835`.

[74] P. Newton. *The N-vortex problem: Analytical techniques.* New York: Springer, 2001.

[75] J. E. Marsden and T. S. Ratiu. *Introduction to mechanics and symmetry.* English. Vol. 48. 12. New York: Amer. Inst. of Physics, 1995, p. 65.

[76] L. Milne-Thomson. *Theoretical hydrodynamics.* 5th. New York: Dover Publications, 1968, pp. 157–159.

[77] F. Zhang and N. Leonard. "Cooperative filters and control for cooperative exploration". In: *IEEE Transactions on Automatic Control* 55.3 (2010), pp. 650–663.

[78] H. Khalil. *Nonlinear Control.* Upper Saddle River N.J.: Prentice Hall, 2015.

[79] R. E. Kalman and R. S. Bucy. "New results in linear filtering and prediction theory". In: *Journal of Basic Engineering* 83.1 (1961), pp. 95–108.

[80] M. S. Arulampalam et al. "A tutorial on particle filters for online nonlinear/non-Gaussian Bayesian tracking". In: *IEEE Transactions on Signal Processing* 50.2 (2002), pp. 174–188.

[81] J. Kaipio and E. Somersalo. *Statistical and computational inverse problems.* New York: Springer, 2005.

[82] R. Chen and J. S. Liu. "Mixture Kalman filters". In: *J.R. Statist. Soc.B* 62.3 (2000), pp. 493–508.

[83] I. Hoteit et al. "A new approximate solution of the optimal nonlinear filter for data assimilation in meteorology and oceanography". In: *Monthly Weather Review* 136.1 (2008), pp. 317–334.

[84] T. Sondergaard and P. F. J. Lermusiaux. "Data assimilation with Gaussian mixture models using the dynamically orthogonal field equations. Part I: Theory and scheme". In: *Monthly Weather Review* Volume 141 (2013), pp. 1737–1760.

[85] C. Bishop. *Pattern recognition and machine learning.* New York: Springer, 2006.

[86] M. A. Carreira-Perpinan. "Mode finding for mixtures of Gaussian distributions". In: *IEEE Trans. on Pattern Analysis and Machine Intelligence* 22.11 (2000), pp. 1–23.

[87] R. W. Brockett. *Finite dimensional linear systems*. New York: John Wiley and Sons, 1970, pp. 1–244.

[88] L. DeVries and D. A. Paley. "Observability-based optimization for flow sensing and control of an underwater vehicle in a uniform flowfield". In: *American Controls Conference*. 2013, pp. 1–6.

[89] N. D. Powel and K. A. Morgansen. "Empirical observability Gramian rank condition for weak observability of nonlinear systems with control". In: *54th IEEE Conference on Decision and Control*. Osaka, JP, 2015, pp. 6342–6348.

[90] R. L. Panton. *Incompressible flow*. New York: Wiley, 1984.

[91] J. D. Anderson. *Fundamentals of aerodynamics*. New York: McGraw-Hill, 1984.

[92] R. Fox, A. McDonald, and P. Pritchard. *Introduction to fluid mechanics*. 6th. Hoboken N.J.: Wiley, 2004.

[93] N. Beckman. *Model systems in neuroethology: Prey capture in mottled sculpin*. URL: `http://nelson.beckman.illinois.edu/courses/neuroethol/models/mottled_sculpin/mottled_sculpin.html`.

[94] Resources Information Standards Committee of British Columbia. *Field key to the freshwater fishes of British Columbia*. URL: `http://www.ilmb.gov.bc.ca/risc/pubs/aquatic/freshfish/fresht-25.htm`.

[95] S. Coombs, C. B. Braun, and B. Donovan. "The orienting response of Lake Michigan mottled sculpin is mediated by canal neuromasts." In: *The Journal of Experimental Biology* 204.2 (2001), pp. 337–48.

[96] *COMSOL Multiphysics®*. Stockholm, Sweden. URL: `www.comsol.com`.

[97] F. Zhang, E. W. Justh, and P. S. Krishnaprasad. "Boundary tracking and obstacle avoidance using gyroscopic control". In: *Recent Trends in Dynamical Systems*. Ed. by A. Johann. Vol. Springer P. Springer Basel, 2013. Chap. 16, pp. 417–445.

[98] A. Pressley. "How much does a curve curve?" In: *Elementary differential geometry*. 2nd ed. Vol. XII. Springer, 2010. Chap. 2, pp. 29–54.

[99] D. A. Paley. "Cooperative control of collective motion for ocean sampling autonomous vehicles". PhD thesis. Princeton University, 2007.

[100] A. Gelb, ed. *Applied optimal estimation*. Cambridge MA: The M.I.T. Press, 1974, pp. 1–374.

[101] M. Aoki. "On observability of stochastic discrete-time dynamic systems". In: *Journal of the Franklin Institute* 286.1 (1968), pp. 36–58.

[102] F.-X. Le Dimet and O. Talagrand. "Variational algorithms for analysis and assimilation of meteorological observations: theoretical aspects". In: *Tellus A* 38A.2 (1986), pp. 97–110.

[103] P. Courtier, J. N. Thepaut, and A. Hollingsworth. “A Strategy for Operational Implementation of 4d-Var, Using an Incremental Approach”. In: *Quarterly Journal of the Royal Meteorological Society* 120.519 (1994), pp. 1367–1387.

[104] Z. Li and I. Navon. “Optimality of variational data assimilation and its relationship with the Kalman filter and smoother”. In: *Q. J. R. Meteorol. Soc.* 127 (2001), pp. 661–683.

[105] G. Strang. *Linear algebra and its applications*. 4th. Belmont CA: Thomson Brooks/Cole, 2006, pp. 1–487.

[106] J. J. Levin. “On the matrix Riccati equation”. In: *Proc. Amer. Math. Soc.* 10.December (1959), pp. 519–524.

[107] C.-T. Chen. *Linear system theory and design*. New York: Holt Rinehart and Winston, 1984.

[108] S. Kay. *Fundamentals of statistical signal processing, volume I: Estimation theory*. Upper Saddle River N.J.: Prentice Hall, 1993, pp. 39–81.

[109] K. Law, A. Stuart, and K. Zygalakis. *Data assimilation: A mathematical introduction*. Cham: Springer International, 2015, pp. 151–174.

[110] B. Øksendal. *Stochastic differential equations*. Fifth Edit. Heidelberg: Springer-Verlag, 2000, pp. 153–157.

[111] P. Maybeck. *Stochastic Models, Estimation, and Control: Vol. 1*. New York: Academic Press, 1979, p. 240.

[112] J. S. Whitaker and T. M. Hamill. “Ensemble data assimilation without perturbed observations”. In: *Monthly Weather Review* 130 (2002), pp. 1913–1924.

[113] B. Free, M. K. Patnaik, and D. A. Paley. “Observability-based path-planning and flow-relative control of a bioinspired sensor array in a Karman vortex street”. In: *American Control Conference*. Seattle, WA, 2017, pp. 1–7.

[114] J. H. Tu et al. “On dynamic mode decomposition - Theory and applications”. In: *Journal of Computational Dynamics* September (2013), pp. 1–30. arXiv: `arXiv:1312.0041v1`.

[115] R. Grasso et al. “Environmental field estimation by consensus based dynamic sensor networks and underwater gliders”. In: *2015 23rd European Signal Processing Conference, EUSIPCO 2015* (2015), pp. 205–209.

[116] R. Grasso et al. “Dynamic underwater glider network for environmental field estimation”. In: *IEEE Transactions on Aerospace and Electronic Systems* 52.1 (2016), pp. 379–395.

[117] B. J. Julian et al. “A scalable information theoretic approach to distributed robot coordination”. In: *2011 IEEE/RSJ International Conference on Intelligent Robots and Systems* (2011), pp. 5187–5194.

[118] D. Gu and H. Hu. "Spatial Gaussian process regression with mobile sensor networks". In: *IEEE Transactions on Neural Networks and Learning Systems* 23.8 (2012), pp. 1279–1290.

[119] R. Graham and J. Cortés. "Cooperative adaptive sampling of random fields with partially known covariance". In: *International Journal of Robust and Nonlinear Control* 22.5 (2012), pp. 504–534.

[120] L. V. Nguyen et al. "Information-driven adaptive sampling strategy for mobile robotic wireless sensor network". In: *IEEE Transactions on Control Systems Technology* 24.1 (2016), pp. 372–379.

[121] G. F. Carrier, M. Krook, and C. E. Pearson. *Functions of a Complex Variable.* Philadelphia: Society of Industrial and Applied Mathematics, 2005, p. 438.

[122] K. A. Hawick and H. A. James. *Enumerating circuits and loops in graphs with self-arcs and multiple-arcs.* Tech. rep. 2008, pp. 14–20.

[123] E. Kreyszig. *Advanced engineering mathematics.* New York: Wiley, 1972.

Index